Tailoring quantum structures for active photonic crystals

Kuznetsova, Nadezda

Publication date:
2015

Document Version
Publisher's PDF, also known as Version of record

Tailoring quantum structures for active photonic crystals

A dissertation submitted to the Department of Photonics Engineering at the Technical University of Denmark as part of the requirements for Doctor of Philosophy

Nadezda Kuznetsova

February 2015

Abstract

This work is dedicated to the tailoring of quantum structures, with particular attention to the integration of selective area grown (SAG) active material into photonic crystal (PhC) slabs. The platform based on active PhC is vital to the realization of highly efficient elements with low energy consumption for on-chip and chip-to-chip optical communication. In order to develop metal-organic vapor phase epitaxial selective area etching and growth, a mask was fabricated in the HSQ e-beam resist including optimization of exposure and development conditions. By use of CBr_4 as an etchant, in situ etching demonstrated various trench profiles along the [0-1-1] and [0-11] crystallographic directions. Selectively grown InGaAs/InP quantum wells (QWs) possessed distinct geometrical and optical properties in the cases of directly grown InGaAs and when an InP buffer was deposited underneath. The fabrication process for the incorporation of an SAG material into needle-shaped specimens for transmission electron microscopy or into PhC amplifiers was optimized to improve the alignment accuracy to below 100 nm.

Micro-photoluminescence measurements of SAG QW showed a large wavelength red-shift (over 100 nm) compared to the unpatterned area and between the structures oriented along the [0-1-1] and [0-11] directions. Strong wavelength dependence with variations of the mask width of a few μm and opening sizes of hundreds of nanometers was observed.

Incorporation of an active medium into PhC structures has showed promising results; in particular, the emission control of SAG QW matched the operating wavelength of photonic crystals. A strong photoluminescence signal in the slow light regime with the group index of 18 was demonstrated.

Resume

Dette arbejde er dedikeret til skræddersy kvante strukturer med særligt fokus på integration af selektiv-område-dyrkning (SOD) af aktivt materiale i fotoniske krystal (FK) membraner. Platformen baseret på aktivt FK er essentiel for at realisere høj-effektive elementer med lavt energiforbrug til on-chip og chip-til-chip optisk kommunikation. Med henblik på at udvikle metal-organisk damp-fase epitaksial selektiv-område-æts og -dyrkning blev en maske fabrikeret i HSQ elektron-stråle resist, og parametrene for eksponering og udvikling blev optimerede. Ved brug af CBr_4 som æts førte in-situ æts til forskellige grøftprofiler langs [0-1-1] og [0-11] krystalakserne. Selektivt dyrkede InGaAs/InP kvantebrønde besad distinkte geometriske og optiske egenskaber i tilfældene af direkte dyrket InGaAs og da en underliggende InP buffer blev tilføjet. Fabrikationsprocessen for inkorporeringen af SOD materiale i nåleformede prøver til transmissionselektronmikroskopi og ind i FK forstærkere blev optimeret, hvilket førte til sporingspræcision på under 100 nm.

Målinger af mikrofotoluminiscens fra SOD kvantebrønde udviste en stor rødforskydning af bølgelængden (mere end 100 nm) sammenlignet med det ustrukturerede område og mellem strukturer orienteret langs [0-1-1] og [0-11] akserne. Stor bølgelængdeafhængighed ved variationer af maskebredden på et par μm og åbningsstørrelser på få hundrede nm blev observeret.

Inkorporering af aktivt materiale i FK strukturer har ført til lovende resultater; især matchede emissionskontrollen af SOD kvantebrønde operationsbølgelængden af de fotoniske krystaller. Et stærkt fotoluminiscenssignal blev demonstreret i regimet for langsomt lys med et gruppeindeks på 18.

Acknowledgments

"Our prime purpose in this life is to help others.
And if you can't help them, at least don't hurt them."
Dalai Lama

I would like to start with a thanks to my main supervisor Associate Professor Dr. Kresten Yvind for hiring me for this position and numerous discussions during the project in addition to reading the entire thesis and providing invaluable comments. I owe my deepest appreciation to my co-supervisor, Dr. Elizaveta Semenova, who introduced me to the exciting world of epitaxy and, in particular, taught how to operate the MOVPE machine and prepare growth recipes. Liza also helped to keep me motivated in easy and difficult times.

I am grateful to the Villum Kann Rasmussen foundation Center of Excellence: Nanophotonics for Terabit Communication (NATEC) headed by Professor Jesper Mørk for funding and support this work.

Many people have contributed to this work either directly or indirectly. At the beginning of my project, Dr. Martin Schubert assisted me extensively in the cleanroom. Moreover, Martin had built up a μPL setup, which was one of the main measurement tools in this work. For that I am very thankful to him. I considered it an honor to work with Dr. Peixiong Shi, who spent an abundance of time exposing the wafers for me with the electron beam writer and, in addition, provided SIMS measurements. I am especially thankful for all knowledge received from him and all bread-support during late evenings/nights work. It is my pleasure to acknowledge Dr. Pierre Colman for the designing the photonic crystal waveguides, fruitful collaboration, beneficial discussions about photonic crystals and other matters, help in the lab, a great sense of humor and above all for keeping my spirit up all the time. I would like to thank Dr. Luisa Ottaviano, who was always available to help with any cleanroom issues and share her results with regards to optimized processes.

Thanks are too to Dr. Sara Ek for transferring her photonic crystals fabrication and experimental skills to me, and also for making our cold and dark lab a pleasant place to work in. I would like to thank Yi Yu for sharing his process optimization details about photonic crystals, Dr. Weiqi Xue for help with the devices characterization, and Dr. Yaohui Chen for the designing of the photonic crystals lasers.

I owe my deepest gratitude to Dr. Shima Kadkhodazadeh from DTU CEN for active collaboration on needle-shaped specimens. Shima also provided all STEM experiments and EDX analysis presented in this thesis.

I am grateful to many people at DTU Danchip for their work including Dr. Tine Greibe, Dr. Thomas Aarøe Anhøj and Dr. Hassan Ouacha for providing e-beam trainings, Elena Khomtchenko and Jens Hemmingsen for helping with photolithography equipment, and Roy Cork for sharing his process knowledge. I would like to offer my special thank you to Dr. Jesper Hanberg for valuable trainings in the cleanroom.

Furthermore, I wish to thank to a number of people: Assistant Professor Dr. Alexander Huck for help with the μPL setup, Dr. Oleksii Kopylov for help with the cryostat equipment, Dr. Radu Malureanu for help with the L-edit codes. I am especially grateful to Dr. Natalie Kryzhanovskaya and Professor Alexey Zhukov for welcoming and guiding me in their lab at St. Petersburg Academic University. Thanks to Dr. Sven Rodt for welcoming me at TU Berlin and providing cathodoluminescence measurements.

I would like also to thank the whole Nanophotonic Devices group, in particular, those who have not been mentioned yet: Dr. Thor Ansbæk, Dr. Minhao Pu, Alexandra Lupi, Miranda Mitrovic, Dr. Yunhong Ding, Dr. Lars Hagedorn Frandsen, Louise Floor Frandsen, Asger Sellerup Jensen. In addition, I am deeply grateful for the assistance of Charlotte Melgaard Larsen. Further thanks to my former officemates: Irina, Krzysztof, Minhao, and Miranda for the positive atmosphere of our work place and unforgettable memories. I am also happy to acknowledge many wonderful people I met at DTU, in particular, Kimberly, Victoria, Maksim, Andrey N., Andrey M., Claudia, Olena, Corinna, Giuseppe, Andrey L. and Andrey A. and many others.

And lastly, I would like to thank Sasha, Alexandra, Liza, Irina, Luisa, Martin, Lesha, Pierre and Robert for providing valuable and extensive comments on the different parts of this thesis. My special thank you is to Associate Professor Dr. Niels Gregersen for the translation of the abstract into Danish. Thanks to Professor Tatiana Shubina for her enthusiasm and appropriate comments, and to Dr. Valentin Jmerik for useful pieces of advice.

On a personal note, I would like to express my deepest appreciation to Dr. Irina Kulkova for her personal and technical support, fruitful discussions about cleanroom work, updates on the last gossips at the department, and most importantly for bringing me to Denmark. This thesis would not have been possible without support and belief in me of all my friends and family who always motivate me. And, last but not least, my deepest gratitude to two Svetlana, my mother and my daughter, for their unconditional love and patience.

List of Publications

Journal publications

1. N. Kuznetsova, I.V. Kulkova, E.S. Semenova, S. Kadkhodazadeh, N.V. Kryzhanovskaya, A.E. Zhukov, and K. Yvind, "Crystallographic dependent in-situ CBr_4 selective nano-area etching and local regrowth of InP/InGaAs by MOVPE", J. Cryst. Growth 406, 111–115 (2014).

2. I.V. Kulkova, S. Kadkhodazadeh, N. Kuznetsova, A. Huck, E.S. Semenova, and K. Yvind, «High-quality MOVPE butt-joint integration of InP/AlGaInAs/InGaAsP-based all-active optical components», J. Cryst. Growth 402, 243–248 (2014).

3. D. Vukovic, Y. Yu, M. Heuck, S. Ek, N. Kuznetsova, P. Colman, E. Palushani, J. Xu, K. Yvind, L.K. Oxenløwe, J. Mørk, and C. Peucheret, "Wavelength conversion of a 9.35 Gb/s RZ OOK signal in an InP photonic crystal nanocavity," IEEE Photon. Technol. Lett. 26, pp. 257-260 (2013).

4. Y. Yu, E. Palushani, M. Heuck, N. Kuznetsova, P. T. Kristensen, S. Ek, C. Peucheret, D. Vukovic, L. K. Oxenløwe, S. Combrie, A. de Rossi, K. Yvind, and J. Mørk, "Switching characteristics of an InP photonic crystal nanocavity: Experiment and theory", Opt. Express 21, 31047-31061 (2013).

5. Y. Yu, M. Heuck, S. Ek, N. Kuznetsova, K. Yvind, and J. Mørk, "Experimental demonstration of a four-port photonic crystal cross-waveguide structure," Appl. Phys. Let. **101**, 251113 (2012).

Conference proceedings

6. I. V. Kulkova, N. Kuznetsova, E. S. Semenova, and K. Yvind, "Butt-joint integration of active optical components based on InP/AlInGaAsP alloys," in Proc. of the 26th International Conference on IPRM: pp. 1-2, IEEE (2014).

7. N. Kuznetsova, P. Colman, E. Semenova, S. Kadkhodazadeh, N.V. Kryzhanovskaya, S. Ek, W. Xue, M. Schubert, A.E. Zhukov and K. Yvind, "Nonplanar nanoselective area growth of InGaAs/InP," in Proc. SPIE 8996, 899608 (2014).

8. Y. Yu, E. Palushani, M. Heuck, S. Ek, N. Kuznetsova, P. Colman, D. Vukovic, C. Peucheret, L. K. Oxenløwe, K. Yvind, and J. Mørk "Ultra-fast low energy switching using an InP photonic crystal H0 nanocavity" in Proc. of Lasers Electro-Opt. Conf., pp. 1–2, paper MI1-4 (2013).

9. M. Heuck, Y. Yu, P. T. Kristensen, N. Kuznetsova, K. Yvind, and J. Moerk “Active photonic crystal switches: modeling, design and experimental characterization”, ICTON (2013).

10. D. Vukovic, Y. Yu, M. Heuck, S. Ek, N. Kuznetsova, P. Colman, E. Palushani, J. Xu, K. Yvind, L.K. Oxenløwe, J. Mørk, and C. Peucheret, “All-optical 9.35 Gb/s wavelength conversion in an InP photonic crystal nanocavity,” ACP/IPOC 2013 (2013).

11. N. Kuznetsova, E. Semenova, S. Kadkhodazadeh, and K. Yvind, “Nanoscale semiconductor optical devices,” Nano-optics for enhancind light-matter interactions on a molecular scale, Springer, pp. 417-418 (2013).

12. N. Kuznetsova, E. Semenova, S. Kadkhodazadeh, M. Schubert, and K. Yvind “Nano-selective area growth of InGaAs/InP using CBr_4 in-situ etching,” in Integrated Photonics Research, Silicon and Nanophotonics (IPR), JTu5A.12 (2012).

13. S. Kadkhodazadeh, E. Semenova, N. Kuznetsova, M. Schubert, M. Thuvander, K. M. Stiller, K. Yvind, and R. E. Dunin-Borkowski, “Towards quantitative three-dimensional characterisation of InAs quantum dots,” part of: MC Kiel, Germany, pp. IM3-P151 (2011), ISBN: 978-3-00-033910-3.

Table of Contents

"I don't know anything, but I do know
that everything is interesting if you go into it deeply enough"
Richard Feynman

Chapter 1. Introduction

1.1 Optical interconnection

With rapid growth in global Internet usage, especially in visual networking there is a greater need for high-speed and energy-efficient interconnection systems. As social networking, high-definition video streaming, cloud computing and other services become increasingly affordable, it leads to a correlated rise in demand for greater bandwidth. To date, the routing and processing of data has been performed by electrical components due to the lack of optical equivalents.

The drawbacks of electrical wires, such as limited density and speed, which are exacerbated at high speed, constrain performance of the information processing systems [1]. For short distance communication and inter and intra-chip connections, electrical wires are still more cost-effective, however the power dissipation becomes a big issue that increases the overall cost. Consequently, new technology needs to emerge to keep pace with the rapid boost of data processing. Exchanging electrical interconnections with optical interconnections, especially on the chip level, would result in beneficial interconnection density, energy consumption and time due to shorter wavelength and higher carrier frequency of optical signals [2]. Optics, for instance, does not have frequency-dependent loss operating from 1 MHz to 1 GHz or frequency-dependent cross-talk [3]. Certainly, all-optical solutions, such as the creation of network-on-chip (NOC), are essential for the future communication. However, to be competitive with electronics, optical circuits have to be not only high-performance, but also satisfy the requirement of low cost. As presented by D.Miller [4], the total power consumption should be ~10 fJ/bit for short connections between chips. The target for intrachip power consumption is even smaller such as a few femtojoule per bit.

Large productivity gains are achieved by integration of more components on a chip to implement complex functions in a short period of time. Growth of optical components on a single chip follows the same trend as microelectronic elements, referred to as "optical Moore's law" [5]. The majority of existing optical devices is produced within a narrow application range and, therefore, requires further development of technologies to integrate more and more functionality. Obviously, a clear demand for not just large-scale integration, but also for more advanced devices materializes.

A great variety of active and passive devices, such as lasers, detectors, waveguides, switches, and modulators can be constructed on a single chip using photonic crystals (PhC). Photonic crystals allows realization of ultra-compact high-efficiency all-optical data processing [6] since

they tightly confine light in an ultra-small volume around wavelength sized. These structures, therefore, can be applied in many areas, where manipulation of light is essential.

1.2 Photonic crystals

The idea behind photonic crystals is realization of artificial crystals, which can manipulate the flow of light. In 1887 Lord Rayleigh discovered that a one-dimensional (1D) periodic structure has a photonic bandgap (PBG) [7] – a range of forbidden wavelengths for propagation. In dielectric structures with a periodic refractive index contrast, photons, similar to electrons in solid crystals in periodic potential, experience periodic perturbation. In 1987 the attention given to photonic crystals has grown after works published by Eli Yablonovitch [8] and Sergeev John [9]. E. Yablonovitch tried to improve telecommunication lasers [10] by searching ways to suppress spontaneous emission (SE), while S. John wanted to localize light in a disordered medium.

Nature illustrates PhC through, for instance, opal gems [11], the peacock's tail [12] and butterfly wings [13]. Light diffracts, for example, in opal due to its closely packed silica spheres microstructure that originates iridescence. Natural photonic crystals have an uncompleted three-dimensional (3D) band gap. For artificial counterparts, in spite of the demonstration of 3D PhC [14]–[18], the fabrication process is challenging as a result of the critical need of state-of-the-art equipment with a high precision alignment module. Thus, to date, the most attractive candidates are two-dimensional (2D) structures, such as air-suspended slabs/membranes. The technology to create them is taken from the silicon microelectronic industry, i.e. lithography and etching techniques. The term "photonic crystals" is mostly applied to 3D or 2D structures, however the 1D type of photonic crystals, named Bragg reflectors, are of much use for distributed feedback (DFB) lasers and dielectric mirrors.

Now focusing on PhC slabs, photons are confined in plane by Bragg reflection of a periodic PhC structure. The confinement in the third direction (out-of-plane) is achieved by total internal reflection (TIR) because a membrane is surrounded by low-index material (e.g. air). The thickness of a semiconductor membrane, in general, is on the order of $\lambda/2n$, where λ is the wavelength and n is the refractive index. Varying topologies of a dielectric lattice allows creation of band gaps for different polarization of light for such as transverse electric (TE) or transverse magnetic (TM) modes. A hexagonal lattice is widely used due to the presence of the largest 2D PBG in TE-polarization (the electric polarization parallel to the 2D plane) [19].

The photonic crystal slabs benefit from introducing a defect [20] or a break in the periodicity [21] so additional modes appear into the band gap region. By removing a single hole (figure 1.1 (a)) or several holes (figure 1.1 (b)), ultra-small optical microcavities can be made. A missing row of holes allows guiding light from one point to another (figure 1.1 (c)).

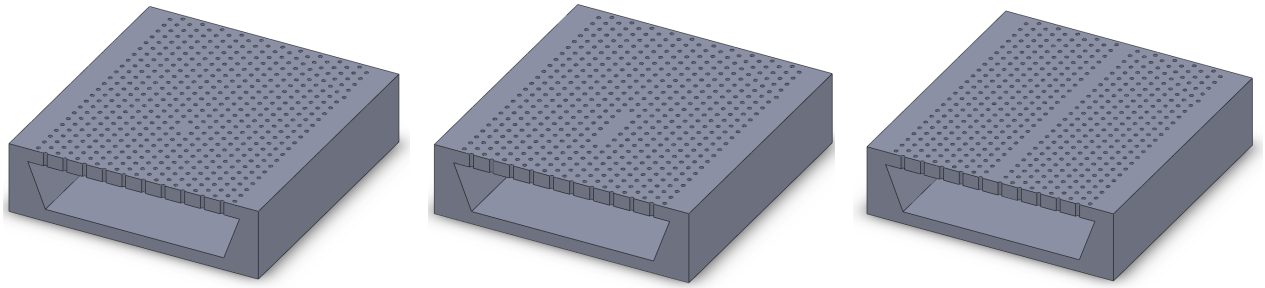

(a) (b) (c)

Figure 1.1: L1 microcavity (one missing hole) (a), L5 microcavity (5 missing hole) (b), and W1 waveguide (c) made in a 2D photonic slab

To characterize PhC cavities two parameters: the quality factor (Q) and the mode volume (V), are used. The quality factor is defined as $Q = \omega/\Delta\omega$, where ω is the resonance frequency. In 2D PhCs the total quality factor can be separated into: in-plane and vertical components $1/Q_{tot} = 1/Q_{\parallel} + 1/Q_{\perp}$. Despite no well-standardized definition of mode volume, it, however, demonstrates how well modes are confined inside the PhC cavity. High-Q cavities with small volume can increase the light-matter interaction that leads to high performances in optical devices, particularly in the low threshold lasers. Anther appealing aspect of photonic crystals is the possibility to slow light down. The development of semiconductor and epitaxial technologies opens up possibilities for combination of PhC with epitaxially grown nanostructures.

1.3 Epitaxial technologies

In the last decade epitaxial technologies have become the workhorse in the fabrication of electronic and optoelectronic devices. The term epitaxy originates from the Greek language and means that the deposited layer inherits the crystalline structure of a substrate. These layers can be produced by a number of different methods called liquid-phase epitaxy, molecular beam epitaxy, vapor phase epitaxy, especially the subtype metalorganic vapor-phase epitaxy.

At the early stage of the epitaxy era, liquid phase epitaxy (LPE) was a widely applied method to obtain epitaxial layers (epilayers). Employing this method, a breakthrough in optical material fabrication was realized, when the first lattice-matched AlGaAs/GaAs laser, which was able to work at room temperature, was demonstrated [22]. A crystalline layer is grown from a liquid phase on a solid crystalline substrate with conditions near thermodynamic equilibrium resulting in the migration of atoms to the energetically favorable position (step sites or kinks) for incorporation [23]. In this manner, the crystalline material has low density of dislocations and point defects. Despite the fast deposition, with growth rates up to 1 μm/minute, the inability to produce abrupt interfaces and the limited ability to grow certain materials reduced the demand for this method. Outside the manufacture of wide band compound radiation detectors LPE is not widely used today.

When abrupt interfaces are demanded, as in quantum wells growth for example; another method called molecular beam epitaxy (MBE) is often employed. The discovery of this

technique opened up the possibility of improvement in the quality of GaAs layers [24] and fabrication of the superlattice structures. Under ultrahigh vacuum conditions, the source molecules are transported to the growth interfaces by molecular beams. The ultrahigh vacuum allows applying of in-situ surface monitoring via reflection of high-energy electron diffraction (RHEED). Nowadays, MBE is a powerful tool in fabrication of semiconductor devices such as transistors, lasers and light emitting diodes (LEDs). However, the chamber under ultrahigh vacuum operates at huge expense and gives slow growth rates (around 1 μm/hour). In addition, the difficulties in growth of phosphorus-containing materials hinder the manufacturing application.

The third type of epitaxial method presented works with vapor sources and can be divided into three subtypes by the chemistry of the precursors: chloride vapor phase epitaxy (ClVPE), hydride vapor phase epitaxy (HVPE), and metal-organic vapor phase epitaxy (MOVPE) that sometimes called as metal-organic chemical vapor deposition (MOCVD). The first two approaches are no longer common, in particular, ClVPE is not mentioned in the contemporary scientific articles, but HVPE equipment can be found among some research labs and a few commercial companies.

Contrary to the material limitations of other tools, MOVPE allows the growth of III-V, II-VI, IV-VI, IV-IV compounds in a large scale with relatively low costs. The underlying foundation of this method lies in a process described in the late 1960s by H. Manasevit [25], who investigated the deposition of III-V materials on a heated substrate using metal-organic gases. In this approach, the deposition of semiconductor compounds occurs from a chemical reaction of metal-organics and hydrides species. An important aspect of MOVPE is the possibility to realize selective area growth, which is essential in fabrication of novel optical devices. The high crystalline quality of produced layers in thickness from a monolayer (few Angstroms) to several micrometers drives the implementation of this method not only among private sector, but also in academia.

1.3.1 Selective area growth

Selective area growth on a nanometer scale represents enormous potential for the fabrication of novel devices such as ultra-compact photonic crystal cavity lasers with the lowest power consumption [26], [27] or single photon emitters consisting of, for example, an individual QD as an active medium [28]. Currently, the technology is based either on post-growth etching of active layers used in buried heterostructure lasers [29] or mesa etching followed by non-planar growth [30], [31]. Both methods rely on ex-situ surface treatment prior to regrowth and, therefore, suffer from defect formation on the grown interface due to unavoidable contamination and surface damage. Eventually, this lowers the optical properties of the material and degrades device performance more and more as dimensions become smaller. Alternatively, the ridges can be grown on a planar surface [32], that does, however, require an additional overgrowth step to make surface planarization [33].

The selective area growth (SAG) technique requires a protection mask of a desirable shape, e. g. using silicon dioxide or silicon nitride [34]–[36]. In 1966 Shaw [37] investigated epitaxial deposition in etched holes in a GaAs substrate and obtained single crystals of the excellent quality. The selective growth is based on the restriction of reactant absorption on the patterned region [38]. The restriction of deposition on the semiconductor region under the mask could be a benefit in large-scale integration where passive and active components are integrated on a single chip.

Furthermore, the SAG approach developed in this work can, in principle, be applied for the fabrication of an array of identical quantum dots (QDs). A widely used method of QDs growth is Stranski-Krastanov growth (self-assembled QDs) that causes non-uniformity in size, strain distribution and material composition of QDs. All these factors contribute to the inhomogeneous broadening of an emission spectrum. Selective area growth, therefore, is necessary to establish the position and shape control of active material. Since the position of the active medium in the cavity influence on light-matter interaction, the control of the active material placement is essential in the fabrication of active PhC devices.

1.4 Active photonic crystals

By introducing quantum heterostructure into PhC both photon [39] and electron properties can be controlled in such structures. In 1946 Purcell implied that the placement of an atom in a lossless cavity allows the modification of the spontaneous emission [40]. Engineering active photonic crystals leads to lower threshold operation, higher modulation rates, and increased integration capacity.

One of the most essential elements of any optical transmission system is a laser, which has to have high injection efficiency and low operation power [41]. Novel constructed DFB lasers for 100 Gb Ethernet operates with the energy cost of thousands of fJ/bit [42] due to a relatively large cavity area on order of hundreds μm^2. The energy cost is reduced in vertical cavity surface-emitting lasers (VCSEL) that are widely used in short distance telecommunication network. Their emitting aperture is around few μm [43]; however, further scaling down is difficult when one needs to maintain high reliability. A new step in low current lasers for inter-chip and intra-chip application is a current-injected lambda-scale embedded active region photonic-crystal (LEAP) laser with a 4.4 fJ/bit operating energy [26].

In 1999 the first III-V active photonic crystal laser was demonstrated with the cavity designed as a single defect microcavity having Q=250 [44]. This laser was fabricated in an indium gallium arsenide phosphide (InGaAsP) membrane. An air-suspended PhC membrane made in InGaAsP compounds suffers from a heating issue. The heat cannot dissipate due to air cladding, preventing CW pumping or limiting the output power [45]. To overcome this issue, the active material needs to be firstly shortened only to the area where the gain material is needed and then buried in an InP membrane. An example of such structure developed by Nippon Telegraph and Telephone Corporation (NTT) for off-chip and on-chip data transmission is shown in figure 1.2.

As a consequence of higher thermal conductivity of InP in comparison to its quaternary or ternary alloys, pumping under the continuous wave regime is feasible. In addition, the pumping spot is determined by the active volume and not by the pumping beam. Thus, less unwanted absorption of the pump light outside the cavity is provided. Furthermore, InP membranes can operate in continuous wave mode at room temperature and can be efficiently coupled with passive waveguides for optoelectronic integrated circuit applications.

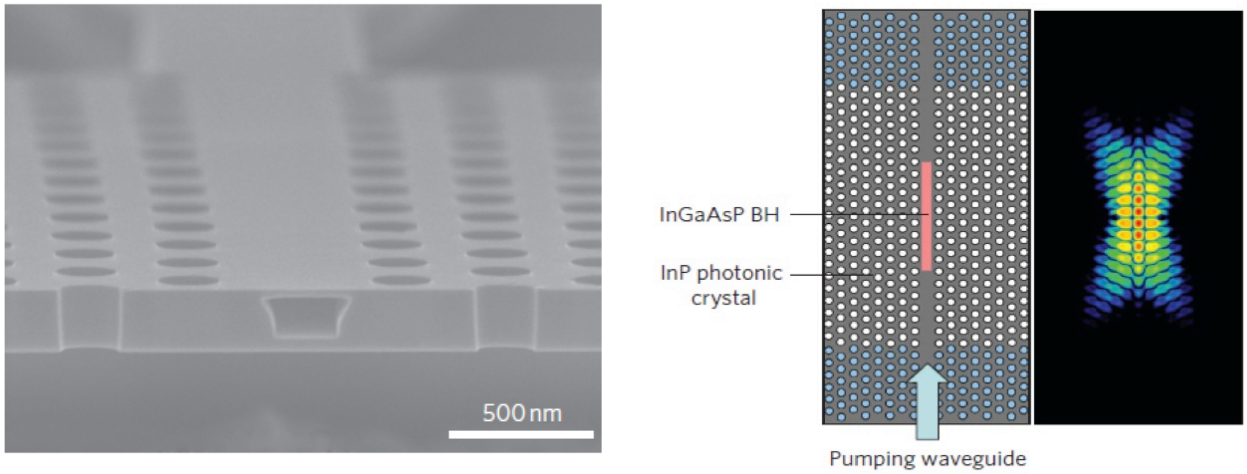

(a) (b)

Figure 1.2: SEM image of the cross-sectional geometry of buried heterostructure photonic crystal nanocavity laser (a), field profile of the structure calculated by FDTD. Taken from [29].

Including a smaller active medium into PhC cavities requires changes to the growth process to fit into the cavity/waveguide area. The buried quantum wells depicted in figure 1.2 were fabricated applying butt-join integration of selective growth. In this method, the active material is first grown, then the undesired material is removed using mask patterning and further etching, finally a cap layer is overgrown to planarize the top surface. A drawback of this approach is the defect incorporation into lateral interfaces during the etching and regrowth steps. In addition, ex situ patterning and etching make the whole fabrication process longer and more complicated.

Speaking about material, InP possesses a relatively lower surface recombination compared to GaAs [46]. Low surface recombination permits the overwhelming of non-radiative recombination states, which may dominate over radiation recombination in nanodevices. In addition, the emission wavelength of quaternary or ternary compounds lattice matched to InP can be designed at 1550 nm where C-band is centered with the minimal attenuation of silica fibers.

1.5 Thesis outline

The object of this work has been the demonstration of photonic crystal slabs with a selective area grown active medium for application in telecommunication systems. The important aspects were investigation of MOVPE selective area etching using CBr_4 and investigation of HSQ e-beam resist parameters for the use as a mask for selective area growth. The fabrication process was

developed to combine different patterns made by electron beam lithography. The study is divided into four main chapters and introduction, conclusions and two appendices.

Chapter 2 provides a description of MOVPE technology and basic features of photonic crystals. Selective area growth is reviewed with the attention given to growth enhancement and compositional deviation, especially, when growing on non-planar surfaces. The impact of design on PhC dispersion and slow light effect are addressed.

Chapter 3 is devoted to the fabrication of SAG InGaAs/InP QWs in nanometer/submicron openings. Optimization of an HSQ mask to grow heterostructures with high optical quality was performed. The surface preparation using sulfuric acid was investigated with the SA mask. MOVPE selective area etching and growth are demonstrated.

Chapter 4 introduces the fabrication process for incorporation of the developed material into InP membranes. Optimization of alignment marks to decrease the fabrication error is presented. An overview of the process flows is given.

In chapter 5 the experimental characterization of SAG QW by various methods, such as scanning transmission electron microscopy (STEM), cathodoluminescence and photoluminescence, is presented. The intermixing of the components is observed by STEM. Dependences on the opening sizes and width of the mask are evaluated by PL measurements. Finally, the amplified spontaneous emission of the fabricated photonic crystal waveguides and long cavities with a selective area grown QW developed in this thesis is demonstrated.

Chapter 2. Basic concepts

This chapter discusses some basic theoretical aspects of MOVPE and photonic crystals. Wherein, in the first section, the focus is on significant aspects of MOVPE, such as hydrodynamics, thermodynamics and kinetics. In the second section, basic electrical and optical properties of semiconductor heterostructures are outlined. The third section is centered around the essential selective area growth approach where the subject of inquiry is growth enhancement and compositional deviation. Specifically, selective growth on non-planar surfaces is discussed in the following subsection due to anisotropic behavior of InP growth. The last section is dedicated to the design of photonic crystals waveguides and lasers. Particular attention is paid to the slow light phenomenon and nanolasers.

2.1 MOVPE growth

MOVPE growth is a widespread method for fabrication of thin layer stacks; meanwhile, it is a complicated technique, which requires analysis of hydrodynamics, thermodynamics, reaction mechanism and kinetics aspects. In order to satisfy needs and desires of material quality, both reactor configuration and growth parameters demand careful analysis. Generally speaking, MOVPE reactors can have either vertical or horizontal geometry. Particularly, this work was carried out in an Emcore Discovery 125 MOVPE vertical-reaction chamber. During manufacturing process, the reactor configuration should be optimized in such a way to diminish edge effects and buoyance that can give less abrupt interfaces. Furthermore, the thickness uniformity and constant composition distribution over a substrate [47] can be improved by utilizing the rotating disc reactor (RDR) concept. The background and the main apects of the RDR concept can be found in [48]–[52].

Figure 2.1 (a) shows a schematic illustration of the employed reactor chamber. An epiready wafer is placed on a spinning susceptor with the resistive heater underneath. Using a thermocouple, a temperature of a wafer holder can be determined; however, the measured value is different from the wafer temperature itself. For this reason, a high-speed infrared pyrometer is also applied to accurately monitor the temperature in a 500º-850º C range. To grow the prominent III-V semiconductors, the typical organometallic compound for group III are trimethylindium (TMIn), trimethylgallium (TMGa), and trimethylalluminium (TMAl) or the methyl-radical can be exchanged by the ethyl-radical. The alkyl sources are, in general, liquids (expect for solid form of TMIn) stored in stainless-steel bubblers, which are kept in bathes at constant temperature and pressure. Hydrides, such as arsine (AsH_3) and/or phosphine (PH_3) gases, are frequently used as group V elements. To deliver the components to the growing interface, hydrogen as a carrier gas (or alternatively, nitrogen) is blown through the bubblers

whereas it takes the precursor molecules. The mass flow controllers measure the essential amount of precursors. The primary component of the total flow in the reactor is the carrier gas with a relatively small amount of precursors. The delivery system involves a complicated vent-run configuration, which help prevent pressure changes between the vent and run lines to enhance the reproducibility of the process [53]. Before entering the growth chamber the input gases are premixed in the separate manifolds for the III group and V group elements to minimize parasitic reactions between them in the vapor phase. Under constant thermal conditions, the injection through the flow flange zones ensures the uniform deposition.

Inside the chamber, the input gases move in a laminar flow until they reach the specific height above the disc called a boundary (stagnant) layer, which describes a region where the temperature and velocity components change rapidly (figure 2.1 (b)). When precursors come closer to the spinning disk, the gas flow picks up circumferential and radial velocity components and the axial velocity reduces to zero at the surface. Above the surface, the incoming precursors break apart under the high temperature condition and the gas-phase diffusion is determined by temperature and concentration gradients. The molecules and atoms arrived to the surface can directly incorporate or can migrate until they find the energetically favorable place, such as step sites or kinks, and incorporate there; or can desorb back into gas phase. Eventually, unused products are removed through the exhaust located in the base of the chamber. Even though RDR involves complex flow dynamics, the mass and heat transport is not dependent on the rotating disc radius to the first order which makes the concept attractive [52].

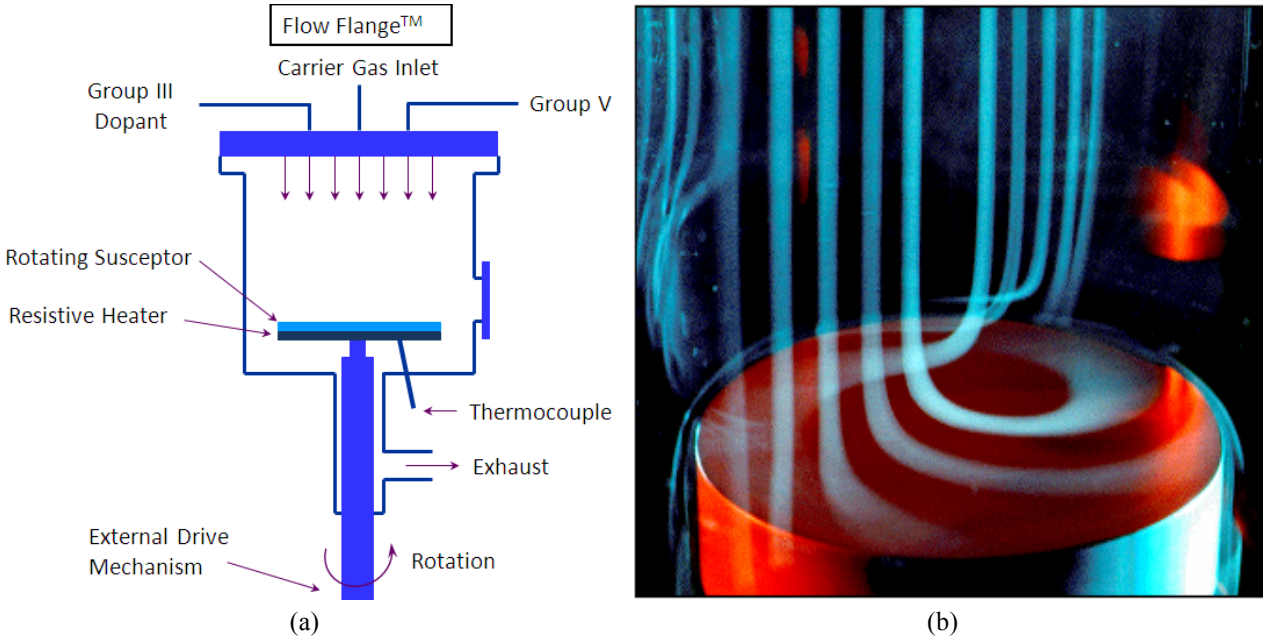

Figure 2.1: Sketch of the growth reactor (a) and flow visualization in the RDR (taken from [54]) (b)

The basic reaction of MOVPE is pyrolysis, or in other words thermal dissociation, which gives the atomic species of organometallic compounds and gaseous hydrides. The simplified reaction including pyrolysis is expressed as:

$$R_3A + BH_n \rightarrow AB + nRH \tag{2.1}$$

where R is an organic radical, A and B are the involved species. In particular, the reaction for InP is given as:

$$(CH_3)_3In + PH_3 \rightarrow InP + 3CH_4 \tag{2.2}$$

where $(CH_3)_3In$ is TMIn and CH_4 is methane. Pyrolysis, in practice, is not a simple process implicating intermediate steps, such as source molecule fragmenting involving step-by-step loss of methyl radicals. These reactions can occur entirely in the vapor (homogeneous) or on the surface (heterogeneous) making the MOVPE process even more complicated. Moreover, the surface nature, including reconstruction, defects and atomic steps, has a tremendous effect on the heterogeneous chemical reactions, and more importantly on growth rates. As shown in figure 2.2 (a), the presence of the catalyzing surface change the pyrolysis efficiency of some fundamental hydrides [53]. The decomposition temperature of PH_3 decreases by more than 300 ºC in the presence of an InP substrate (closed circles) compared to an empty quartz tube (open circles). Similar behavior was observed for AsH_3, but with use of a GaAs substrate as a catalyst. The surface reduces the bond of arriving molecules leading to better incorporation. For the group III species, the catalyzing surface has a little impact on pyrolysis efficiency. The decomposion of TMIn happens at lower temperature than TMGa (figure 2.2 (b)). Compared to group V hydrides, the effective temperature of alkyls is lower and the curve is steeper, indicating faster pyrolysis in a shorter temperature range. Thereby, the pyrolysis mechanism is different for group III and V due to surface catalysis effect. Analysis of pyrolysis is important not only for hydrides, but also for metal alkyls as, for example, heterogeneous pyrolysis of TMGa is slow in the lack of AsH_3 [55].

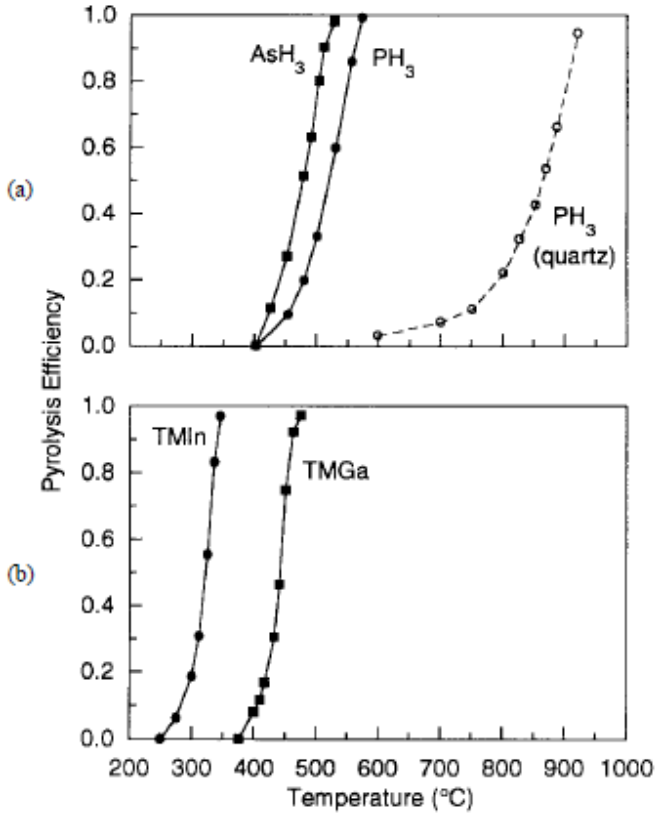

Figure 2.2: Pyrolysis efficiency of group V (a) and group III (b) species taken from [53]

Apart from a strong influence of a surface on the pyrolysis efficiency, species of group V are highly volatile, which manifests in a lower incorporation of them into a growing film. Thus, III-V alloys are produced with large excess of group V or, to put it another way, with V/III partial pressures ratio greater than unity. When growing at high overpressure of hydrides, the elements of group III are efficiently depleted at the interface with no impact on the stoichiometry of solids. However, an excess of the metal alkyls can form a second liquid phase on the surface. Furthermore, nonvolatility of some reaction products notably carbon-containing compounds can give rise to contaminations.

With regard to the growth temperature, two regimes are identified where the deposition can be constrained by interface kinetics or diffusion kinetics. At low temperatures, when pyrolysis of the III group is not completed, the reaction limited regime is observed until 500 ºC [38]. By raising the temperature, transport becomes independent on the substrate temperature meaning the precursor diffusion toward the surface is slower than the occurring reactions. This is called the mass transport limited regime. Working under this condition for III-V materials is preferable due to a small impact of temperature gradient. Above 750º C, the higher the growth temperature is, the slower growth rates are due to parasitic reaction between alkyl and hydrides and increased desorption.

Practically, when growth occurs at the mass transport limited regime and gas-phase reactions are neglected, growth rates and composition are proportional to the flow rate of the III group

constituents assuming their incorporation rate is equal to the unity. For the III sublattice in a ternary alloy, the growth rate is the sum of the binary growth rates [53]:

$$g_0 = (A_1 F_{TMGa} + A_2 F_{TMIn}) \frac{p_{total}}{F_{total}} \tag{2.3}$$

where A_1 and A_2 are constants determined empirically, p_{total} is the total pressure in the reactor, F is the flow of components and the total flow respectively. Wherein, the flow rate of metal alkyl through the bubbler can be expressed as [52]:

$$F_{metal\ alkyl} = \frac{\varepsilon F_{hydrogen} p_{metal\ alkyl}}{(p_{bubbler\ total} - p_{metal\ alkyl})} \tag{2.4}$$

where ε is bubbler efficiency and p_i, F_i are the partial pressure and flow of a component *i*. Simultaneously, growth rates are measured in-situ by a laser-based reflectometer. The flux of the diffusion through a boundary layer of δ_0 thickness is expressed as:

$$J = \frac{D_{In}(p^*_{In} - p^i_{In})}{RT\delta_0} \tag{2.5}$$

where D_{In} is a diffusion coefficient, p^*_{In} is the pressure of the input gases, p^i_{In} is the interfacial partial pressure. The equilibrium constant to form solid InP is defined as:

$$K_{InP} = \frac{a_{InP}}{p^i_{In}(p^i_{P_4})^{1/4}} \tag{2.6}$$

where a_{InP} is an InP lattice parameter. The composition of solid is proportional to the ratio between growth rate of one constituent and the total growth rate. For example, the composition of $In_{1-x}Ga_xAs$ can be determined from:

$$x = \frac{J_{Ga}}{J_{Ga} + J_{In}} = \frac{D_{Ga} p^*_{Ga}}{D_{Ga} p^*_{Ga} + D_{In} p^*_{In}} \tag{2.7}$$

To produce materials of high purity and good morphology, growth parameters need to be determined empirically due to extreme complexity of the MOVPE process. The optimal values, generally, are constant; however, they require recalibration with time or after the growth chamber or sources maintenance.

Working with the group III favors low-pressure conditions (10-80 Torr) to result in a smaller amount of parasitic reactions. At fixed input molar flows, the amount of collisions of each molecule in the gas phase decreases when the reactor pressure goes down. As a consequence, the pyrolysis rate is reduced and sharper interfaces can be obtained. Experiments at low pressure is interesting for selective growth as well because, according to Dupuis et al. [56], growth

enhancement in the area near a mask can be diminished with pressure reduction. In the used reactor, the pressure alteration is a quite complicated task due to recalibration of all parameters to keep a safe distance for incoming precursors. Aiming for production of light sources, not only physical and chemical processes in the reactor require consideration, but also the connection between fabrication process and material properties need to be established.

2.2 Semiconductor heterostructures

Sequential epitaxial growth of two semiconductors with different electronic properties allows engineering a heterostructure. Based on III-V compounds, a variety of materials can be combined into a heterostructure to manipulate a band gap, or the corresponding wavelength, which is plotted as a function of a lattice constant in figure 2.3. In this work, the compound of interest is InP and by the white line the lattice-matched compounds are highlighted and in particular, the composition of $In_{1-x}Ga_xAs$ needs to be x=0.467. Transitions from a direct to an indirect semiconductor, due to a crossing of the lowest Γ, X and L conduction bands, are shown by dash and compound lines.

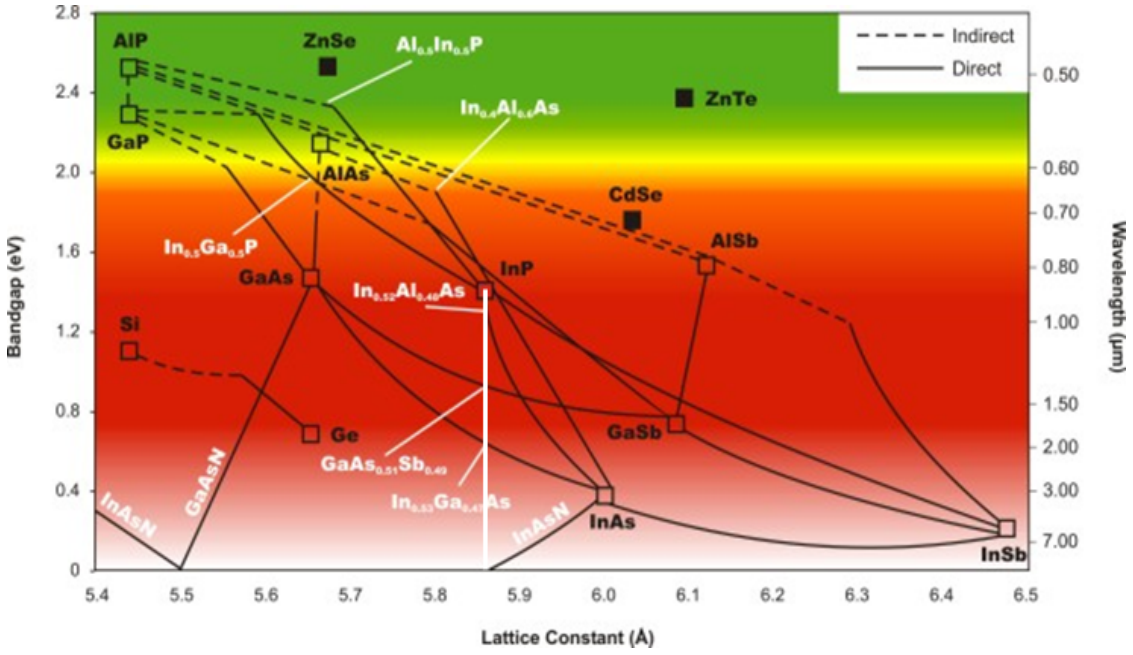

Figure 2.3: Band edges as a function of lattice parameter. Along the straight white line is shown the InP lattice constant and the composition of InGaAs lattice-matched to it. Taken from Veeco website http://www.veeco.com/promos/lattice-parameter-and-bandgap-data.aspx.

The lattice constant of ternary compounds can be calculated using Vegard's law as:

$$a_{alloy} = xa_A + (1 - x)a_B, \tag{2.8}$$

where a_A and a_B are the lattice constants of the binary compounds A and B. When the difference in lattice constants between the substrate and depositing film are less than 1%, the film inherits an in-plane lattice constant of the wafer without formation of structural defects. If this mismatch increases, strain can arise in the epilayer without development of defects when the layer thickness is less than the critical thickness (pseudomorphic growth). Continuing to grow above the critical thickness leads to plastic strain relaxation via surface bending and crystal defects formation, which play a role of recombination centers reducing the luminescence intensity and broadening the spectrum linewidth.

Using a simple quadratic form [57], the connection between alloy composition of ternary and the energy gap is described as:

$$E_g(A_{1-x}B_x) = (1 - x)E_g(A) + xE_g(B) - x(1 - x)C, \tag{2.9}$$

where A and B are the binary compounds, C is the bowing parameter, which is the deviation from a linear interpolation. The composition of a compound has a similar effect on refractive index and can be described in the same way as in the equation (2.9). The variation in composition, therefore, leads to graded interfaces due to variation not only in the band gap but also in the lattice constant. When chemical transition assumed to be abrupt, then the potential and band transition is considered to be abrupt too.

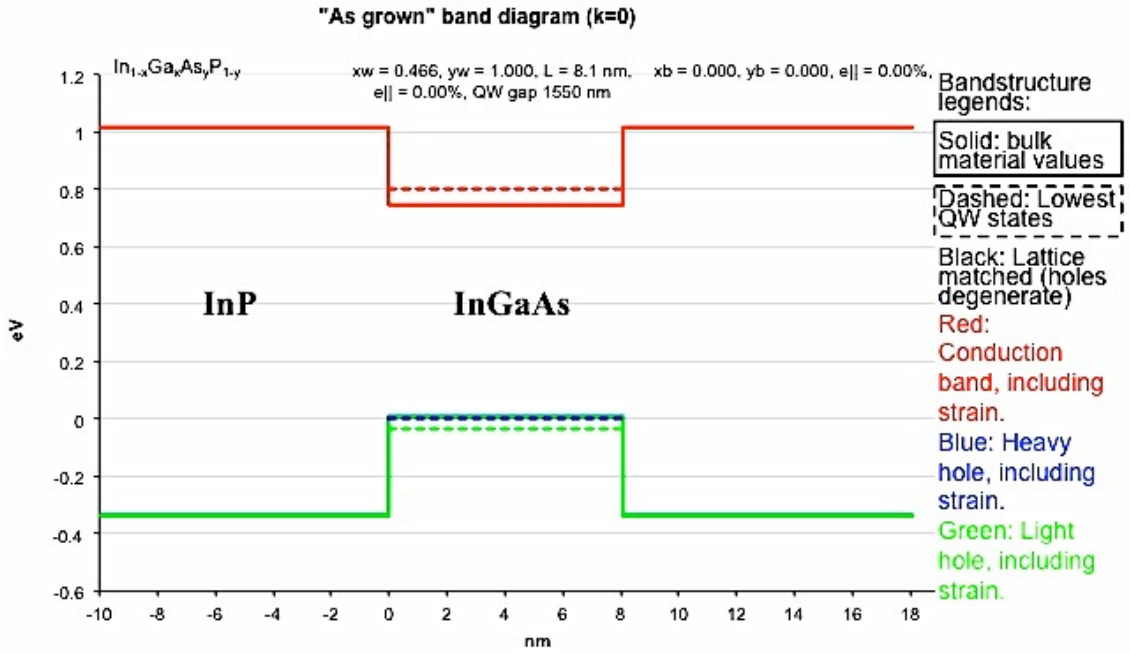

Figure 2.4: Band gap diagram of InGaAs/InP QW emiting at 1550 nm and represents the type I of the bands alignment

The alignment of the band gaps of the heterostructures affects physical properties of the devices. The valence and conduction bands can be aligned in three ways: straddling gap (type I), staggered gap (type II) or broken gap (type III or sometimes refer as type II b). In the first type the conduction and valence bands within the bandgap restricts both types of carriers. Type I is plotted in figure 2.4 exemplified by a double heterostructure of InGaAs/InP. Additionally, AlGaAs/GaAs and InAs/GaAs possess this type of alignment. For staggered type, the steps in the valence and conduction bands go in the same direction. An example of this type is GaSb/GaAs materials. The broken band alignment has the bands, which do not intersect, so the band lays above/below of the conduction band/valence band of another semiconductor. A material having this type of interface is InAs/GaSb.

The optical properties of semiconductors with a direct band gap are determined by the transition from the conduction band to valence band. Thus, a photon is emitted through the radiative recombination process of an electron-hole pair (exciton). Now considering the energy of a quasi-single electron confined in the potential barrier of the crystal of L_x, L_y, L_z dimensions. The electronic properties of the crystal can be calculated in the framework of the effective mass approximation. Assuming the zero potential (W=0) inside the crystal of L_x, L_y, L_z dimensions the Schrodinger equation can be written as:

$$\frac{-\hbar^2}{2}\left(\frac{1}{m_x^*}\frac{\partial^2}{\partial x^2}+\frac{1}{m_y^*}\frac{\partial^2}{\partial y^2}+\frac{1}{m_z^*}\frac{\partial^2}{\partial z^2}\right)\psi(r)=E\psi(r) \tag{2.10}$$

where m^* is the effective mass of electrons along three directions x, y, z, $\psi(r)$ is a wave function, $\hbar$ is the Plank constant. Assuming the boundary conditions as $\psi(x \pm L_x, y, z) = \psi(x, y, z)$, the solutions for the wave function and eigenenergies are

$$\psi(r)=\frac{1}{\sqrt{V}}e^{i(k_x x+k_y y+k_z z)}, \tag{2.11}$$

$$E_k=\frac{\pi^2\hbar^2}{2m_x^*L_x^2}n_x^2+\frac{\pi^2\hbar^2}{2m_y^*L_y^2}n_y^2+\frac{\pi^2\hbar^2}{2m_z^*L_z^2}n_z^2 \tag{2.12}$$

where V is the volume of the bulk crystal. So every electron state is described by discrete value of k. Different effective masses of holes and electrons lead to dissimilar shapes and depths of lateral confinement energy. A more accurate electronic structure can be calculated using multiband k·P method [57]. The energy separation of the electron and holes states defines the energy and wavelength of the emitted photon.

In bulk materials with continuous energy bands, the electrons and holes can move freely. When the physical dimensions become smaller than the de Broglie wavelength of electrons and holes, the quantum confinement starts to be seen resulting in quantization of the energy bands. By confinement of electrons and holes in the low dimensional structures, the enhanced optical output and high-temperature performance can be reached. The quantum confinement leads to the

modification of the electronic density-of-state (DOS), which describes the number of allowed states for electrons per interval of energy as:

$$g(E) = 2\times\frac{1}{V}\frac{dN}{dE} \tag{2.13}$$

where N is the number of electron states. In the bulk crystal the DOS is proportional to the square-root dependence of energy $\sqrt{E}$, which is plotted on the left side of figure 2.5. Now considering restriction of the electron mobility in one direction, elsewhere the electrons still can move quasi-free. Take, for example, an InGaAs/InP QW, which is the investigated structure in this thesis, the density of state for 2D case or for quantum wells is

$$D_{2D}(E_i) = \frac{m^*}{\pi\hbar^2} = \text{const} \tag{2.14}$$

which is staircase-like function. When the energy quantized along two directions z and y, the quantum wires are obtained and their DOS is illustrated in figure 2.5 for 1D case. Note that the peaks are not equidistant. If energy quantized in all three directions, then the zero-dimensional electronic DOS is observed which is a sum of δ-functions (the right picture in figure 2.5).

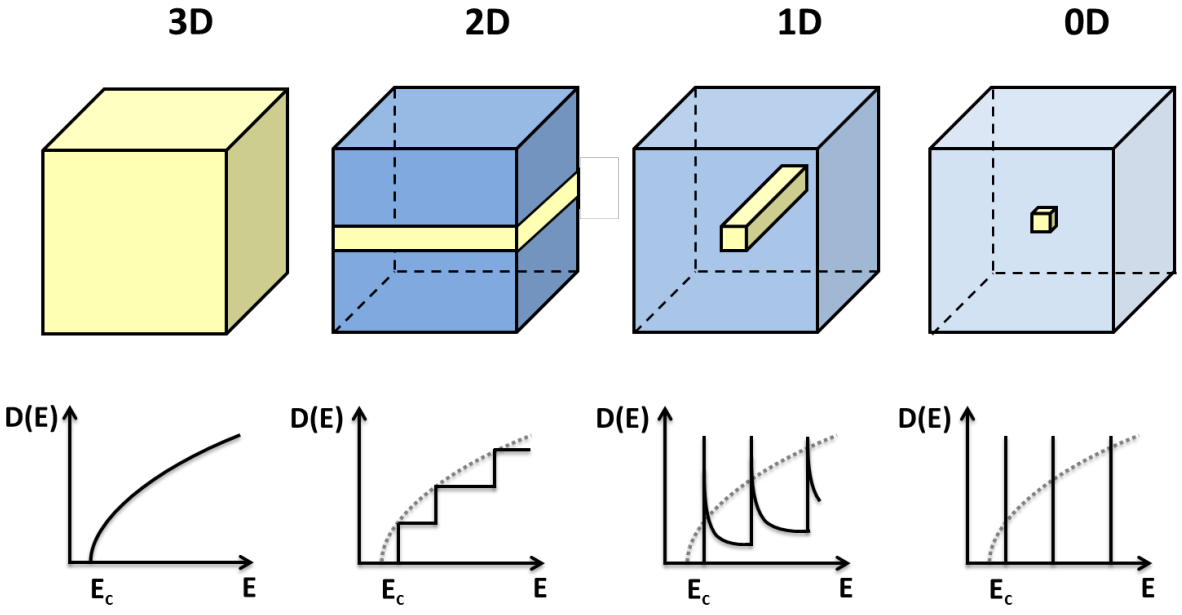

Figure 2.5: Electronic density of states *D(E)* in different dimensionalities: bulk semiconductor (3D), quantum well (2D), quantum wire (1D), and quantum dot (0D). E_c stands for the conduction band edge

To fabricate low-dimensional structures, more sophisticated approaches additionally to the classical epitaxial technologies can be applied such as selective area growth, which is described in the section below.

2.3 Mechanism of selective area growth

Selectivity in epitaxial growth is achieved by lateral patterning of III-V materials with silicon oxide/nitride. Also, the mask may be produced by HSQ electron beam resist [58], which allows precise positioning of a material and preventing an extra step in glass deposition (see section 3.1). Noteworthy to say, that the mask nature affects the adsorption-desorption kinetics above the patterned surface. The prevention of deposition on the mask forces an obtained excess of components to diffuse laterally toward open semiconductor regions. As a result, first, a thickness gradient is observed near the mask edges manifesting in non-uniform growth. Take, for example, a quantum well, where the consequences of growth enhancement can be seen as the thickness increase lowers the quantum levels, which causes a wavelength red-shift. Secondly, various diffusion rates of species emerge as composition deviation across the selective area as well as in the vicinity of a mask. Considering selective area growth of InGaAs/InP, the gas phase diffusion coefficient of In-containing species is higher than Ga-containing ones [59]–[61] and indium has higher bonding energy [62]. It is, therefore, expected to have In rich material in the selective areas. These two perturbations disappear on few tens/hundreds micrometers away from the pattern features [63]. Furthermore, the mask parameters, such as width and opening size, interplay on growth alteration in a way the wider the mask and the smaller openings are, the higher growth enhancement is. This deviation can be converted into fabrication of multi-wavelength laser diodes in a single growth run [64].

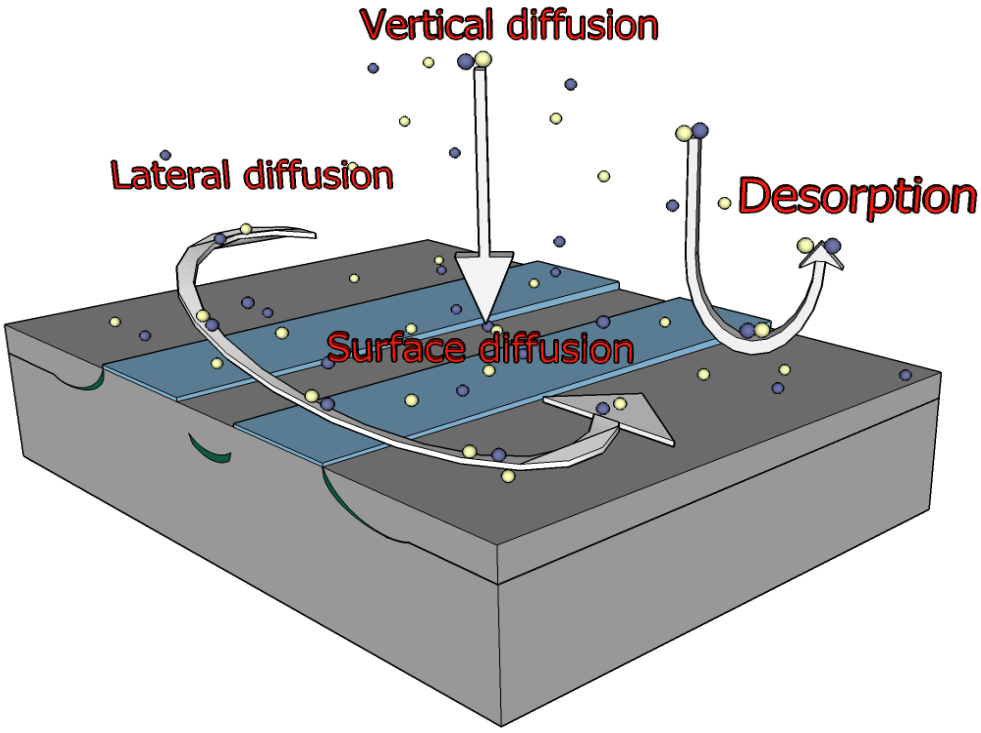

Figure 2.6: A schematic showing the flows near the surface

Selectivity can have its origin either in vapor phase diffusion or surface migration of involved components (figure 2.6). As mentioned above, the surface has a significant influence on the pyrolysis efficiency (see section 2.1); therefore, the precursors are not fully decomposed above the glass features [38] and so not adsorbed on the mask layer. The reagents come to the patterned area desorb back to the gas phase, collide with the molecules there and are redirected either towards an open semiconductor surface, where they can be adsorbed; or towards the mask, where they can again desorb back to the gas phase [63], [65]. However, a sticking coefficient of elemental species is high on the mask; thereby decomposed precursors can form a polycrystalline layer on the mask diminishing selectivity. On the basis of this, selective growth in MBE is unfeasible.

MOVPE growth is a complex approach and so not easily understood, and selective growth is even more convoluted. However, Gibbon et al. [36] suggested the simplified model to benefit device design simulation. The experiments in [36], [66] revealed that vapor phase diffusion is responsible for the excess growth rates, as a consequence, the presented model is based on diffusion of precursors in the gas. By solving the Laplace's equations, the concentration profiles can be calculated for both In and Ga species. Figure 2.7 illustrates the boundary conditions in the model. The boundary conditions were derived from first Fick's law for the masked area in assumption of no deposition and a combination of Fick's law and Langmuir isotherm for the semiconductor. On the border of the stagnant layer, the n concentration is considered to be a constant. Thus, the adjustable parameter is D/k, where D is the diffusion coefficient in the gas phase and k_s is a surface reaction rate constant (roughly proportional to the sticking coefficient) [67]. In Gibbon's work [36], D/k value was fitted to experimental data, thus it is dependent on a mask fill factor. In addition, the temperature was assumed to be constant over the calculation window as a result the diffusion coefficients are constant as well.

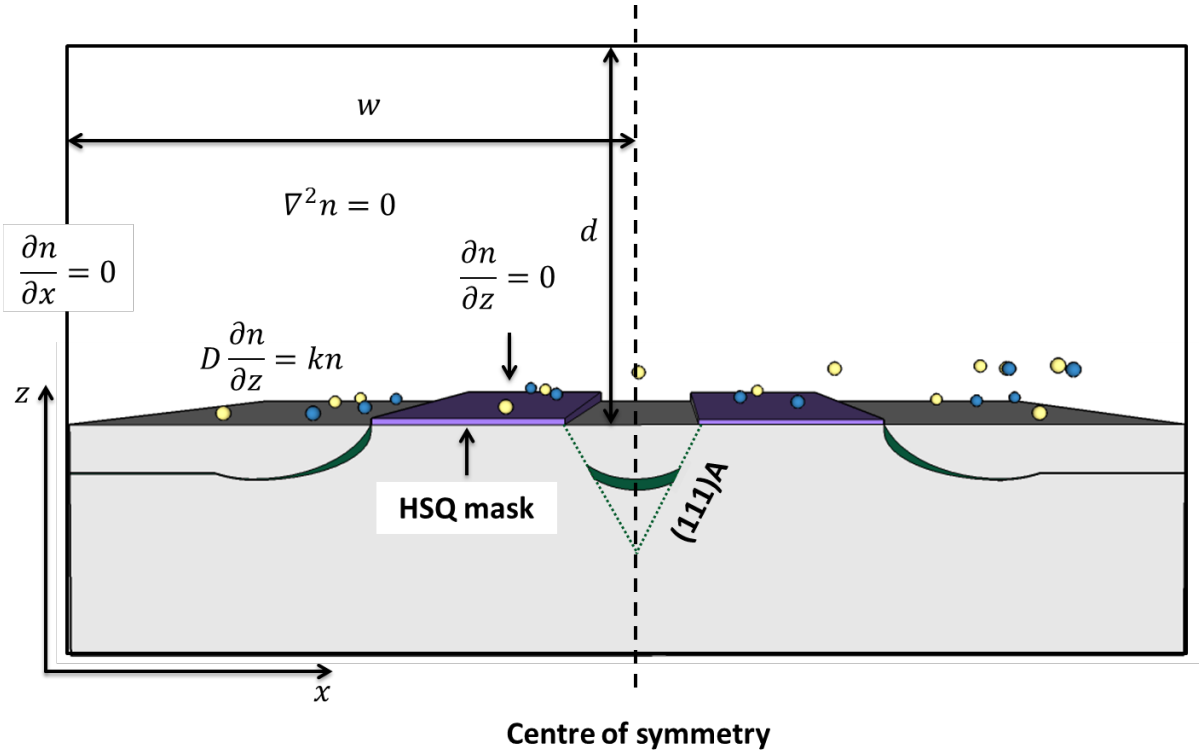

Figure 2.7: Boundary conditions in the model for SAG

The process parameters, such as a temperature, pressure and V/III ratio, have an effect on selective growth. By elevation of the temperature, the diffusion coefficient in the vapor phase and surface migration [56] are increased proportionally to $T^{3/2}$ due to a greater activation energy. Pyrolysis occurs faster with raised temperature leading to possibility of deposition of polycrystalline material on the mask, as mentioned above. The higher the pressure is, the smaller the diffusion coefficients are and more of the precursors decompose in the gas phase. In addition, higher pressure can contribute to increase of In content too [64]. Decrease in V/III ratio leads to the suppression of surface migration on the (100) plane.

2.3.1 Non-planar selective growth

Non-planar selective growth is an important approach for fabrication of novel optoelectronic devices as well as for understanding of fundamental aspects of selective epitaxy. Patterning of substrates in one more dimension can be realized, for example, by FIB etching [68] or by a combination of e-beam or photolithography and wet etching. Often, wet etching of InP or GaAs ends up in formation of self-limited structures called V-/U-grooves [69], [70], which allow fabricating quantum wires [71]–[73]. If InGaAs material is deposited in V-grooves, it is preferentially embedded inside the triangular bottom, but also a thin layer deposits on the sidewalls [74] that increases the injection efficiency [30].

Patterning a wafer in one or two dimensions affects the growth properties along different crystallographic orientations. In light of crystallographic dependent growth behavior, it is

important to understand the crystal structure of III-V semiconductor and especially InP. Commonly, indium phosphide, as many III-V semiconductors, possesses a zinc blende (sphalerite) lattice, where every atom bonds to four neighbors of another type. Overall, zinc blende consists of two interpenetrating face-centered-cubic lattices (fcc). Only III or V group atoms are contained in each sublattice with the shift of the relative sublattices of $a/4$, where a is the length of the fcc lattice constant. The absence of a center of inversion leads to different physical and chemical properties of InP along the [111] direction originated from crystallographic polarity. Deposition rates, therefore, are reduced on {111} planes, which contain either In ({111}A) or P ({111}B) atoms with one chemically active bond resulting in stability of chemical reactions [75]. Various incorporation rates of species on different crystallographic planes add further perturbation to the selective process although the slowly grown planes have a dominant influence. For example, Caneau et al. [76] reported that In composition in $In_{1-x}Ga_xAs$ increases on (111)B compared to (111)A.

The basic planes of InP are {001}, {110}, and {111}, besides these planes extra {311} planes are often observed during crystal growth. {311} planes are a stable intermediate facets composed of {111} steps and {100} terraces [77]. Planes with higher Miller indices can also be resolved on an atomic scale, which are formed by combination of basic {001}, {110}, and {111} planes. For cubic crystals, the angle ϕ between two planes $(h_1k_1l_1)$ and $(h_2k_2l_2)$ is given by:

$$\cos\phi = \frac{h_1h_2 + k_1k_2 + l_1l_2}{\sqrt{h_1^2 + k_1^2 + l_1^2}\sqrt{h_2^2 + k_2^2 + l_2^2}} \tag{2.15}$$

Therefore, applying reverse procedure by measuring an angle by SEM the crystal planes can be determined.

2.4 Design of photonic crystals

Photonic crystals are periodic structures, generally fabricated in 2D geometry by “drilling” holes in dielectric medium. The periodicity introduces a photonic band gap that prohibits the propagation of light at certain frequencies [8], [78]; as a consequence, effective confinement of light can be achieved. Therefore, this allows realizing ultra-compact cavities having volume in order of a cubic wavelength with a large quality factor (more than one million) [79]–[81]. The requirements of a large output power and a low operating energy can be satisfy by shrinkage of active material volume until the gain saturation compensates for a acceptable output signal [82]. Integration of selectively grown epitaxial layers in photonic crystals hence plays an important role. SAG material, also, allows switching from InGaAsP- into InP-based slabs that improves both thermal characteristics and devices efficiency. Furthermore, the possibility to slow down light propagated in PhC waveguides significantly attracts attention to these structures due to enhanced light-matter interaction. Finally, a combination of small optical sources with output waveguides on a single PhC chip using mature microelectronics technology carries the potential

for realization of all-optical processing, which is essential in integrated optics. Regarding the practical implement of all-optical functions in PhC, it is essential to control not only the design, but also the intrinsic material properties to avoid side effects. For instance, the requirements for both large output power and a low operating energy can be further satisfied by shrinking the active material volume to the sole part of the device where gain is required, hence reducing the area to be pumped [82]. In particular, such strategy is the key to reduce unwanted heating of the device.

In absence of free charges or electrical currents the propagation of light through PhC medium is described by four Maxwell's equations [83]:

$$\nabla \cdot \mathrm{H}(\mathrm{r},\mathrm{t}) = 0, \tag{2.16}$$

$$\nabla \cdot \varepsilon(\mathrm{r})\mathrm{E}(\mathrm{r},\mathrm{t}) = 0, \tag{2.17}$$

$$\nabla \times \mathrm{E}(\mathrm{r},\mathrm{t}) + \mu_0 \frac{\partial}{\partial \mathrm{t}} \mathrm{H}(\mathrm{r},\mathrm{t}), \tag{2.18}$$

$$\nabla \times \mathrm{H}(\mathrm{r},\mathrm{t}) - \varepsilon_0 \varepsilon(\mathrm{r}) \frac{\partial \mathrm{E}(\mathrm{r},\mathrm{t})}{\partial \mathrm{t}} = 0. \tag{2.19}$$

where H is the magnetic flux, E is the electric flux, ε is the dielectric constant, μ is the magnetic permeability, r is the position vector, and t is time. In addition, the displacement field D and the electric field E are interrelated as $\mathrm{D}(\mathrm{r}) = \varepsilon_0 \varepsilon_\mathrm{r} \mathrm{E}(\mathrm{r})$. The magnetic induction filed is related to the magnetic field via $\mathrm{B}(\mathrm{r}) = \mu_0 \mathrm{H}(\mathrm{r})$ in an assumption of μ_r=1. By applying algebraic methods and simplification of Maxwell's equations, the master equation can be obtained and expressed as:

$$\nabla \times \left(\frac{1}{\varepsilon(\mathrm{r})} \nabla \times \mathrm{H}(\mathrm{r}) \right) = \left(\frac{\omega}{\mathrm{c}} \right)^2 \mathrm{H}(\mathrm{r}) \tag{2.20}$$

where ω is the frequency and c is the speed of light. The speed of light in vacuum can be expressed as $\mathrm{c} = 1/\sqrt{\mu_0 \varepsilon_0}$. Solving the master equation gives access to the photonic band structure, where propagation wave vector k can be computed in terms of the frequency for the different eigen modes. For this purpose, two simulating techniques can be applied that are a Finite Differences in Time Domain (FDTD) [84] simulation and the method based on the plane wave expansions (available MPB software package [85]). That latter technique is especially well adapted to PhC waveguides because it takes advantage of the periodicity of the PhC. Indeed for periodic structures, the eigen modes are also periodic with the same periodicity and follow the Bloch-Floquet theorem which allow several simplifications. As a result, the band diagram of a-periodic structures is also periodic with periodicity $2\pi/\mathrm{a}$, and is usually expressed in units of the size of the PhC unit cell a.

Figure 2.8 (a) shows a dispersion diagram of a line defect waveguide in the first Brillouin zone $k = (0, \pi/a)$[1]. The frequency is normalized $\omega_{norm} = a/\lambda$. This scaling property is a huge advantage for PhC, because the working frequency can be easily adjusted simply by changing the lattice parameter a. In PhC waveguides, light is confined in the slab plane by Bragg reflection and vertically by total internal reflection. To confine light into a slab, the wave vector *k* needs to be greater than vacuum wave vector $k_0 = \omega/c$. The modes, which satisfy the condition of $k = k_0 c$, are lied inside the light cone (a grey shadowed area in figure 2.8 (a)) and suffer large intrinsic losses because they couple spontaneously to the free space [86]. At low and at high frequencies, the photonic band gap is delimited by two bands with a continuum of modes (blue lines). The modes at a low frequency part of the band diagram contain their energy in the high index region of the crystal and called the dielectric or slab modes. These modes are not confined inside the waveguide. The top part of the band diagram is called air modes.

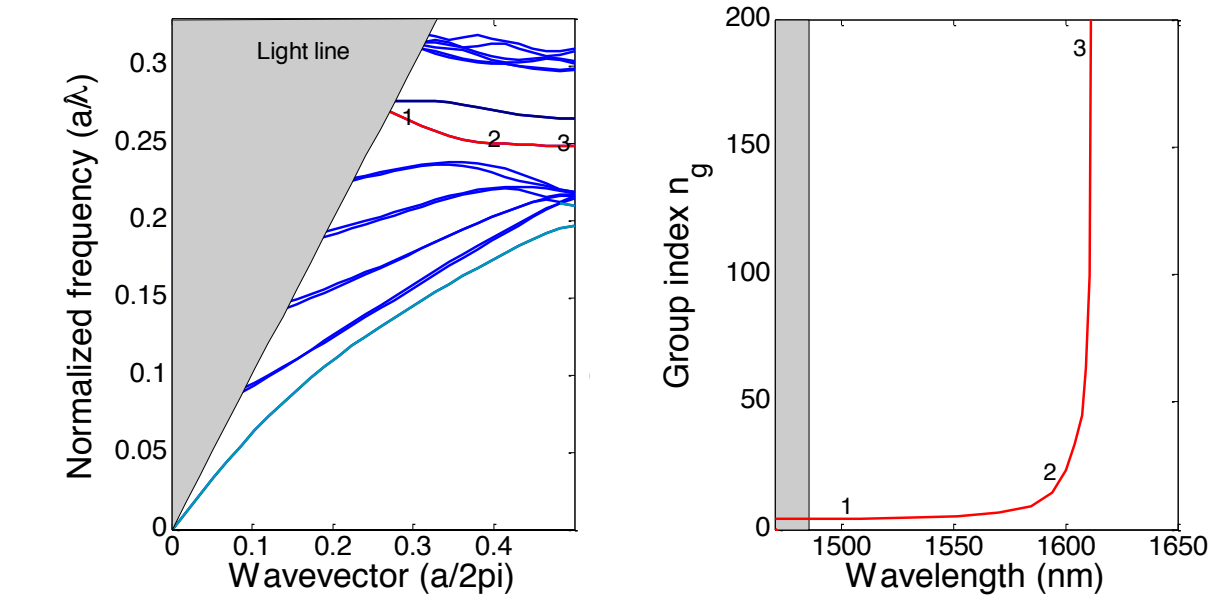

Figure 2.8: A dispersion diagram of a slab waveguide (a). The fundamental (even) mode is marked in red color. The group index of the fundamental mode (b). Electric field distribution for fast (1), intermediate (2) and slow (3) light (the bottom row). Taken from [87].

With regard to polarization, photonic band gap varies for TE and TM modes in 2D photonic crystals. However, slabs with a triangular lattice can provide bands for both types of the modes. The presented dispersion diagram shows TE polarization (electric field parallel to the the 2D plane, and magnetic filed is perpendicular to the slab). The TE mode has a bigger PBG than the

[1] The design of photonic crystal waveguides were done by Pierre Colman and Sara Ek; and PhC lasers by Yaohui Chen, Sara Ek, and Weiqi Xue.

TM mode and is also better confined inside the PhC waveguide. Thus this mode is often used for application. The attention still need to be paid to the TM and the higher orders modes as the imperfections, such as roughness and non-verticality of holes, can result into coupling of modes with different polarization into other waveguide modes. A single row of missing holes introduces a series of guided modes within the PBG [88]–[92] and below dielectric band (cyan line). Two modes inside PBG have even (red line) and odd (dark blue) electrical field distribution. The fundamental mode (with lower frequency) is can be excited by an incoming plane wave. Others modes are usually loss and difficult to couple to.

In PhC waveguides, the group velocity of an optical pulse, expressed as $v_g = c/n_g$ is reduced and group index n_g is increased accordingly. The group index is plotted in figure 2.8 (b) at the three marked points in the dispersion diagram for fast (1), moderate (2) and slow light (3), whose field distribution is shown below, respectively. Approaching the band edge of Brillouin zone $k = \pi/a$, group index becomes large (n_g >100), but the group propagation losses increase at the same time. As seen, the mode profile alters within the propagation in the Brillouin zone. In fast light regime, the mode is confined inside the waveguide region, while in slow light regime, the mode extend into the holes. Consequently slow light modes are very sensitive to the exact positions of the holes and to fabrication disorder.

2.4.1 Slow light and PhC nanolasers

Slow light is a very interesting effect, which enhances light-matter interaction and improves device functionality [93]. Using slow light, the device size can be scaled down meanwhile improved gain, optical absorption and nonlinear effects per unit length can be demonstrated [94]. The main constraining factor, though, is fabrication induced structural disorder and imperfections, which result in the reduction of group refraction index and the increase of propagation losses [95]–[97]. Even local cavity may develop near the band edge manifesting in random lasing [98]. Consequently the design and experimental investigations in PhC must always consider these effects (loss and multiple scattering) in order to avoid any misinterpretation of the results, for example mistaking random lasing peaks for slow light enhanced gain.

Active photonic nanodevices draw an ever increasing focus [29], [99]. Including an active medium into periodic structure leads to enhancement of the effective gain, which is proportional to group index. Especially, as it was reported for one-dimensional photonic band gap made by a stack of dielectric layer of different thicknesses, effective gain is boosted by photonic band edge effect [100], which can significantly low the laser threshold. The modal gain coefficient can be expressed as:

$$g_{mod} = \Gamma g_{mat} = \Gamma \frac{n_g}{n_b} g_0 \tag{2.21}$$

where g_{mat} is the material gain, g_0 is the bare material gain in absence of a PhC waveguide, n_g is the group index, n_b is the dielectric refractive index of the active material, and Γ is a confinement factor describing the field overlap with the active material. Slow down factor is defined as:

$$S(\omega) = \frac{n_g^{PhC}}{n_g} \tag{2.22}$$

where n_g^{PhC} is the group index including the effect of the PhC dispersion. Owing to its impact on the light confinement, the slow down factor S affects also the amplified spontaneous emission (ASE) in the way that higher group index leads to longer interaction with matter [101]. However, as reported by Grgic et al. [102], the gain in the periodic medium is enhanced in a complex manner and the simple slow-light enhancement rule (2.21) does not hold anymore for large group index. In presence of an active medium, the dispersion hence the group index is modified and the total slow-light enhancement of the gain is capped. As demonstrated for active PhC waveguides, slow light not only enhances the gain, but also allows to control its spectral position by alteration of PhC parameters [99]. Another feature occurring near the band edge is loss increase, thereby it is better to use the net gain, which is defined as the modal gain minus waveguide losses ($g_{net} = g_{mod} - \alpha_{loss}$).

Photonic crystal lasers can be realized in a size as small as a cubic wavelength [103]. However, due to their small size, such lasers have a very low total output power. On the contrary laser lengths in the range of several tens of micrometers is considered to achieve output power levels in the range of tens of μW to 1 mW, and bandwidths in the order of several tens of GHz. Moreover, properties of long PhC cavities are close to their conventional counterparts, therefore, the same equations can be applied to describe the PhC lasers; and their dynamics would be easier to understand. In conventional lasers, lasing occurs when gain overcomes losses, which originate from partial transmittance of mirrors.

Adding a hole inside a W1 waveguide creates a mirror with reflectivity r_i, insertion of holes from both sides allow to realize a cavity [104]. The advantage of such cavity is that the net gain and waveguide's end facet reflection can be tuned independently. This is not possible in a single mode ultra-small PhC cavity. Long PhC cavities would allow, at a large stage, the inclusion of both gain and loss material, such as a saturable absorber, in the same cavity [105]. The combination of gain with a power independent feedback (saturable absorber) is indeed the key for the fabrication of high-repetition rate pulses lasers.

The guided mode in the PhC cavity hits one mirror and is backreflected to the second mirror, then backrefrected back on the first mirror. Thus, the important parameter of cavity is the modal reflection coefficient $r = |r| \exp(i\phi)$. Assuming loss-free roundtrip the phase matching conditions at resonance are

$$K(\lambda) = \frac{\pi m - \phi}{L} \text{ with } m \in \mathbb{N} \tag{2.23}$$

The slow-down factor changes the modes spacing since the cavity length effectively becomes longer. Hence the mode spacing is:

$$\Delta\lambda = \frac{\lambda^2}{2Ln_g} \tag{2.24}$$

Because the slow down factor varies strongly close to the band gap, the selection of lasing modes and the mode compression depends strongly on S. The threshold condition is expressed by:

$$\Gamma g_{mat} = \frac{\alpha_i}{S} + \frac{1}{2SL} Ln\left(\frac{1}{R_1 R_2}\right) = \frac{\alpha_i + \alpha_m}{S} \tag{2.25}$$

where α_i the is internal loss, L is the cavity length, $R_i = |r_i|^2$, α_m is the effective mirror losses. As seen, the slow light in this model affects the threshold limit by decreasing the impact of the mirror losses. One should keep in mind that the propagation loss α_i actually depends on the group index, hence α_i/S does not necessarily decreases with increasing group index.

This simple model gives a fair insight, which is sufficient for the first design and experimental investigations. Developing a more comprehensive theoretical model for PhC slabs with active material is a highly complex task because it requires, among others, including the electromagnetic field distribution and propagation in the slab along with coupling to the carriers in the quantum well. This coupling is not trivial due to dispersion of PhCs: slow light enhances the effective interaction length and the optical density of states [106].

Finally, an inverted taper (see figure 2.9) has been placed at the end of PhC in order to improve out and in-coupling [107], [108]. Additionally, tapers help suppressing the Fabry-Perot reflections, which are induced by reflection at the cleaved facet. Such features are critical because a reflection can play a detrimental role by interfering with the cavity end-facet reflection.

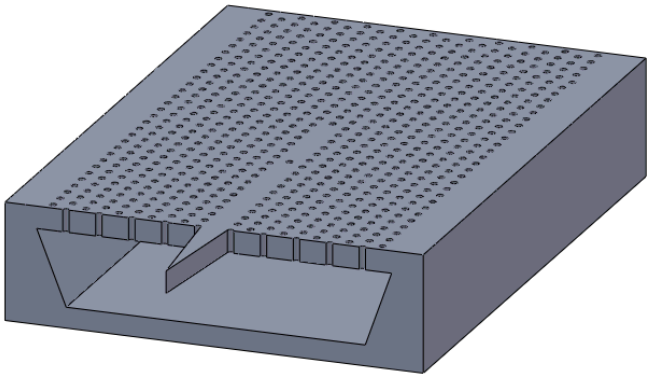

Figure 2.9: An illustration of a laser design with a taper and one hole out-coupling mirror

2.5 Summary

In this chapter, the overall physical processes in the MOVPE reactor are presented. The flows inside the chamber are described briefly. When working with III-V compounds, an important aspect is that growth occurs with great excess of the V group species. Assuming the incorporation rate of the III group to be the unity, growth rate of ternary compounds is determined by the partial pressure of equivalent constituent of the III group. Furthermore, the ratio between the growth rates of the III group and total growth rates defines the composition. Depending on the growth temperature, three regimes are allocated and are called kinetically limited, diffusion limited and the regime of high temperature where desorption prevails.

This work is centered around the development of selective area growth approach with further integration into a photonic crystal platform. Thus, the connection between grown layers and optical properties is established. Alloy composition of ternary compounds manipulates the emitting wavelength, lattice constant and, in addition, refractive index. The basic optical properties of heterostructures are described with an emphasis on the density of states.

During selective area growth, the presence of a mask perturbs the growth process manifesting in excess thickness and composition deviation. Working with InGaAs, thicker layers leads to a red-shift of wavelength as does the increased In content. For non-planar growth, also, various incorporation rates of Ga species on different crystallographic planes should be included in device design.

Photonic crystal slabs prohibit the light propagation at certain frequencies. Slow light effect in PhC enhances light-matter interaction and at the same time allows minimizing the device size. Including an active medium into a periodic structure results into increase of the effective gain, which is proportional to group index. Limiting the active area to the PhC part, where gain is required, allows reducing the pumping area and improving thermal properties of the device.

"A theory is something nobody believes, except the person who made it.
An experiment is something everybody believes, except the person who made it"

Albert Einstein

Chapter 3. Fabrication process

Novel ultra-compact photonic crystal (PhC) cavity lasers with the lowest power consumption [26], [27] can be fabricated employing the selective area growth (SAG) approach. In this chapter, development of the SAG method is presented. The fabrication was carried out at DTU DANCHIP cleanroom facility. The first section describes the optimization of an HSQ mask to produce material of high quality and with desirable optical properties. Subsequently, the surface preparation, which is an essential step for obtaining a strong PL signal, is set out in the second section. Investigation of MOVPE selective area etching and growth is presented in the third and fourth sections respectively.

3.1 HSQ mask

Hydrogen silsesquioxane (HSQ) is a promising masking material for nanoengineering application, especially for selective nano-scale area growth. Due to its high thermal resistance, it is compatible with high-temperature MOVPE processes [58]. HSQ is an inorganic high-resolution negative tone electron beam resist; in consequence precise control of the SAG pattern position can be achieved by means of electron beam lithography. The conversion of this resist into amorphous silica after exposure helps avoid critical fabrication steps such as glass deposition and mask transfer by reactive ion etching (RIE), which is essential as in the case of ZEP resist use and may introduce defects in further epitaxial growth.

In 1998 HSQ was used as an e-beam resist for the first time by Namatsu et al [109]. The ideal solution has a cage structure with formula $(HSiO_{3/2})_8$, which opens up during e-beam exposure. A network structure forms through cutting of the SiH bonds, which are weaker than SiO bonds. Then, cross-linking of siloxane (Si-O-Si) bonds are formed via unstable silanol (Si-OH) groups [110]. In addition, diffusion of exposed radicals into the matrix was reported [111] producing random cross-linking of a neighboring area leading to unreproducible results. The properties of the final film depend on spinning, exposure and development parameters and, pattern density.

3.1.1 Optimization of resist deposition conditions

At the beginning of this project, not much work had been done at DTU related to the HSQ resist named XR-1451, thus, a starting point was to obtain as thin a resist as possible. Thinner resist is preferable for use allowing reduced forward scattering that causes a broader beam profile at the bottom than at the top of a resist layer. Conversely, a mask may need to have a certain thickness

in order to withstand possible etching processes. The resin solution employed in this work is a spin-on material commercially available from Dow Corning Corporation. The resist is very sensitive to contamination; any particles in the spin-coated film can damage the performance of the fabricated structures. On this ground, a new bottle was poured into several single-use plastic bottles, which were stored in a freezer at -5°C to avoid fast deterioration of the material. Before pouring resist directly on a wafer, the bottles were thawed at room temperature for 30 minutes to prevent moisture condensation. By varying the angular speed of spinning or/and dilution rate using methyl isobutyl ketone (MIBK), the HSQ film can be spun on in various thicknesses from 13 nm up to 1.3 μm [112]. Dilution percentage and spinning conditions, carryed out in this work are presented in Appendix A. The thinnest film obtained was 13 nm.

After spin coating, hot plate baking is important in order to enhance the adhesion between HSQ and InP substrates, which is definetely worse than between HSQ and silicon. The pre-baking consisted of two steps: first at 120°C for 2 min, then at 220°C for 2 min. In spite of adhesion improvement, baking starts the cross-linking process in the HSQ layer, like the electron beam irradiation does, having a countering effect that leads to a reduction in resist contrast. It was reported [113] that even 8 h time delay between spinning and exposure increases the feature size of HSQ structures, no matter if the samples were stored in air, nitrogen or vacuum atmospheres. Keeping this in mind, the waiting time of HSQ covered wafers before the ebeam exposure was minimized. Several experiments with a delay time up to 3 hours in air atmosphere have not shown a noticeable increase in feature sizes.

3.1.2 Mask design for different quantum structures

By altering the mask design, engineering of structures with quantum confinement is realized. A written pattern remains on a wafer after development, since HSQ is a negative tone e-beam resist. Semiconductor parts protected by resist stay passive providing selectivity during epitaxial deposition.

To fabricate, for instance, selective area QWs, a single pattern feature consists of a pair of rectangular masked regions with a narrow gap (opening), where a QW is grown (figure 3.1 (a)). Scaling down the opening size to the exciton Bohr radius (11.3 nm in InP [114]) allows obtaining QWires. Reducing dimensions even further by creation of intersecting lines (grating) depicted in figure 3.1 (b) or alternatively, squares/circles with square-/circle-shaped openings (figure 3.1 (c)) may be used for fabrication of structures with 0D confinement (QDs). Comparing them to commonly used Stranski-Krastanov (SK) growth mode, the investigated technology allows achieving them in a selected place with high homogeneity in size and shape. In this study, two rectangular lines with nano-scale openings between them, a square with a nano-scale square-shaped opening inside, and a 2D grating were the main patterns investigated. In conjunction with spinning process and mask design optimization, exposure and development are crucial steps in having a feasible mask for SAG; therefore, investigation of these parameters are presented in the next section.

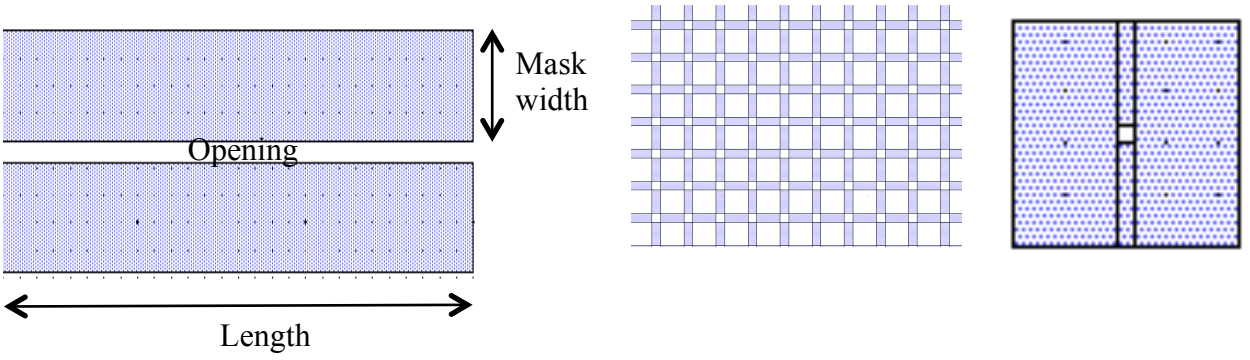

(a) (b) (c)

Figure 3.1: Pattern features for SAG of a QW (a), an array of QDs (b), and a single QD (c)

3.1.3 Optimization of exposure and development conditions

The optimization process started from exposure of 13 nm thick XR-1451 resist spun on an InP wafer (see section 3.1.1). At the beginning of the project, ebeam exposures were performed in a JEOL JBX-9300FS e-beam writer, which was replaced by a new one (JEOL JBX-9500FS) both operated at 100kV. To determine an optimum dose, the electron doses were varied in a series of steps (1000, 3000, 5000, 7000 μC/cm^2). The e-beam writer was driven at 10 nA current. After exposure, resist was developed in 1 AZ400K : 3 H_2O (potassium hydroxide (KOH)-based) for 2 minutes. In all experiments AZ400K solution was applied at room temperature. Each sample was developed immediately after e-beam writing, i.e. influence of the delay between exposure and development was negligible. The exposure resulted in only partial presence of the mask making the estimation of the optimum dose impossible.

Consequently, the next experiment was conducted on 50 nm thick resist and a dose range: 4000, 5000, 6000, 7000, 8000 μC/cm^2 - using the same current and development conditions as before. Two well-established techniques, such as scanning electron microscopy (SEM) and atomic force microscopy (AFM), were used to analyze the lithographic process. In particular, DTU Danchip cleanroom facility has got a SEM Zeiss Supra VP 40 SEM and a Dimension 3100 Nanoman AFM. Although, two widely used parameters to characterize resist are contrast and sensitivity, in experiments described below, the absence of a residual layer and the full presence of the pattern, as well as HSQ exposed and open area sizes, were the main evaluation criteria. As a matter of fact, residue renders dramatic impact, such as a drastic reduction of PL, on the quality of the fabricated devices. Figure 3.2 presents a InGaAs/InP QW, for which the PL signal was not resolved, grown in the open gap containing dense HSQ leftovers. The distribution of the residual layer among samples has haphazard character as occurred. There is a trade-off between reducing scum and improving adhesion because a higher dose guarantees more stable pattern, but it gives more condensed residue. Taking into account the possibility of washing the pattern away like during the first exposure, the optimum dose was set 6000 μC/cm^2. Considering the feature dimensions, noteworthy to say that granularity of HSQ resist causes a big fluctuation in the line width measurements. However, component sizes can be adjusted by the mask design.

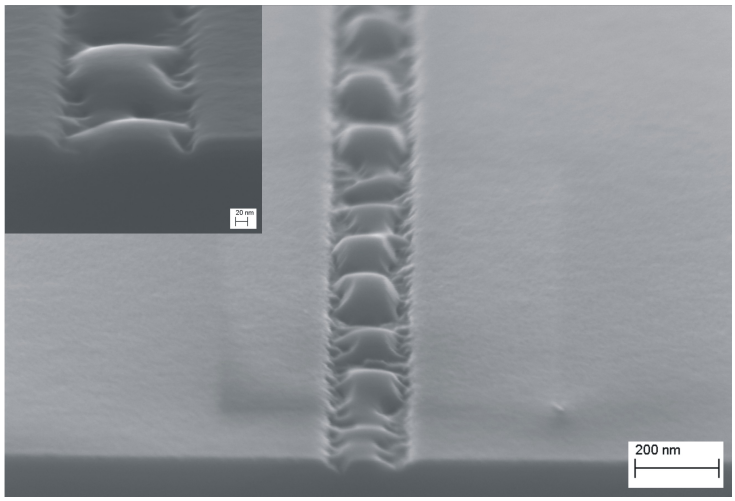

Figure 3.2: SEM image of a SAG QW grown in the opening with a dense residual layer (the exposure dose was 8000 μC/cm^2)

In order to succeed in dealing with a tremendous residual layer issue, another type of developer was investigated. Apart from AZ400K, tetremethylammonium hydroxide (TMAH) aqueous solution, named MF CD-26, can be used as a developer to dissolve the cage structure over the network one. AZ400K is almost five times stronger than MF CD-26 because siloxane bonds are broken slower in TMAH. KOH-based developer gives higher resist contrast [115] compared to TMAH; but in contrast, TMAH one has a higher sensitivity allowing the use of a lower exposure dose. This results in a smaller amount of insoluble residues in the unexposed areas and in a shorter writing time. Accordingly, the dose range was chosen 800, 900, 1000, 1200 and 1500 μC/cm^2 for the same mask design. Prior to development, the InP wafer was cleaved into four quarters to apply different time (75 s, 50 s, 25 s, and 15 s). The quarters were developed in MF CD-26 at a temperature of 50 °C. Even the parts written with the maximum dose of 1500 μC/cm^2 were washed away. After few attempts emerging washing of the mask away (even when thicker resist of 30 nm was used), it was decided to not employ TMAH developer, and to use the KOH one.

An alternative solution to the inevitable scum problem could be removing it in diluted hydrofluoric acid. After development, the samples were dipped in a 5% HF:H_2O (5% HF diluted further 1:100 by volume) solution for 90 s. The longest etching time done was 90 s for well-exposed protection lines without losing parts of them. A serious drawback of this approach is the opening enlargement or even total pattern removal due to etching of HSQ by HF. The width of the opening before and after HF treatment was measured by AFM and data are presented in table 3.1. The obtained data show that HSQ etching rate in 0.0049% HF is approximately 1.2 nm/s. On one hand, this approach gave the expected result in removing the scum, on the other hand, this process is not well controlled, for example, small features can be easily lost due to poor adhesion of HSQ. Thus the question of scum removal still remains open.

Table 3.1 Opening and protection line sizes before and after etching in diluted HF acid

	Opening size, nm	Opening size, nm	Protection line, μm
Before etching	162 nm	248 nm	4.322 μm
After etching	282 nm	363 nm	4.098 μm

Another method of surface cleaning from the residue was inductive coupled plasma reactive ion etching (ICP- RIE). The used process contains the mixture of carbon tetrafluoride and hydrogen (CF_4:H_2) gasses in a ration of 10:10 sccm where the pressure was 3 mTorr[2]. This recipe gives slow etch rate of glass (8 nm/min) making it convenient to work with resist thinner than 50 nm. After etching, the sample was investigated by AFM using a special cantilever SSS-NCHR, which has a tip radius <2 nm for improved resolution of roughness. The roughness can be expressed in terms of the root mean square:

$$R_q = \sqrt{\frac{\sum(\mathrm{Z_i})^2}{\mathrm{N}}} \qquad 3.1$$

where Z_i is the current Z value, and N is the number of points within the box cursor. Figure 3.3 (a) shows damaged InP surface after etching. The measured value was R_q=0.8 nm on an area of 70 nm×70 nm. Comparison of this value to the original InP epitaxially growth surface, which is R_q=0.1 nm measured on the same area, proves the rough surface. Moreover, the HSQ mask had rough edges preventing clear observation of the opening area (figure 3.3 (b)). On the basis of the AFM measurements, this etching method is not appropriate to surface cleaning without further optimization.

[2] The used process was optimized by Irina Kulkova for glass etching using in another SAG technology

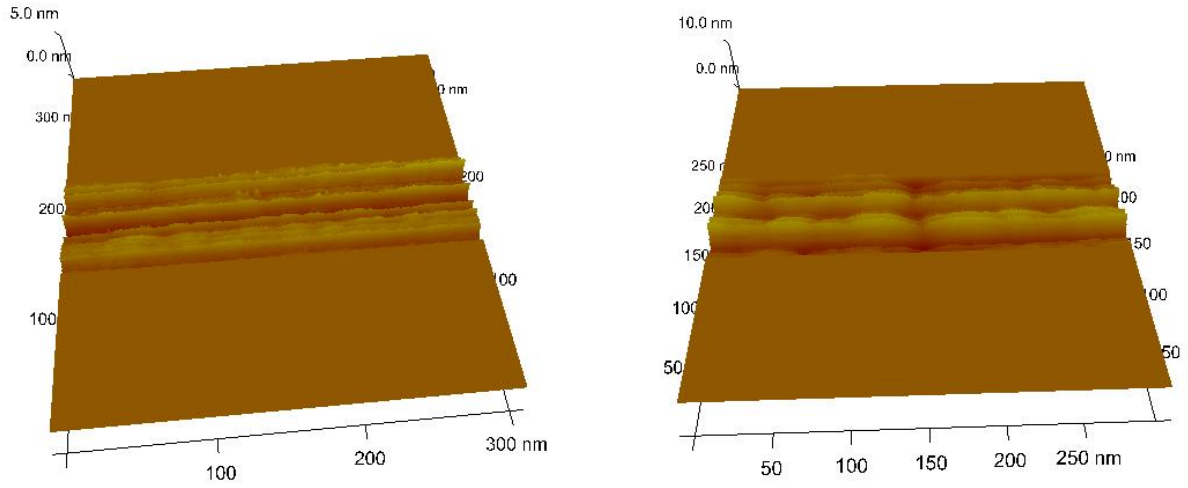

(a) (b)

Figure 3.3: AFM images of the InP surface 5 µm away from the mask (a) and the mask with 50 nm opening, which is not well defined (b), after ICP-RIE

The experiments with thin resist of 13 nm revealed either partial/complete absence of the pattern or dense openings when the applied dose was increased. The further examination was done using XR-1451 film thickness of 30 nm (see section 3.1.1). The applied dose was varied in a series of steps (2000, 3000, 3500, 4000, and 5000 µC/cm^2). The beam current was raised from 10 nA to 30 nA, which reduces the fabrication cost via shorting the writing time. Such changes did not affect the feature dimensions. The core of this experiment was investigation of different development conditions to improve the mask performance, such as removing the residual layer and increasing the HSQ adhesion. In order to collect more data, the whole wafer was cleaved into four quarters at which four different development conditions were applied. The previously used developer of 1 AZ400K: 3 H_2O was applied to the first sample. Another option was the more concentrated 1 AZ400K: 2 H_2O in order to clean the residue from the surface, which, as was mentioned above, has a huge impact on the optical quality of fabricated structures. More aggressive developers attack the resist strongly raising the adhesion problem. However, adhesion of HSQ can be promoted by post-apply-bake [116], thus baking at a temperature of 90 °C for 5 minutes after exposure was combined with the common used here developer. The post-apply-bake helps to dissociate the SiH bonds and form network structure where new SiO bonds are created. The amount of SiO bonds are affected by time and temperature [117]. The fourth investigated parameter was baking after development in 1 AZ400K: 3 H_2O to check if this step can improve the etching resistance of HSQ during further processing (in particular, fabrication of alignment marks for PhC devices which is outlined in the section 4.2).

To investigate a pattern for SAG QWs (see section 3.1.2), protection line widths of 0.1, 0.5, 1, 2, 3, 4, 5 µm and opening sizes of 10, 25, 50, 75, and 100 nm were chosen. A couple of points were similar for all development types: first, the smallest opening size was detected. In particular, opening sizes smaller than 10 nm were not developed; 25 nm openings had dense connected residue as shown in figure 3.4 (a). Therefore, the smallest achieved open area was

50 nm. Secondly, with widening of the protection lines, the quantity of scum increases. Thirdly, the structures exposed with the dose of 2000 μC/cm^2 were overdeveloped thus the exposed features were not homogeneous, as shown in figure 3.4 (b). Deposition of material in the unclosed parts of the mask would reduce the selectivity in the following epitaxial process. On the other side of the dose range, the dose of 5000 μC/cm^2 was too high which resulted in more pronounced residue when compared to other doses or undeveloped openings with 5 μm lines.

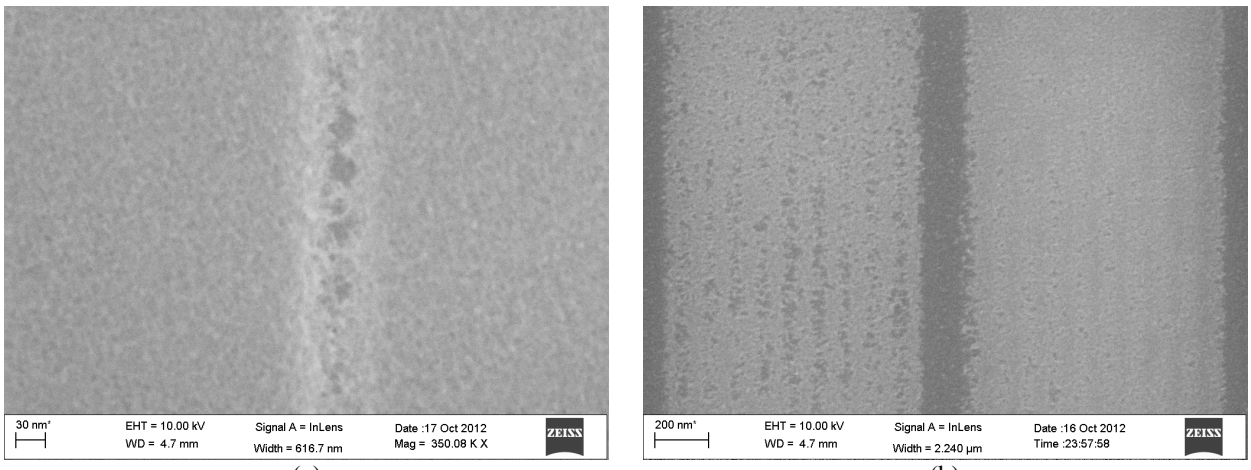

(a) (b)

Figure 3.4: SEM images of dense residue in an opening area (a) and underexposed HSQ lines

When working with 30 nm thin resist, it was noticed that the width of the protection lines had stronger influence than the applied developer conditions over the presence of the residual layer. Considering 1 AZ400K: 3 H_2O developer, the optimum dose laid in a range of 3000-3500 μC/cm^2. Thus for 3000 μC/cm^2, the 50 nm design openings became wider by 20 nm. And the 50 nm openings exposed with the dose of 3500 and 4000 μC/cm^2 had a dense scum; therefore, the smallest residue-free opening was 75 nm. The concentrated developer (1 AZ400K: 2 H_2O) revealed the optimum dose of 4000 μC/cm^2. A smallest clean opening of 50 nm was obtained; however, for the widest protection lines, openings of this size had connected parts of scum.

Next, baking after exposure did not show expected adhesion enhancement. For example, structures exposed with 2000 μC/cm^2 still had unfastened parts (see figure 3.4 (b)) within smaller density though. The 3000 μC/cm^2 dose was too high and the scum was more pronounced including higher doses. Under no circumstance has there been any evidence of adhesion improvement. To draw a conclusion, the optimal conditions for exposure and development were the base dose of 4000 μC/cm^2 and the developer concentration of 1 AZ400K: 2 H_2O for 90 s without post-apply-baking.

Finally, adding thermal curing after development, surprisingly, diminishes adhesion. Notably, the structures exposed with a dose of 3000 μC/cm^2 were overdeveloped. For 3500 μC/cm^2 and 4000 μC/cm^2 doses, the amount of residue was smaller compared to the already described conditions, at the same time the openings were overdeveloped. As can in figure 3.5 (a), the

thickness of remaining resist is thinner compared to other cases indicating worse adhesion. Indeed, no improvement in the etching resistance was observed, so these development conditions are not applied for the fabrication of alignment marks.

Roughness of the HSQ film, described in terms of R_q, is given in figure 3.5 (b). Markedly, the surface roughness is affected by post thermal treatment. The formed after baking network structure seems smoother than the cage one.

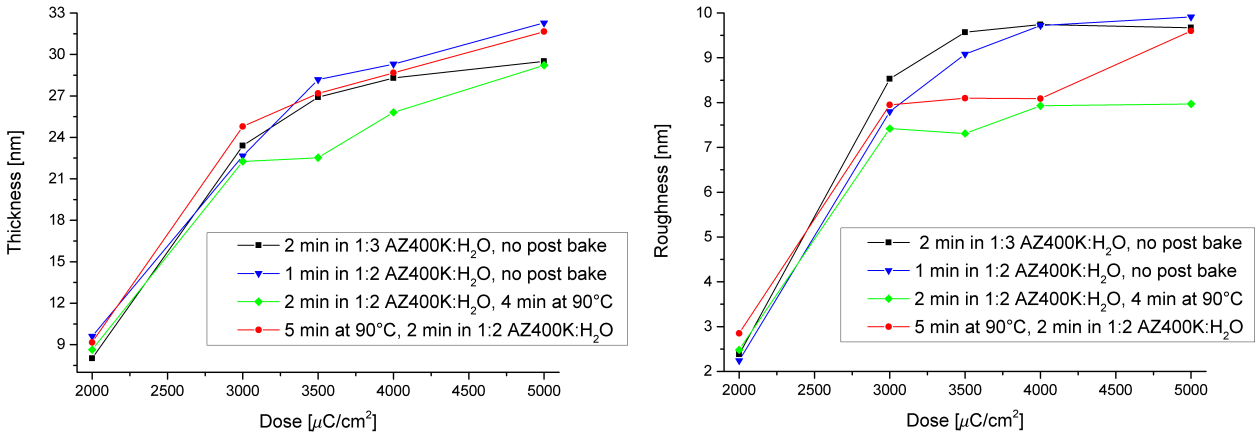

(a) (b)

Figure 3.5: Thickness dependence (a) and roughness (b) vs applied doses of 30 nm thick HSQ layer using four different development conditions.

Adding the proximity correction to the pattern preparation helps keeping the opening sizes independent on the mask geometry. The proximity effect is caused by forward and backward scattering which results in widening feature sizes. To solve this problem, the point spread function (PSF) (the energy distribution of the scattered electrons) can be added to the coding of the pattern in electron beam software called "Layout Beamer". Using another software "Sceleton", the PSF itself can be calculated by a Monter Carlo method. In time of pattern preparation for exposure, extra parameters such as bias and beam blur can also be adjusted[3] to reach more accurate outcome.

Now turning to the pattern for fabrication of quantum dots, which are the structures of interest due to their potential superior properties. A single feature contains a square-shaped opening in the square protection matrix (see section 3.1.2). After exposure and development, the square shape of openings became circles. In general, this pattern follows the same behavior for development as structures for fabrication of QWs, except that openings became smaller in diameter when the protection square increases in size. A similar trend was seen in the amount of residue: for underdeveloped structures, the opening sizes were smaller than designed with less pronounced scum. To fabricate an array of identical QDs, the mask performs as intersection lines wherein a width of a single line is 40 nm and opening sizes in a range of 15-40 nm (figure 3.6). None of applied development conditions succeeded in achieving this pattern. It requires careful

[3] The parameters were obtained from the dose correction done by Luisa Ottaviano

writing involving minimizing the aperture in the e-beam writer. In such a way, the electron spot size is reduced enhancing the resolution. A slow writing process (low applied current) can also guarantee complete writing of all intricate details without the loss of pattern integrity. Due to time limitation the further optimization of this pattern is beyond the scope of this work.

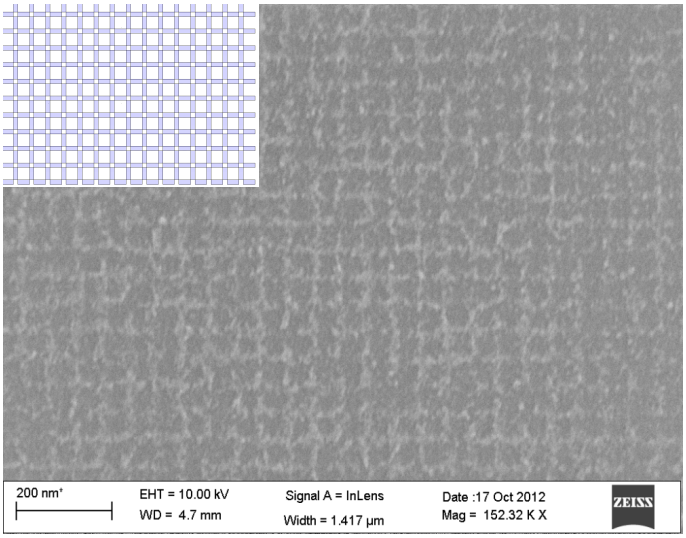

Figure 3.6: SEM image of the exposed pattern for an array of QDs. Inset shows the mask layout.

One point is worth noticing is that HSQ possesses an aging effect which is steady polymerization leading to the increase of molecular size distribution [118]. The manufacturer's recommended shelf life time is about 6 months, but HSQ can be used after expiration date for about a year. However, aging time decays the contrast and reduces the onset dose. Thus, even when all parameters are optimized to obtain the best performance of the final devices aging HSQ may require adjustments in the parameters.

3.2 Surface preparation for epitaxial growth

Combining ex situ patterning with epitaxial growth calls for surface preparation before nano-selective area growth. Before loading samples to the MOVPE reactor, organic contamination was removed in a parallel plate oxygen asher at 0.2 mbar pressure. This followed by etching of native oxide in concentrated sulfuric acid for 2 minutes, then rinsing in the water chamber with bubbles for 5 min. Sun et al. [119] claimed that complete removal of the native oxide from InP requires a strong acid solution at high concentration. The concentration of H^+ needs to be high enough to prevent OH^- group bonding to the surface, which makes it hydrophilic and oxidizes InP. During hydrolysis, hydrogen atoms attach to phosphorus atoms providing hydrogen termination leading to a hydrophobic surface. The hydrophobic surface is resistance to oxidation from water and to carbon contamination from the acid. Such a solution for surface preparation might be sulfuric acid, which does not, significantly, etch InP.

Importantly, Ebert et al. [120] determined that concentrated sulfuric acid etches InP with etch rate around 5 nm/min. To check this statement, SEM and AFM measurements of a sample with a

selective mask oriented along [0-1-1] and [0-11] directions were carried out. Not only etching at 7 nm/min etch rate was observed, but also crystallographic dependent behavior. In case of the mask oriented along [0-1-1] the etched groove profile is illustrated in figure 3.7 (a) wherein revealed (11-2)B and (1-12)B planes forming an angle 65 degree with a (100) plane. In another [0-11] direction, there are (2-1-1)A and (211)A planes constructing an angle of 35 degree to a (100) plane.

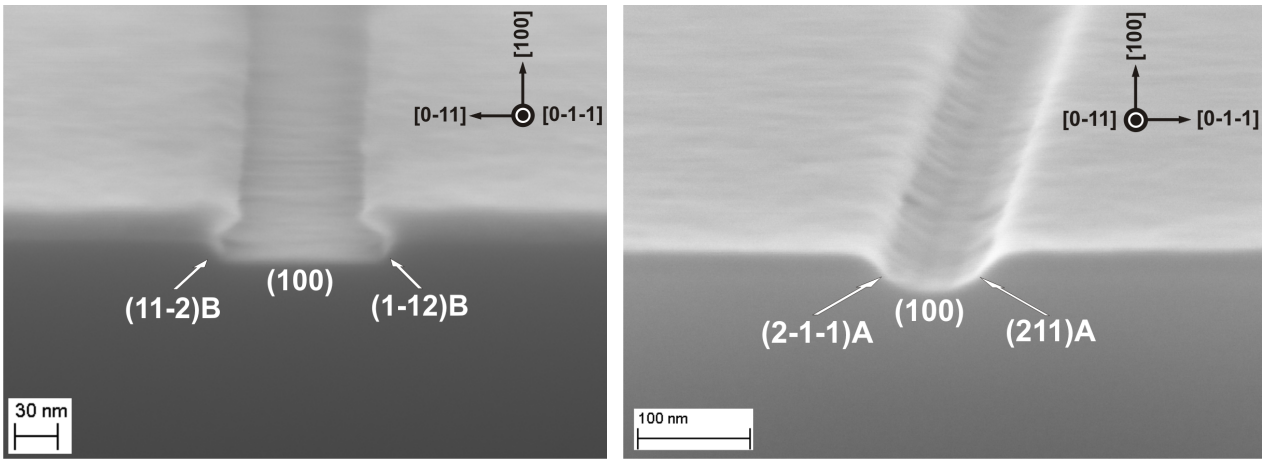

a b

Figure 3.7: SEM images of a sample with the HSQ mask on the top directed along [0-1-1] (a) and [0-11] (b) etched 2 minutes in 98% H_2SO_4. The width is 1 μm and opening size is 75 nm

Even 14 nm etching depth evolving different crystallographic planes can significantly affect characteristics of nanoscale area growth. So to minimize the influence of surface preparation, experiments employing different etch time (30 s, 1 minutes and 2 minutes) were conducted. Then inside the MOVPE reactor, CBr4 etching and overgrowth of 4 nm InGaAs/ 10 nm InP layers, which are described in the following sections in more details, were done. Based on PL measurements of grown structures and compared to the unpatterned area 1 mm away, it was evaluated that 1 minute is the shortest time having no impact on optical signal. An open bath sulfuric acid absorbs water molecules from air lowering its concentration. As a result, diluted H_2SO_4 does not etch InP even on a nanometer scale, but can leave random residue that is pernicious for further epitaxy.

In an attempt to improve the surface preparation, ammonium hydroxide (NH_4OH) etching [121] was added to this step. Two samples were prepared for the experiment. The first one was etched in 1 NH_4OH: 5 H_2O for 30 s, and then the surface cleaning procedure of 1 minute in sulfuric acid and 5 minutes in the bubbles chamber was applied. On the second sample only latter surface cleaning procedure was employed. No difference in the Pl intensity of a single InGaAs/InP QW was observed for the two compared samples; therefore, the additional step of NH_4OH was not utilized in the current study.

After the ex situ surface treatment, the wafers were loaded immediately into the MOVPE reactor. Further thermal deoxidation for 15 min at 650 ºC under a phosphine flow. To clean the surface even more, in-situ etching of InP that is taken up in the section below.

3.3 In-situ etching of InP by CBr_4

In-situ etching of InP by carbon tetrabromide (CBr_4) reduces the amount of nonradiative recombination of investigated quantum heterostructures by improving the interface quality [122]. CBr_4 is a well-known precursor for doping of GaAs based materials due to weak bonds of C-Br. In comparison with carbon tetrachloride (CCl_4), which is another etchant of InP, bromine-containing materials are less corrosive, averting damage to equipment and the environment.

Before research into selective area etching, it is essential to verify CBr_4 parameters, such as temperature and flow, to obtain a specular surface for further overgrowth. The temperature values chosen were 610 °C, which is the typical growth temperature for an InP layer, and 700 °C. Two flows of CBr_4 bubbler were chosen 105 sccm and 116 sccm, based on the results of Ebert et al. [120], corresponding to molar rate of 10.1 and 11.1 μmoles/min respectively. The CBr_4 bubbler was maintained at 18 ºC temperature and etching was done at total pressure in the reactor of 60 Torr. To prevent phosphorus evaporation, etching was performed under a phosphine (PH_3) flow of 200 sccm.

Using the emissivity-corrected pyrometer on the reactor, monitoring of the etching process was realised. Optical reflectance plot depicted in figure 3.8 illuminates initial growth on an epi-ready (001) InP wafer followed by CBr_4 etching. The first 1000 s is the procedure start including heating up a wafer, succeptor rotation to 1000 rpm, and thermal deoxidation. Then, 300 nm of InP buffer layer was grown corresponding to 1600 s on the optical reflection plot. Next, 100 nm of $In_{0.53}Ga_{0.46}As$ was deposited having large difference in refractive indexes to InP allowing subsequent monitoring in line of the etching process. On the top of InGaAs, 850 nm of InP was grown that was etched under conditions presented in table 3.2.

Table 3.2 Etching temperatures and flows

Region #	Temperature, °C	Flow, sccm
1	610	105
2	610	116
3	700	105
4	700	116

Each step was done for 600 s except for the region 4 where the etching time was 840 s. Etching rates, which are inversely proportional to an oscillation period, can be extracted from the optical reflectance curve. However, a non-uniform etching process and slow removing of byproducts from the interface (in particular, at a lower applied temperature T=610 °C) give a not sinusoidal curve that makes extraction of the etching rates complicated in the current experiment.

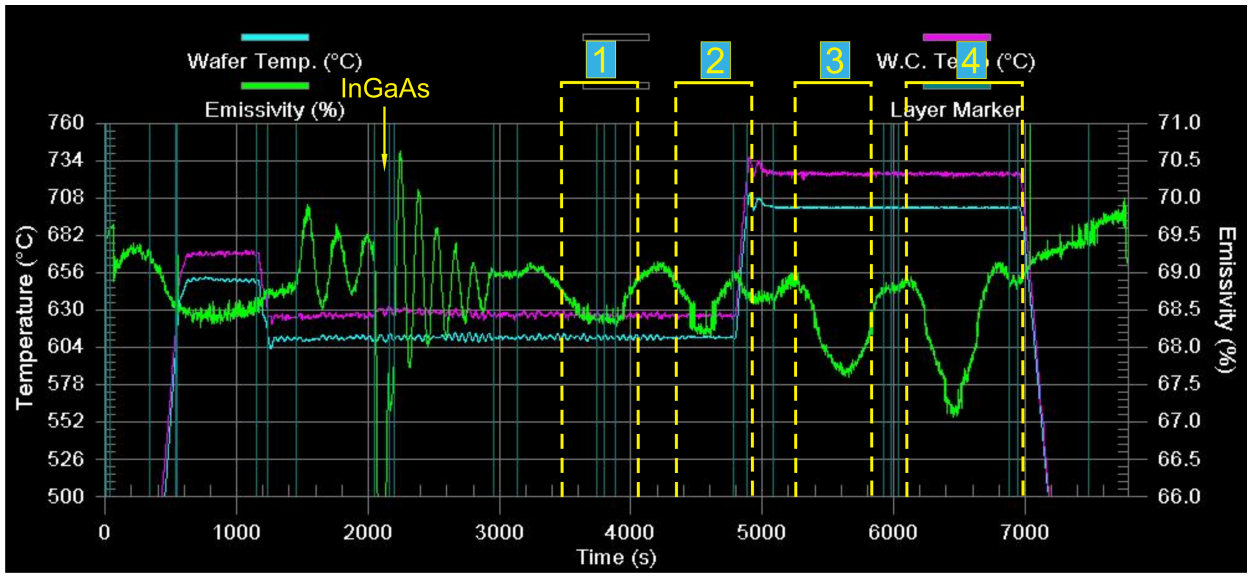

Figure 3.8: Optical reflectance (green plot) illustrating InP/InGaAs growth and in-situ CBr_4 etching. The red and blue plots indicate the wafer temperature

In analyzing the surface morphology subsequently, carried out AFM scans illustrated a rough surface with hillocks around 100 nm in height. Due to this, the experiment was repeated varying only one parameter. The optimum based on the AFM surface evaluation was found to be 610 ºC etching temperature and 116 sccm flow resulting in etch rate of approximately 10.5 nm/min. From time to time, the etch rate needs of recalibration as flows in reactor conditions change. To assess the etching quality, etched InP surface was examined and compared to the epitaxially grown one (figure 3.9 (a) and (b)). Comparison revealed the atomically smooth and specular surface as the original one.

A survey of other materials, in particular InGaAsP, showed a rough surface with hillocks around 10-20 nm in diameter (see figure 3.9 (c)). An explanation for such behavior can be obtained by adopting the view of Arakawa et al. [123]. During etching, decomposed Br radicals interact with In forming the In-Br volatile compound:

$$\text{III-V (solid)} + \text{Br} = 1/2V_2 \text{ (gas)} + \text{III-Br} \qquad 3.2$$

The formed compound is removed from the surface into gas phase along with thermal desorption of phosphorus from the surface. In the case of InGaAsP, Ga-Br compounds or/and As atoms do not effectively desorb leading to large amounts of residuals. Further to this, reviewing GaAs etching by CBr_4 [124], CBr_4 radicals decomposed into CBr_x radicals and Br^- interacting with H^+ to form HBr. Ga atoms cooperate with CBr_3 creating limiting volatile compounds of $Ga(CBr_3)$ and Ga-Br. Thereby, different volatility of materials affects their ability to be etched.

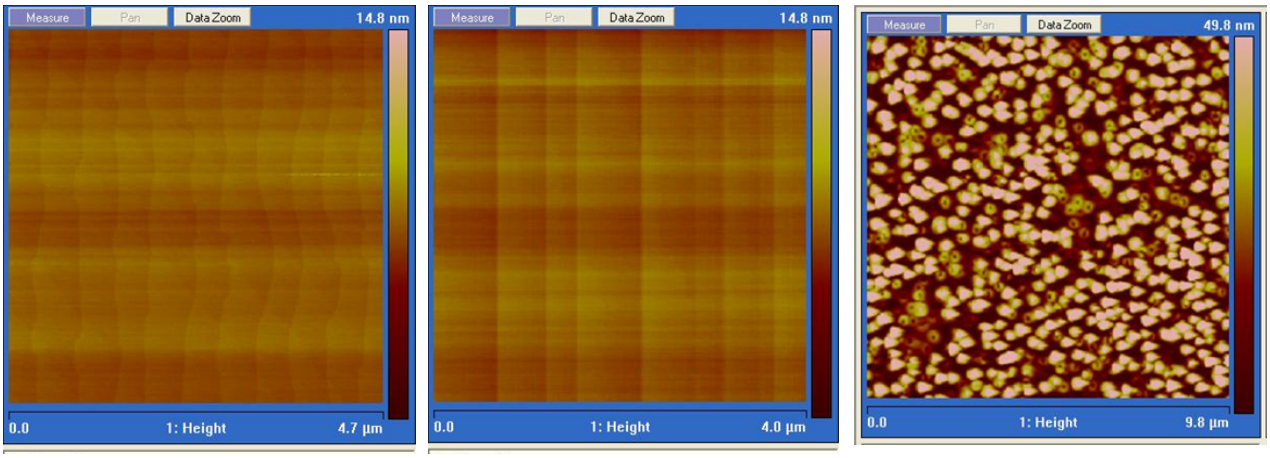

(a) (b) (c)

Figure 3.9: AFM images of epitaxially grown InP (a), InP after CBr_4 etching (b) and InGaAsP etching (c)

In order to remove all byproducts, growth interruption after CBr_4 etching, varying in steps (1 s, 20 s, 120 s), was implemented under PH_3 flow of 200 sccm. In order to verify suitable parameter, the same procedure as in case of surface preparation was applied to measure PL intensity of an overgrown single QW. The strongest intensity was obtained with 20 s growth interruption. It is worth mentioning that surface preparation assesses a larger impact on the PL signal intensity than growth interruption.

To investigate possible carbon doping during etching, secondary ion mass spectroscopy (SIMS) was done using an ATOMIKA SIMS[4]. Mass spectra and depth profiles were measured using two primary ion sources O^+ and Cs^+. In general, the signal is proportional to the total concentration without influence of impurities; however, the absence of implant standards for III-V materials made impossible to calibrate the carbon concentration. The sample for investigation was etched by CBr_4 and then InP/InGaAs/InP layers were grown. In figure 3.10 (a) and (b) the depth profiles are shown where the secondary mass ion signal of $^{12}C^-$ and $^{13}C^-$ were monitored. The high-level background originates from always-present gases in the SIMS chamber such as CO and CO_2. The obtained results showed that the formed QWs have a carbon peak monitored by Cs^+ source and carbon-free structures using O^+ one. Cs+ source is more sensitive for the detection of the electronegative elements such as carbon. Either O+ did not detect carbon or the carbon incorporation is not uniform on the wafer.

[4] Dr. Peixiong Shi provided most of SIMS measurements.

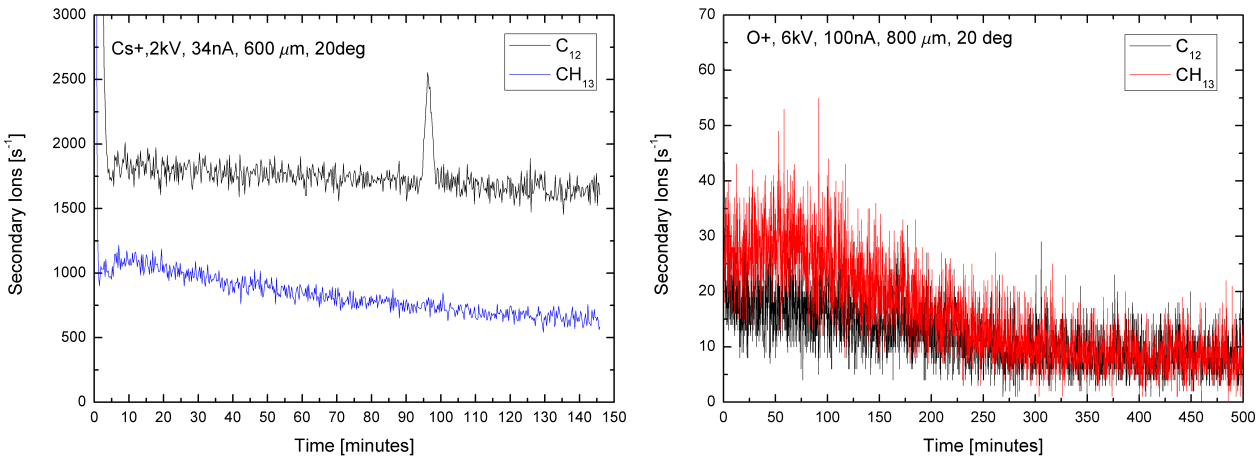

(a) (b)

Figure 3.10: Depth profiles taken using Cs^+(a) and O^+(b) sources

3.3.1 Selective area in-situ etching

Investigation of selective area in-situ etching is essential in device design to obtain reproducible and predictable results. Owing to the crystal structure of InP, patterning the wafer with a mask causes the etching to be limited by crystallographic planes.

In the current study, a single pattern feature consisted of a pair of rectangles masked by HSQ regions (see section 3.1.2) of 200 µm in length with a narrow gap where the active material was grown. The width of the masked region was varied in three discrete steps (1 µm, 4 µm, and 10 µm) and the gap between the lines was varied in a series of steps (nominally 50 nm, 75 nm, 100 nm, and 200 nm). The mask was oriented along major (0-1-1) or minor (0-11) flats (EJ convention wafers).

Owing to lack of tools for in-situ monitoring of selective processes on a nanometer scale, a developed criteria for evaluation of groove profile was postgrowth observation of InGaAs/InP layers (nominal thicknesses of 5 nm/10 nm respectively) simultaneously functioning as a growth marker. To increase the contrast of SEM images, grown layers were stain-etched in a 1 H_2SO_4: 8 H_2O_2: 80 H_2O solution. Thus, InGaAs appears as a dark region on SEM images.

During the first experiments, the etch time chosen was 183.5 s[5] which is equivalent to 30 nm etched depth on an unpatterned area. Along the [0-1-1] direction, figure 3.11 represents a trapezoidal-shaped trench combining {111} and {100} planes, to be more specific, the sidewalls are (1-11)B and (11-1)B planes (see section 2.3.1). Importantly, openings of different widths were terminated by the constant angle of 54 degree indicating the self-limiting nature of this type of etching.

[5] In selective etching, the mask parameters affect etching speed; therefore, etch time is used as a reference parameter not an etched depth

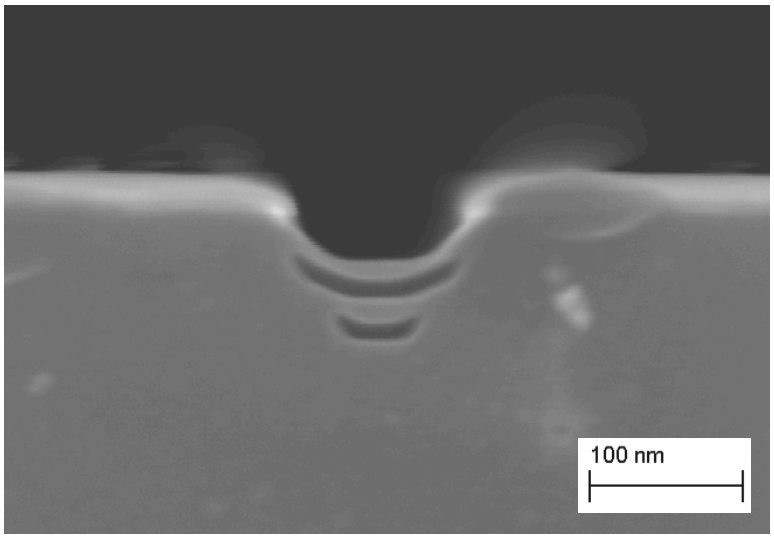

Figure 3.11: SEM cross-sectional views of a trapezoidal-shaped trench

In view of the above observations etching longer would end up in a triangular trench or a V-shaped pattern which offers a possibility to grow the challenging structures - quantum wires [71], [72]. The ex-situ wet or dry etched V-grooves demand that an InP buffer layer be grown before InGaAs to prevent reduction in optical properties. Due to the small volume filling factor [72], the additional layer of InP increases the effective size of InGaAs. Using etching inside of the MOVPE reactor, InGaAs material can be grown directly in etched trenches thereby maintaining a high optical signal. Furthermore, commonly when quantum wires are fabricated into V-shaped grooves, a thin QW is formed on the sidewalls, traps the carriers and funnels them into the QWire [30].

To verify this growth mode in our material system, the etch time was increased to 600 s resulted in a V-shaped groove along [0-1-1] and [0-11] directions (figure 3.12). Closer examination reveals presence of dense residue either from HSQ residual layer or poor surface cleaning. Etching behavior of this specific sample was completely different and the repeation of the experiment did not give the V-shaped grooves with 5 nm bottom plateu. Analysis of InP preparation ways, such as epitaxially grown or epi-ready wafers, flow dynamics in the reactor, effects of aging masking material has not revealed any data about non-repeatable results. Existence of the residual layer could locally change the etching properties whereby V-shape was observed only for few structures of the pattern layout.

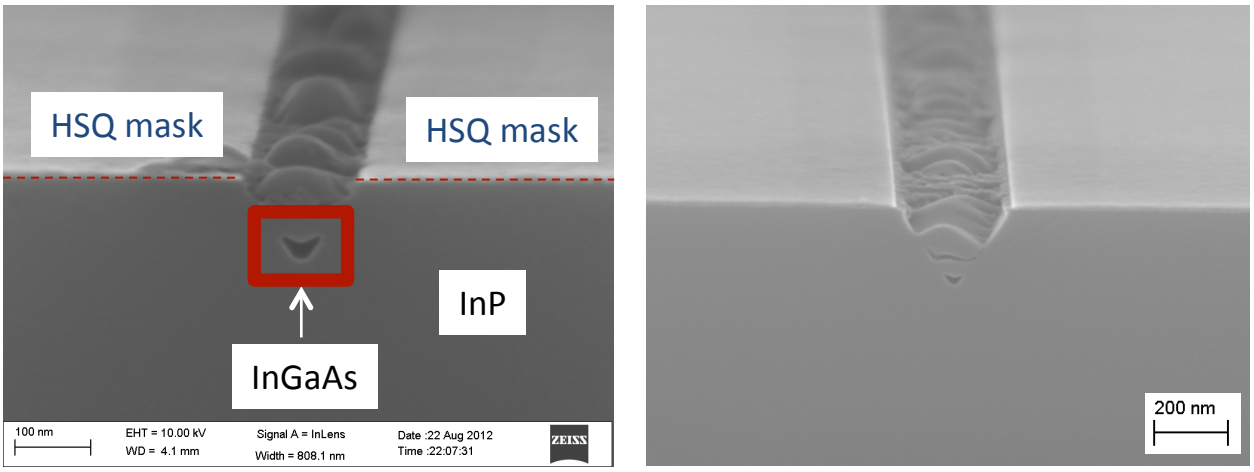

(a) (b)

Figure 3.12: V-shaped grooves after CBr_4 etching along [0-1-1] and [0-11] directions

Another set of experiments was done without growth markers. Along [0-1-1] direction the trench possesses anisotropic type of etching resulting in a U-shaped geometry (figure 3.13 (a)) which evolves three types of crystal planes: {111}B, {311}B and {100}. Contrary to other directions, etching along [0-11] remains to be more isotropic (figure 3.13 (b)) with developed crystal planes: {111}A, {311}A, and {100}. In both cases, the angles of the grooves are 54 degree that forms {111} planes with {100} planes, and 26 degree, that produces {311} planes with {100} planes. As seen, for example, in figure 3.13, there is an absence of re-deposited material on the mask or in the trenches signaling that all byproducts have been removed and good quality interface quality has been achieved for regrowth.

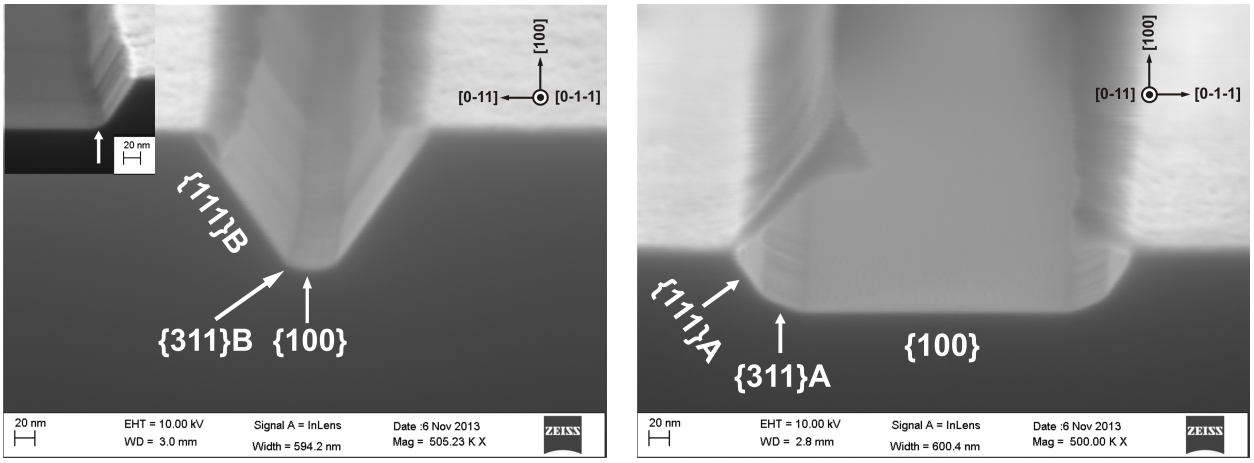

(a) (b)

Figure 3.13: SEM images of CBr_4 etch profiles along [0-1-1] (a) and [0-11] (b) directions. The designed opening size is 50 nm and the protection line width is 4 µm etched for 1000 s

To investigate the trenches' profile, the etching time was varied in three durations (300 s, 500 s, and 1000 s). Considering the structures oriented along the [0-1-1] direction, the etching is associated with the development of U-shaped grooves. When analyzing the shortest time of

300 s, the trench was seen to possess a trapezoidal shape with a combination of {100} and {311}B planes at the bottom. The etching time, in this case, was not enough to reach the self-limited V-shaped grooves. Although, it was challenging to clearly resolve the {311}B surfaces, their length could be estimated to be around 7-10 nm with no interplay of the mask parameters or etching time. Also, the etched depth, which is defined as the maximum depth in the groove, is not dependent on the opening sizes (see figure 3.14 solid lines). The variation in depth for 4 µm protection lines was measured to be 4 nm, which is similar to the measurements uncertainty. For comparison, the etch rate on an unpatterned area was approximately 10 nm/min, which was determined using optical reflectance produced by the emissivity corrected pyrometer.

Increasing the time to 500 s, or even 1000 s, registered slowing of etching for opening sizes smaller than 100 nm. Even though the grooves etched in the small openings achieved their self-limit, their bigger analogs can still be etched down vertically. Further evidence of the self-limit was that the smallest size of the bottom {100} planes attained its value of 15 nm at 500 s. For the longer time, the bottom plateau was not enlarged, while the undercutting increased indicating slow lateral etching after reaching the self-limit. In all experiments the etch rate was higher for a wider mask, as denoted in figure 3.14 (solid lines).

The etching along the [0-11] direction showed very different etching behavior with a dominant lateral component. As seen in figure 3.14 (dashed lines), the vertical component depends on the opening sizes, but no marked influence of the mask width is noticed. With increasing mask width and etching time, the undercutting and the length of the bottom {100} planes increased. A comparison of etch rates in the experiments for 500 s and 1000 s showed faster etching for shorter times. This may indicate that the increased etched area under the mask combined with a diffusion limitation through the mask opening impact the rate. Both {311}A and {111}A planes with nominal lengths of 30 nm and 20 nm (defined at 300 s etching time) correspondingly became bigger when the etching time was longer.

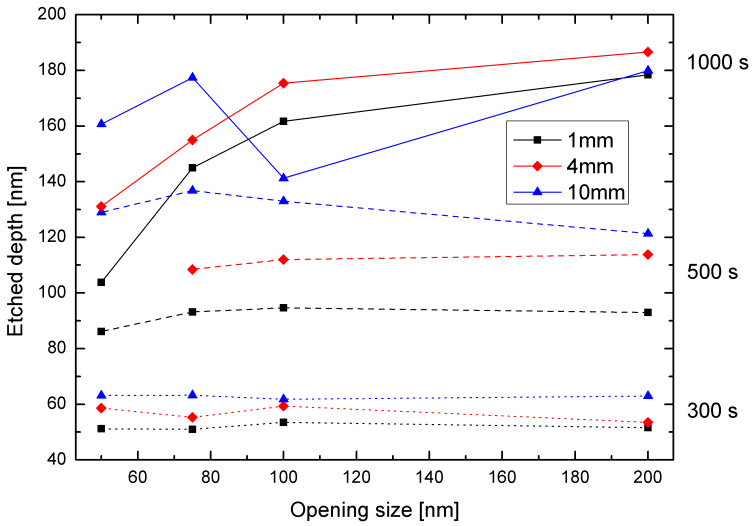

Figure 3.14: Etched depth vs opening sizes for different widths of protection lines along the [0-1-1] direction. The point for 100 nm opening with 10 µm protection line etched for 1000 s is due to the missed parts in the pattern as result of the bad local adhesion of HSQ.

Moreover, undercutting of the HSQ mask was seen for both directions. After electron beam exposure, the openings had the designed sizes but were subsequently enlarged during in-situ etching. This raises the question about HSQ resistance during etching. HSQ edge etch rate was observed to be approximately 6 nm/min (determined after regrowth of epitaxial layers) with no significant thickness reduction of the mask pointing to very slow vertical etch rate. A reason for this may be that HSQ edges were exposed with a slightly smaller electron beam dose leading to poorer edge etch resistance. In addition, annealing at 650 °C temperature showed a HSQ thickness decrease in 10 nm, which fits the data obtained for post-apply thermal curing (see figure 3.5).

The observed difference in the etching behavior during the low pressure vapor phase etching is opposite to what is typically seen in wet chemical etching but is consistent with earlier work [125]. The {111}A planes contain only In atoms with three bonding electrons and one dangling bond compared to five electrons per atom for {111}B planes where the dangling bond is occupied by two electrons [126]. Because the Br radicals interact with In, as was outlined in the previous section, {111}A planes were determined more chemically reactive than {111}B which were the slowest etch planes. By analogy to in-situ PCl_3 etching [125], the dangling bond without electrons can be attractive for Br^- radicals and the filled orbitals in the case of {111}B make an etching barrier. The different planes developed during etching play an important role for further selective area growth, which is addressed in the following section.

3.4 Selective area epitaxy

Selectively grown structures are usually bounded by the slow grown crystallographic planes. The presence of a mask in MOVPE leads to a concentration gradient of the growth precursors near the masked region, and, as a consequence, thickness enhancement and composition changes are observed [36].

3.4.1 SAE of InP/InGaAs/InP

To assess the significance of this process, a single InP/InGaAs/InP QW was deposited in the etched trenches. InGaAs/InP layers were grown at a temperature of 610 ºC using standard precursors (trimethylindium, trimethylgallium, arsine, and phosphine) and hydrogen as a carrier gas. The V/III molar flow ratio was 68.3 for $In_{0.53}Ga_{0.47}As$ and 145 for InP with planar growth rates of 1.05 nm/s and 0.45 nm/s, respectively.

Before discussing the material deposited in U-shaped trenches, considering growth in trapezoidal-shaped grooves along the [0-1-1] direction. When InP is deposited first, it starts filling the corners of the trapezoid, which are the energetically favorable places to initiate deposition. As a result, the groove changes its profile to a semicircle (see figure 3.15 (a)). This leads to distribution of the InGaAs material differently across various opening widths. While InGaAs grown in 250 nm openings follows the groove shape, the material is mostly located in the central part of the InP matrix for 100 nm openings as illustrated in figure 3.15 (b). Atoms

migrating from the mask form thickened regions in the area closed to the groove edges (see, for example, figure 3.11 or figure 3.15 (a)), which is a common characteristic in planar selective area growth [36], [53], [67], [127], [128]. Symmetry in the grown material is observed among almost all structures. The capping InP layer, which planarizes the surface, preferably grows on the (001) surface.

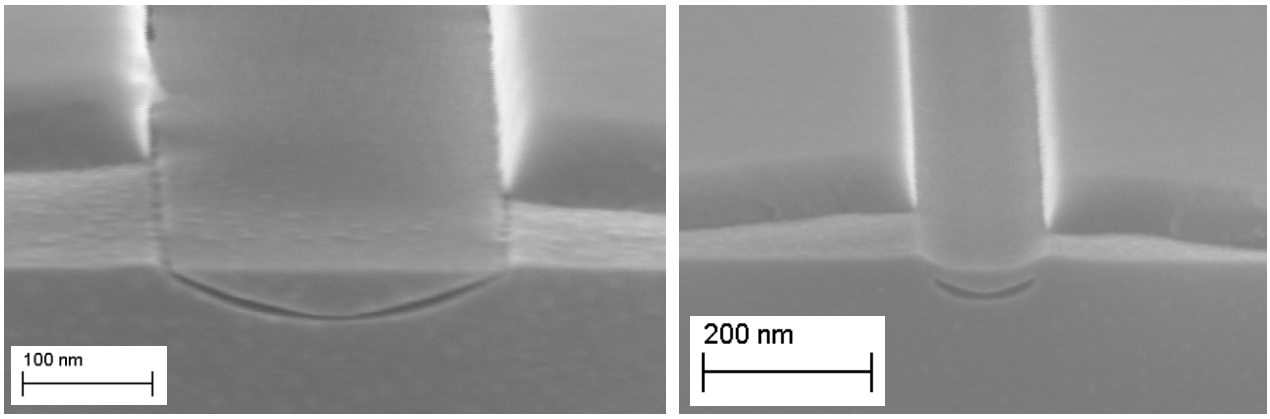

(a) (b)

Figure 3.15: SEM images of a buried InGaAs single QW of 250 nm (left) and 100 nm (right) width with HSQ mask on (0-11) InP plane

If desired, the InGaAs layer can have a flat geometry (figure 3.16). To achieve this geometry, prior InP needs to fill the etched trench completely assuring the planar surface. When growth continues above the surface level, InP favoring different crystallographic planes, in particular, there are three planes evolved: {111}, {311}, and {100} along the [0-1-1] direction. Since one of the main goals of the current work is demonstration of active photonic crystal slabs, where the flat surface is essential to confinement light inside the membrane, the growth above the surface was not investigated in great details. The gable shape of the material was obtained during InP overgrowth above the surface with the configuration of the mask as periodic squares of 100 nm×100 nm.

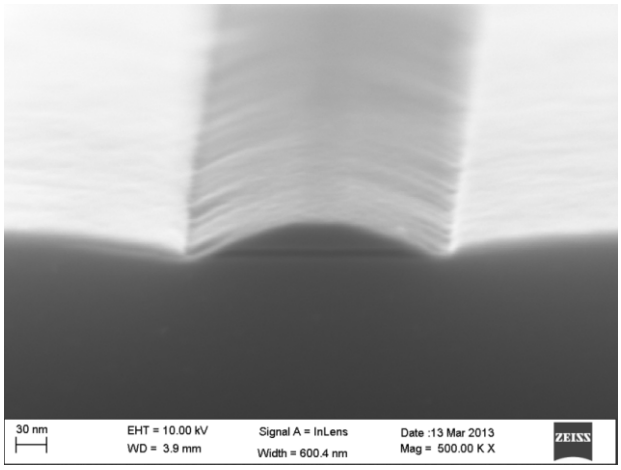

Figure 3.16: SEM image of a single flat InGaAs QW

3.4.2 SAE of InGaAs/InP

Furthermore, the growth of a single InGaAs/InP QW without an InP buffer was investigated. As illustrated in figure 3.17 (a) for the [0-1-1] oriented mask, the growth of the InGaAs layer takes place on {311}B and {001} planes without any deposition observed on the {111}B. While the growth in openings smaller than 100 nm are connected and crescent-shaped, the 250 nm opening has two regions of InGaAs separated by InP (figure 3.17 (a)). In the perpendicular direction, the InGaAs growth is mostly present on {311}A spreading partially on {111}A and {100} planes (figure 3 (b)). In addition, the InP growth occurs under HSQ mask due to poor adhesion to fill the void. Under the aforementioned conditions no growth on the mask was observed indicating good selectivity.

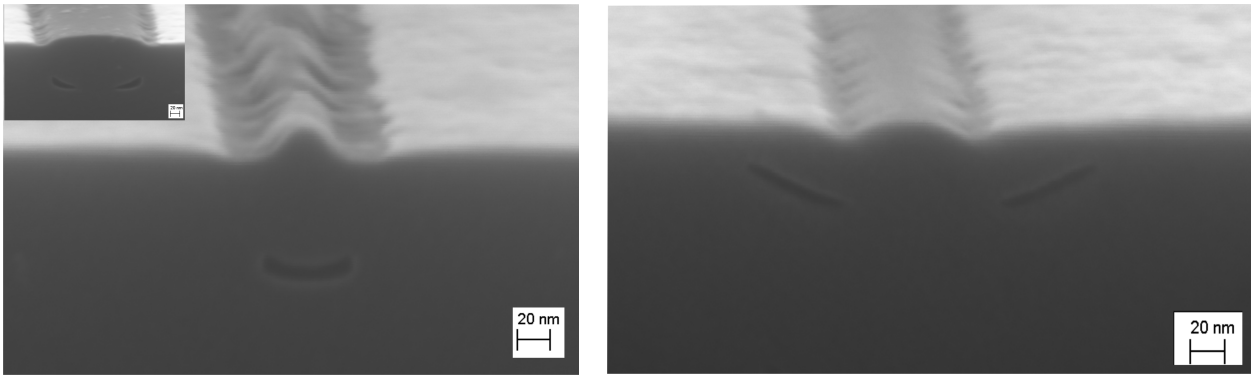

(a) (b)

Figure 3.17: Cross-sectional SEM images of selectively grown InGaAs/InP with 100 nm separation stain-etched along [0-1-1] (a) and along [0-11] directions (b). Inset shows 250 nm opening

In summary, selective area growth on in-situ prepared non-planar surfaces allows obtaining different shapes of the InGaAs/InP quantum well. Evolving different crystallographic planes leads to various incorporations of species on these planes, so raising a need to investigate crystalline properties and composition of the material by TEM. The next chapter addresses the fabrication of the specimens for TEM and photonic crystals with buried SAG material.

3.5 Summary

The fabrication processes of selective area grown quantum wells on in-situ prepared non-planar surfaces have been described in this chapter. The parameters for HSQ as a SAG mask was found to be XR1451-02 spun on 30 nm thickness, pre-baking 2 minutes at a temperature of 120 °C and 2 minutes at 220 °C, the electron dose of 4000 μC/cm^2 and the development condition is 90 s in 1 AZ400K: 2 H_2O at room temperature.

Using different mask orientations, crystallographic dependent etching of InP can be observed during surface preparation by 98 % H_2SO_4 as well as when carbon tetrabromide (CBr_4) is used as an etchant. Etching in sulfuric acid revealed the trenches having {112}B and {100} planes along the [0-1-1] direction and {211}A and {100} planes along the [0-11] direction. U-shaped grooves

were formed in the time of CBr_4 etching along the [0-1-1] direction, terminated by {111}B planes with an ~15 nm {100} plateau and transitional {311}B planes, developed in a self-limiting manner. In the perpendicular direction [0-11] etching with a dominant lateral component driven by fast etched {111}A and {311}A side planes was observed.

An InP grown after etching leads to a wider distribution of InGaAs across the width of the different openings. A directly grown single InGaAs QW in the etched grooves demonstrated different QW profiles: a crescent-shaped on {311}B and {100} planes (along the [0-1-1] direction) and two separated quarter-circle curvatures grown preferably on {311}A along [0-11].

Chapter 4. Integration of the SAG material into InP specimens/slabs

This chapter concentrates on the development of a fabrication process to incorporate the developed SAG material into InP specimens/slabs of different applications. First, the design of pillar-shaped specimens for transmission electron microscopy to investigate the compositional and structural properties is described. Then, the optimization of alignment marks is presented to minimize the misalignment error. A detailed description of the fabrication process steps for needle-shaped specimens and photonic crystals with SAG is done in the two final sections respectively.

4.1 Design of specimens for TEM

Studying the selective area grown material by transmission electron microscopy (TEM) can determine its compositional and structural properties with high accuracy. Along with conventional TEM, high-angle annular dark-field (HAADF) scanning transmission electron microscopy (STEM) and atom probe tomography (APT) allow assembling 3D information about structures of interest. Specimens (or lamellas) in cross-sectional geometry are often prepared by focus ion beam (FIB) milling and lift-out operation. The accessible tilt range of these lamellas with a typical thickness of hundred nm is constrained because they no longer transparent enough for electrons when traversing the specimen at an angle. To overcome this limitation, the geometry of specimens can be modified to a needle shape, which can be prepared either by FIB milling or by combination of wet etching and lithography. The advantage of the latter compared to FIB preparation is the absence of damage to the semiconductor, such as amorphisation, intermixing and Ga implantation.

A single needle-shaped specimen with the investigated SAG material is designed as a 4 μm long and 50 nm in both width and height free-hanging needle attached to the semiconductor substrate. The fabricated structures are detached by cleaving and mounted onto a suitable grid for further TEM investigation. To incorporate SAG quantum structures into pillars, the pattern layout is presented in figure 4.1 where the red area is a selective mask and the green one is the needle. The challenge in current fabrication is that the SAG pattern and the pattern for specimens themselves are made by electron beam lithography. So precision alignment of two patterns to each other is essential, particularly, working on a nanometer scale. This emphasizes the importance of the alignment mark optimization highlighted below.

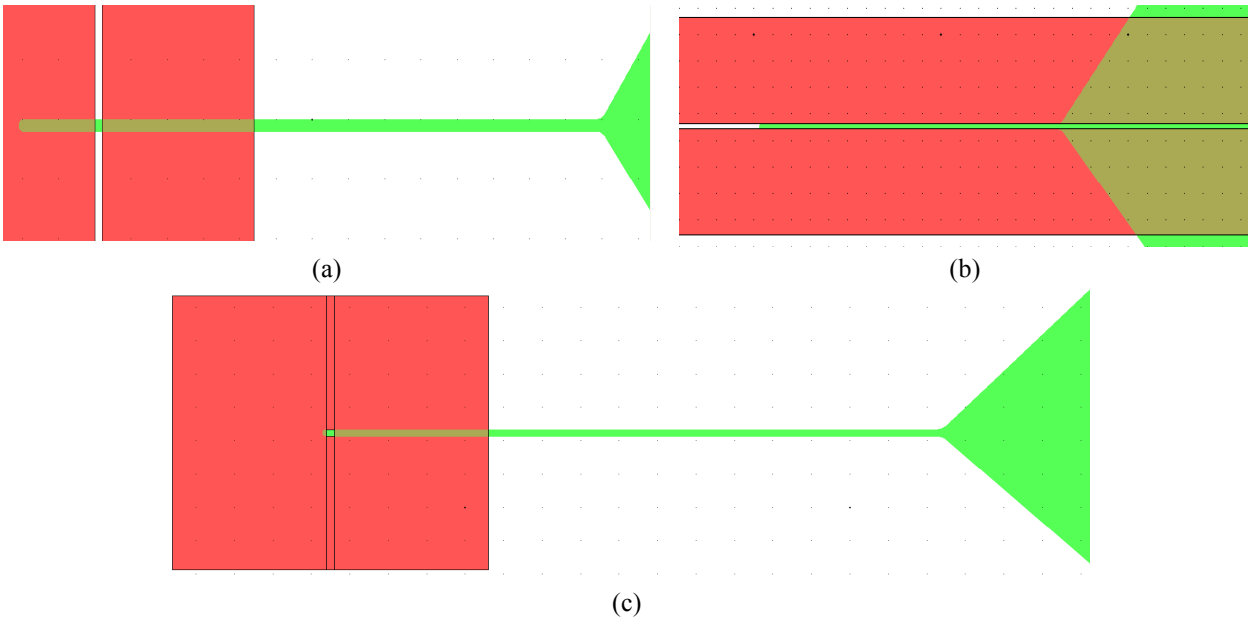

Figure 4.1: Design of pillar-shaped specimens with SAG QWs (a and b) and QDs (c)

4.2 Alignment mark optimization

The quality of marks is crucial for manual alignment of several patterns. The negative impact of misalignment is the loss of the SAG material in the needle-shaped specimens. For this reason, layout misplacement can be applied as shown in figure 4.1 (a).

The first batch of alignment marks was made by a combination of conventional UV lithography patterning and wet etching, since this approach is faster and cheaper than e-beam lithography and dry etching. An alignment mark is designed as a big cross with an open region inside, where the small cross of 2 µm in width is placed (see figure 4.2). A total of 16 marks were formed on an epi-ready (001) InP substrate in AZ5206E positive tone photoresist. A 600 nm film was spun on at 4000 rpm for 30 s followed by thermal baking at 90 °C for 90 s. The resist exposed in vacuum mode for 7 s was developed in 1 AZ351B: 5 H_2O for 60 s, thereafter, post baking at 120 °C for 2 minutes was employed.

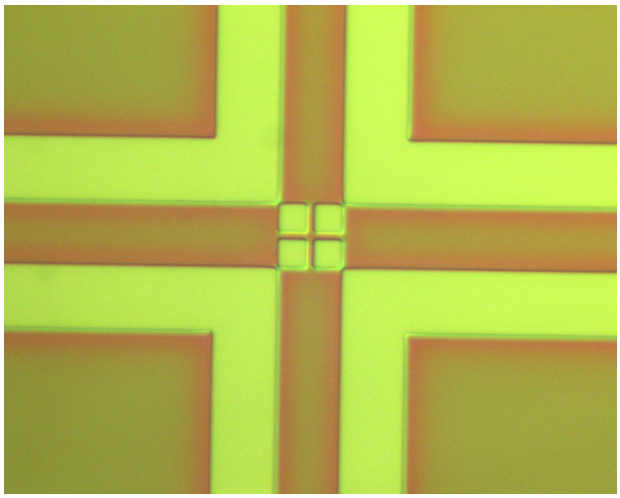

Figure 4.2: Optical microscope image of a fabricated alignment mark in AZ5206E

After pattern creation, the marks were transferred into the InP substrate by wet etching using hydrochloric acid (HCl). This type of etchant provides crystallographic dependant behaviour [126], where, in practice, crystal planes with low etch rate define the etching profile. Sidewalls of slow etched planes, in general, are inclined. Structures, such as crosses, would have different profiles of two intersecting lines. Considering the etching process, the dissolution of InP is based on the exchange of bonds between In-P and H-Cl that resulted in In-Cl and P-H bonds [129] having phosphine (PH_3) gas and hydrolysed InCl as the products of the reaction:

$$InP + 3\ HCl \rightarrow InCl_3 + PH_3 \tag{4.1}$$

To moderate InP etching, phosphoric acid is added in volume parts of 1 HCl: 4 H_3PO_4. When working without a stop layer underneath, the etching time controls the shape of the inner cross as the etch undercuts the resist mask. As seen in figure 4.3, one line oriented along the $[0\bar{1}1]$ direction vanished and the second one along the $[0\bar{1}\bar{1}]$ direction has inclined sidewalls. Even the shortest applied time of 15 s was too long for complete survival of the structures. Moreover, the parameters of the photo exposure and the resulting line width are significant for the amount of material left after etching.

After etching the AZ5206E resist was stripped 5 minutes in acetone, 1 minute in ethanol, and 1 minute in running DI water followed by nitrogen blow drying and oxygen plasma cleaning. In all processes described below, AZ5206E resist is used with the same parameters for spin coating, exposure, development and stripping presented in this section, even when the pattern is altered.

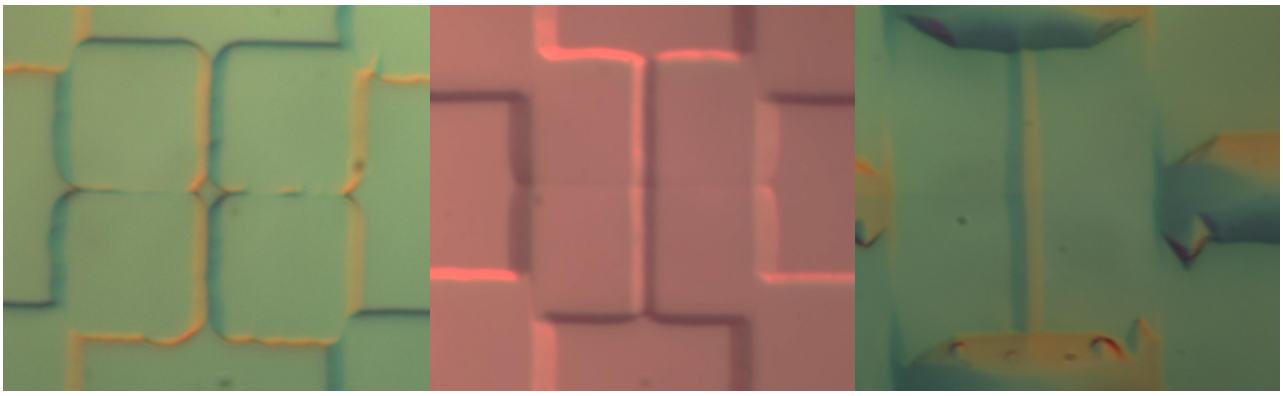

(a) (b) (c)

Figure 4.3: Optical microscope images of 2 µm wide inner cross after wet etching in 1 VP HCl: 3 VP H_3PO_4 for 15 s (a), 30 s (b), 2 min (c)

For the project only manual alignment was done and this makes symmetry of intersection lines criteria important. The sample etched for 15 s was investigated further by SEM (figure 4.4). The inner part of the cross has uncertainty 150 nm in determination of the center position. This fact increases the misalignment error, consequently, the marks are not suitable for high-precision alignment.

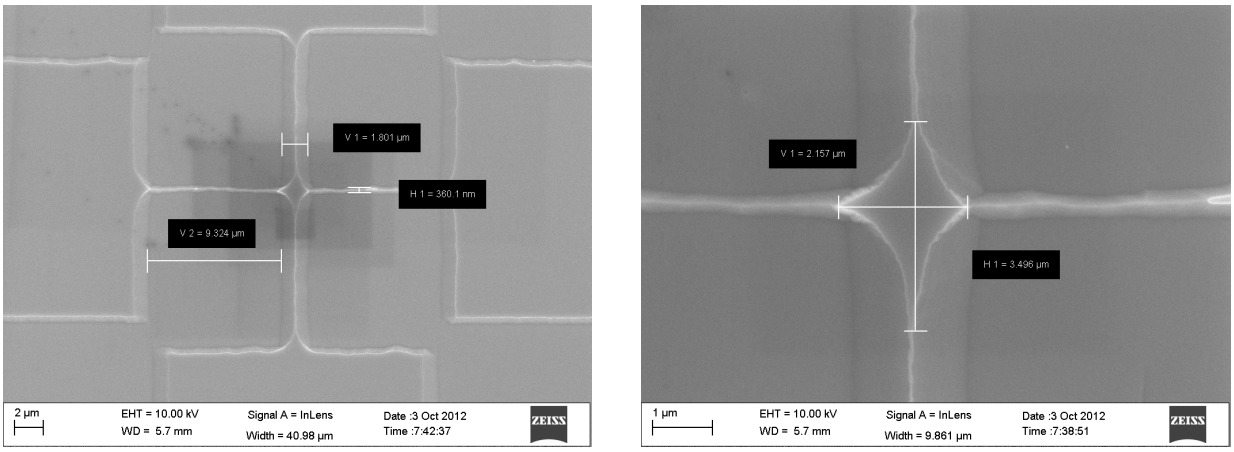

(a) (b)

Figure 4.4: SEM image of the inner cross (a) and close-up view (b) after wet etching for 15 s in 1 HCl: 3 H_3PO_4

In an attempt to get a more symmetric mark, the mask was rotated on 45 degrees in relation to the major flat with the reference to work of P. Eliás at el. [130], who studied the photomask orientation about crystallographic planes. This attempt failed to obtain more useful shapes. The marks had a similar trend, such as not symmetric central center part, to the ones depicted in figure 4.4.

In light of these results, wet etching was replaced by reactive ion etching (RIE), which, in principle, allows forming the vertical sidewall profile along all crystallographic directions. The available equipment named “PLASSYS” operates at radio frequency (RF) of 13.56 MHz and has planar geometry. By applying a strong RF field, the plasma is ignited between two parallel

plates: the upper one is called an anode and the bottom is called a cathode on which a quartz plate with the sample is placed. The gases, which form the plasma by colliding of free electrons to neutral atoms, come into the chamber though the small inlet in the anode (the lid in the current machine). In the plasma, positively charged ions are generated, accelerated, and strike the sample surface. Additionally to the ions, there is a large amount of free reactive radicals. Reactive particle arrives onto the surface, where chemisorption occurs and causes formation of the product molecules and desorption of them. Plasma etching is mostly chemical etching but physical sputtering, to a small extent, is always presented. If the incident energy of ions is high enough, the process results in sputtering of the surface atoms. At the back of the chamber the turbo pump is located together with a throttle valve that regulate the pressure. The pressure affects the directionality and energy of the ions. The lower the pressure, the more energetics and directed ions are due to fewer interactions in the plasma sheath. Depending on the process conditions, such as pressure, RF biasing, gas composition, the etching can be explained either by dominant chemical etching, sputtering or their combination. Predominantly, the movement of ions is vertically directed towards the surface thereby allowing to obtain anisotropic etch profiles. With regard to chemistry, the absence of a load lock chamber makes unfeasible to work with chlorine-based gases owing to its high corrosive nature. A combination of methane plus hydrogen (CH_4/H_2), therefore, was reported to be favorable over Cl_2-based etchant giving smoother sidewalls and less surface roughness.

Using a CH_4/H_2 mixture [131], anisotropic etching of InP can be realized. Methyl radicals (CH_3) and H radicals interact with InP producing $In(CH_3)_x$ and $In(C2H_5)_x$ compounds and phosphine respectively. In addition, methyl radicals create carbon-reached polymer deposition on the surfaces, which prevents further etching, in pure methane discharges. Oxygen plasma can remove this polymer, thus the used process is cyclic containing an O_2 cleaning step after every etching loop. Priory to all InP MORIE processes, the sidewalls of the chamber are coated with polymer to not affect the etch rate by sidewalls absorption of etchant species. Cleaning removes this coating restricting the etch rate. Overall, etch rate, deposition rate of polymer film and anisotropy can be controlled by relative fraction of CH_4/H_2. The lower the concentration of methane in the plasma is, the slower the etch rate and the smaller angle of the sidewalls are.

Before employing dry etching, photolithography and deposition of a hard mask of silicon dioxide was done. SiO_2 was deposited by plasma enhanced chemical vapor deposition (PECVD) using silan/nitrous oxide/nitrogen ($SiH_4/N_2O/N_2$) gases. The thickness of the hard mask was 85 nm and the pattern was formed in AZ5206E photoresist. After pattern development, the silica was etched in the RIE chamber using fluoroform/oxygen (CHF_3/O_2). Then resist was stripped in acetone and ethanol followed by oxygen plasma cleaning. After that, etching of InP by RIE was done using the following parameters: CH_4/H_2 flows of 8.4 sccm: 42.0 sccm, power of 60 W, V_{bias} of 450 V, process pressure of 80 mTorr. Finally, the silica was etched away in buffered hydrofluoric acid (BHF).

The next step in processing is epitaxial deposition of the active material, which, actually, can destroy the cross sidewalls sharpness. By comparing the marks formed before and after epitaxial

growth, the influence of the grown layers on the quality of alignment marks can be seen. Figure 4.5 (a) shows the alignment mark with 1 µm of InGaAs and 650 nm of InP on top. A cross of few hundreds nm formed due to altered growth rate on different crystallographic planes. These marks were used to align the first batch of the devices leading to misalignment accuracy more than 200 nm. The marks created after epitaxial growth possess rough edges and was not used for device fabrication. The crosses in such a way are not applicable for alignment.

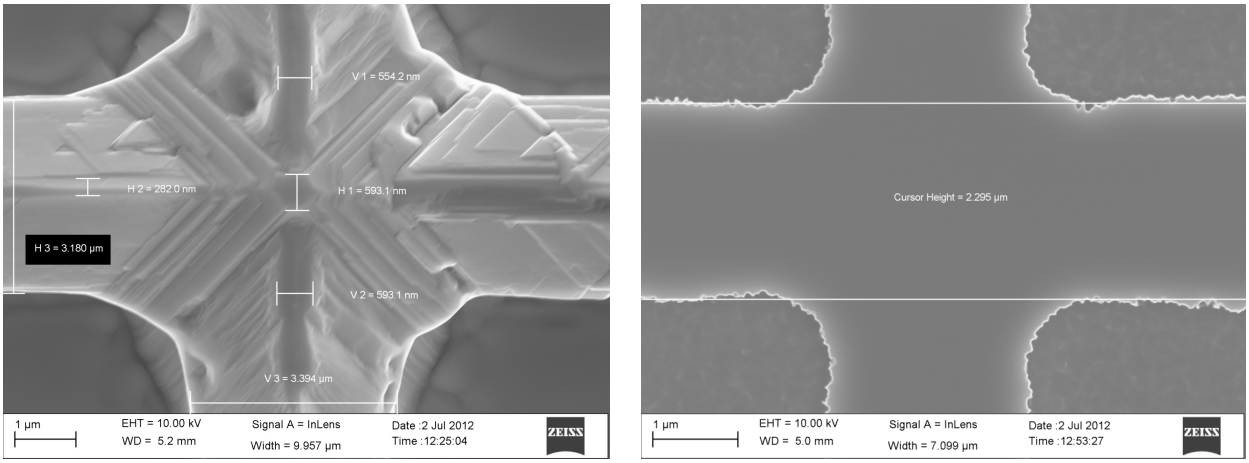

(a) (b)

Figure 4.5: Alignment marks made before regrowth with deposited layers on the top (a) and the one made after growth (b)

Moving further, the alignment marks were patterned by e-beam lithography. Alignment marks were design as the previous ones, but scaled down and the inner corner had a line width of 1 µm whereas in the crossing in the middle part the line width was reduced to 100 nm. In case the small part is lost during processing, the wider lines would still be present. The marks were written in the same run as the protection mask for epitaxial growth. Poor adhesion of HSQ on InP (see section 3.1.1) hinders using the same dose for both layouts. An example of a cross with poor adhesion is presented in figure 4.6 (a). Small features require a higher dose, which was chosen to be 7000 µC/cm^2.

The contrast during alignment is achieved by a height difference in InP, so the marks need to be transferred into InP. To ensure that the active material is not etched away during RIE, a mask in AZ5206E resist was applied to protect active material. Due to 30 nm HSQ layer, the etch depth was only 250 nm (RIE selectivity of HSQ:InP = 1:9), however, it is enable good contrast for SEM imaging. As seen in figure 4.6 (b), the current process was successful for obtaining symmetrical alignment marks with straight sidewalls of approximately 100 nm in width.

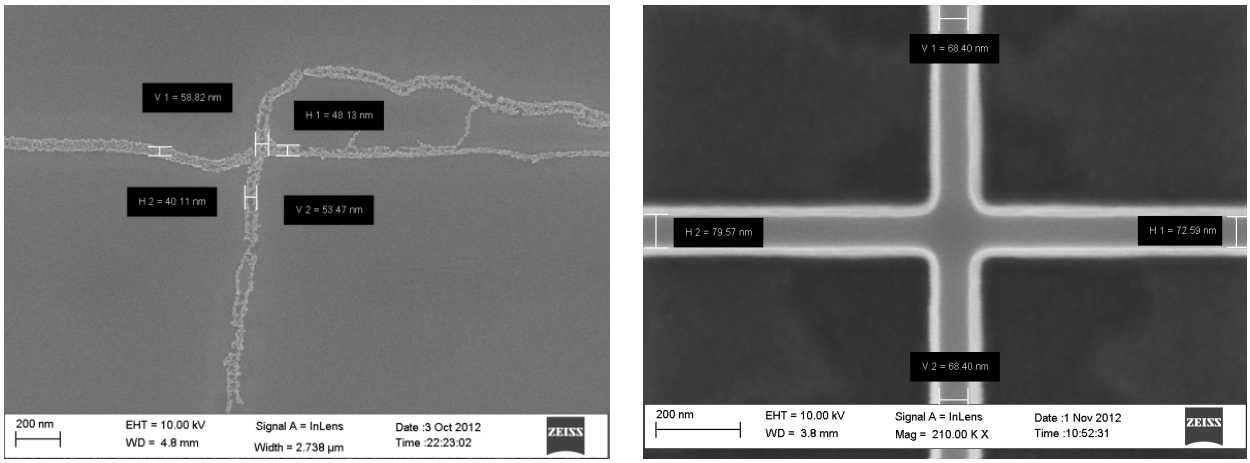

(a) (b)

Figure 4.6: Plane view of an alignment mark with pour adhesion (a) and a good one (b)

4.3 Fabrication of needle-shaped specimens

The fabrication of needle-shaped TEM specimens involves reactive ion etching, glass deposition, inductively coupled plasma etching, selective wet etching and critical point drying. Owing to the fact that the entire structure was produced in the InP material except a QW InGaAs layer, it is impossible to realize a free-hanging structure by conventional wet etching without an extra step, which comprises sidewalls protection by a silicon dioxide layer. An overview of the entire process is presented in the table below:

#	Description	Drawing
1	The fabrication starts from epitaxial growth. An InP layer of 40 nm and an InGaAsP stop layer of 10 nm, which are defined the total thickness of the needle-shaped specimens, were deposited during this step.	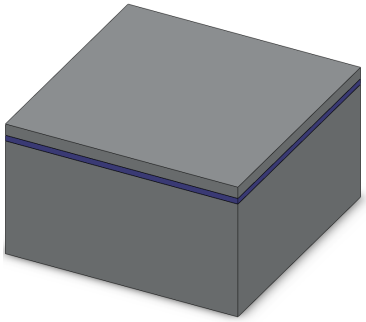
2	A SAG pattern was drawn in the XR1451-02 resist of a 30 nm thickness. The electron dose and the current were 4000 µC/cm^2 and 10 nA, respectively. Also, in this run the alignment marks are drawn with 7000 µC/cm^2. After that, the resist is developed 90 s in 1 AZ400K: 2 H_2O (see section 3.1.3 and 4.2).	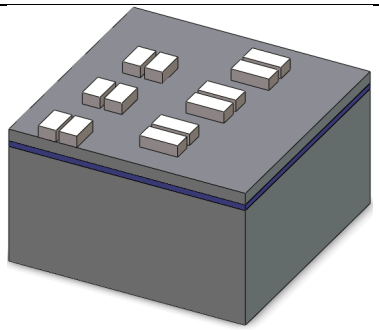
3	Before loading samples to the MOVPE reactor,	

	surface was prepared by plasma cleaning and native oxide etching in concentrated H_2SO_4 (see section 3.2). In-situ etching and a single InGaAs/InP QW were done (see sections 3.4 and 3.3.1). The HSQ mask was removed afterwards.	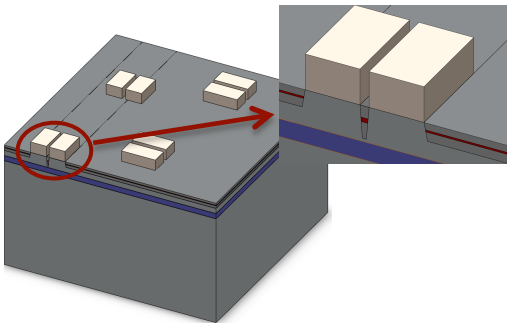
4	The specimen pattern was made using Fox-15 spun on at a 350 nm thickness. Prior to exposure, the resist was removed manually from the marks. E-beam patterning of the pillars was done with a dose of 4000 $\mu C/cm^2$ and the current of 15 nA. The resist was developed 150 s in 1 AZ400K: 3 H_2O.	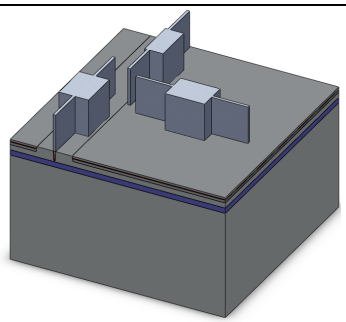
5	First RIE etching of 150 nm InP including the QW layer was performed to open the QW for further protection by glass.	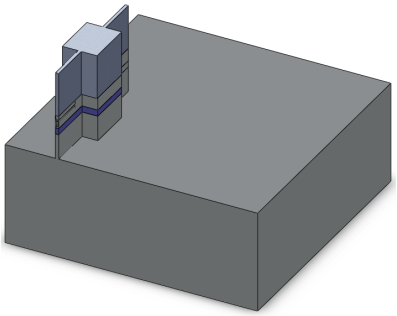
6	40 nm silicon dioxide was deposited to cover the sidewalls.	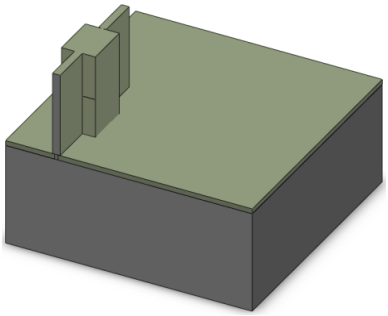
7	The glass layer was etched in ICP-RIE in a way that left the sidewalls covered with glass followed by 450 nm InP etching in RIE, which is not shown in the right picture.	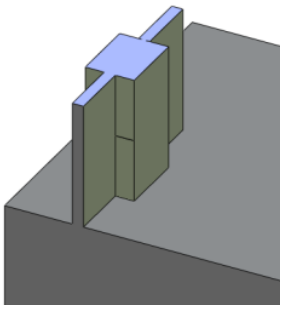

8	To realize the free-hanging needle, the wet etching was done 90 s in 1 HCl: 1 H_2O. Then the silica layer was removed 4 minutes in 40 % HF. Critical point drying was applied because the needles are too fragile to apply conventional nitrogen blow-drying.	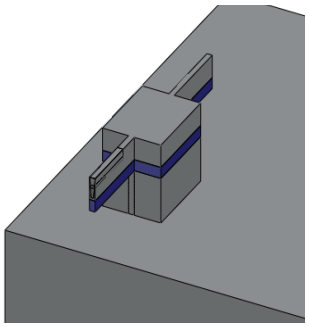

After two e-beam writings and RIE etching (steps 1-5) the structures were covered by silicon dioxide (see figure 4.7 (a)), which was etched by RIE in the earlier experiments (step 7). In this manner, the upper part, where the structures of interest are placed, subsequently, protected during final wet etching. However, the fabricated specimens were only ~15 nm thick (figure 4.7 (b)), which believed due to etching away of the protection layer during the RIE. Thus, the glass etching process was optimized in ICP-RIE in a way to increase vertical component of etching whether lateral is diminished.

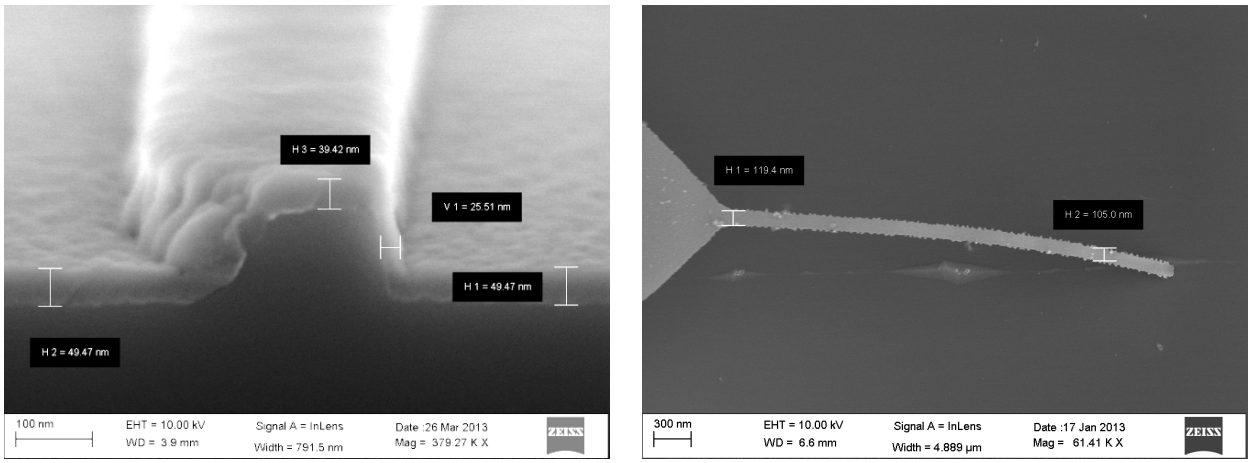

(a) (b)

Figure 4.7: Cross-sectional view of 40 nm deposited SiO_2 on the etched InP (a) and the released needle-shaped specimen

ICP-RIE etching has an advantage over conventional RIE in uniformity and high density of plasma working at low pressure. A magnetic field induces by applying an RF current and produces plasma. An extra bias can be applied to the sample holder platten allowing independently controlling the density of plasma and the amount of coming to the surface ions. This gives extra degree of freedom for optimization of the fabrication process. Moreover, ICP allows operates at low pressure (<20 mTorr) while being able to disassociate the gasses to a high ion density through a large coil power. To provide vertical direction of the ions, the etching process was modified by increase of the platter power thereby enhancing the sputtering component.

Etching of silicon dioxide was realized by carbon tetrafluoride (CF_4) together with hydrogen. During etching, the C_3 and F radicals adsorb where, in particular, C_3 radicals bond with O_2 at the surface forming CO, COF_2, and CO_2 byproducts; F radicals bond with Si forming SiF_4. Adding H_2 helps removing F radicals out of the system in a way of composed HF gas. Polymerization presence on all surface decreasing etch rate. In contrast, ionic bombardment has enough energy for interaction of carbon/hydrogen with surface oxygen.

The used recipe has the following parameters: CF_4/H_2 ratio of 15/5 sccm, platter power of 100 W, coil power of 150 W, pressure of 3 mTorr, RT. This recipe gives etch rate of 30 nm/min. After ICP etching, the cross-sectional geometry was checked indicating the glass protection covering of the upper part where it should be (figure 4.8). Two images are different specimens because it is impossible to hit a 4 μm long object with the available equipment; therefore, long test structures were added for cross-sectional view. As observed in the left picture, ICP also etches InP resulting in the widening of the needles.

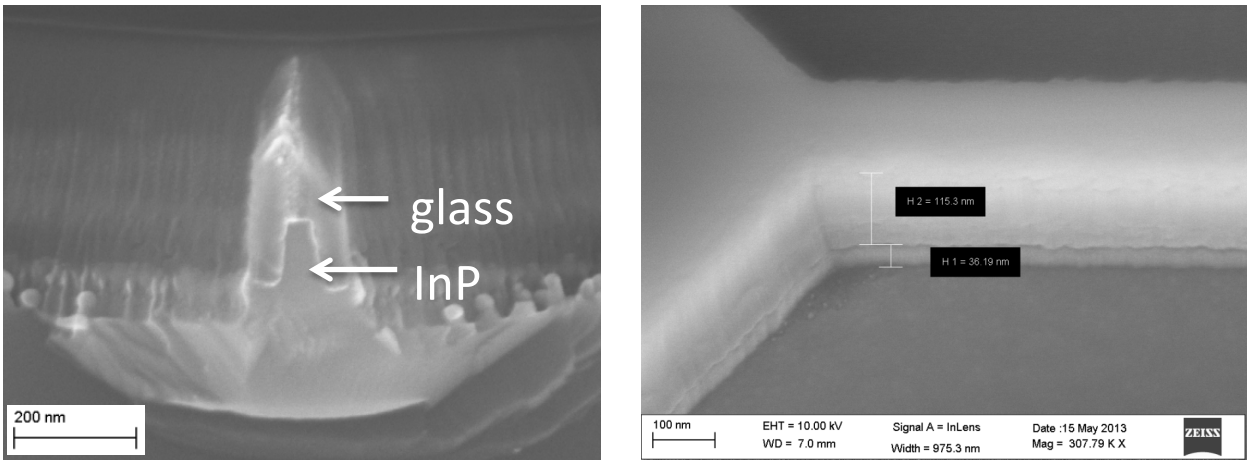

(a) (b)

Figure 4.8: SEM images of cross-sectional geometry (a) and side view (b) of the pillar-shaped specimens after SiO_2 etching by RIE-ICP

Although the silica stays after ICP etching, no detectable improvement compared to RIE ones in specimen robustness and layer presence was observed. The samples in cross-sectional geometry were examined after the following fabrication step, which is RIE etching of the semiconductor. The glass was still on the sidewalls and InP was etched; however, the produced specimens were still too thin and fragile.

Investigation of the effect of hydrochloric acid on the protection layer was done. Before doing this experiment, the etching of InP with different concentrations of HCl was conducted using specimens with QDs buried into InGaAsP matrix. Data are listed in table 4.1.

Table 4.1 Etch depth of InP in HCl of an different concentration

#	Concentration	Time	Thickness, nm	Etch rate, nm/min
1	1:1 HCl:H_2O	5:00 min	1270	254
2	1:2 HCl:H_2O	10:00 min	297	29.7
3	1:4 HCl:H_2O	5:00 min	No data	-
4	3:1 HCl:H_2O	00:30 min	No data (too high concentration, no needles)	-

Needle-shaped specimens were released by 90 s in 1 HCl: 1 H_2O with the silica layer, which was removed by HF for 2 minutes at the following step. The specimens require that liquid tension drying is avoided to prevent them from breaking. Thus, critical point drying using isopropyl alcohol (IPA) was applied. Figure 4.9 illustrates that the glass protection layer is broken as well as the pillar-shaped specimens detached from the base platform. Falling apart of the protection cover during wet etching prevented successful fabrication of the pillar-shaped specimens. Another observation was the lateral dimensions increase compared to the e-beam lithography. This increase equals to the silica deposited thickness. Energy dispersive X-ray spectroscopy (EDS) analysis[6] showed the presence of Si on the top of the samples indicating silica left over from the processing.

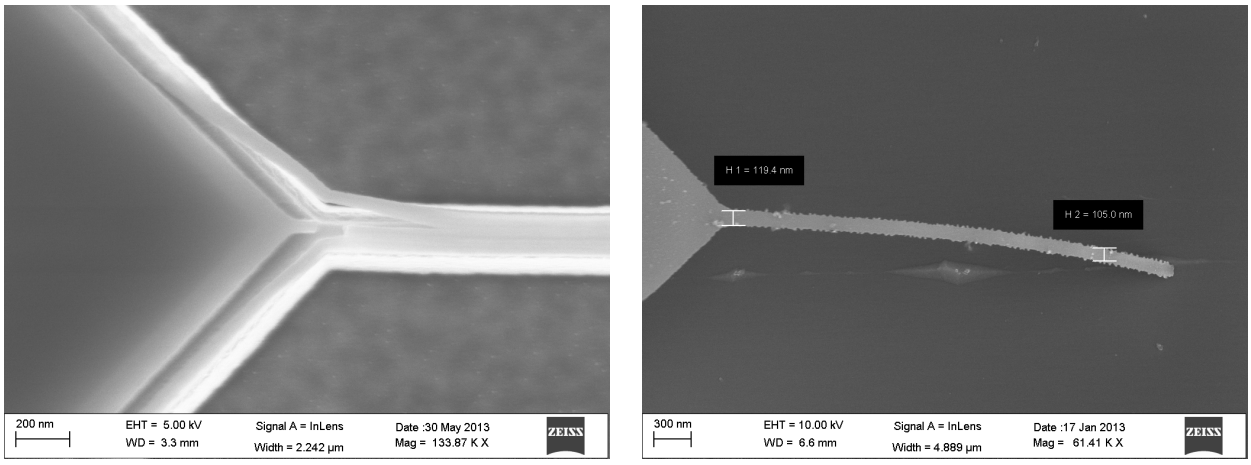

(a) (b)

Figure 4.9: SEM images of a pillar-shaped specimen after etching in 1 HCl: 1 H_2O (a) with silica presented and released one (b)

To summarise, none of fabricated structures were strong enough to be mounted on TEM grid and investigated. Post facto, it was said that the silicon layer was of bad quality related to not optimized process in PECVD.

[6] EDS analysis and the STEM work were done by Dr. Shima Kadkhodazadeh

4.4 Fabrication of photonic crystals with SAG

The core of this work is demonstration of photonic crystal devices with selectively grown active material with a focus on development of fabrication technology. Previous devices based on $In_{1-x}Ga_xAs_yP_{1-y}$ material suffered from the heating issue and, as a consequence, only optical pumping scheme under pulsed regime had been realized. A step towards continuous wave (CW) pumping of an air-suspended PhC membrane is the incorporation of selectively grown active medium in the heart of photonic crystal devices. This approach opens up the possibility to transfer the fabrication of a slab into InP, which has thermal conductivity of 68 W/mK compared to 4.2 W/mK for $In_{1-x}Ga_xAs_yP_{1-y}$, in other words, 16 times higher. Aiming for small power consumption around few μW for lasers, realization of the ultra-small active medium around few μm^2 is essential and can be achieved by the current technique for selective area growth. A brief description of the full fabrication process is shown below with the main steps drawn in figure 4.10:

1. **Epitaxial growth**. In order to bury a quantum well in the middle of a slab, the epitaxial growth was split into three phases. Here the first part of the InP membrane where the active layer was incorporated and 1 μm of InGaAs sacrificial layer were grown.
2. **Electron beam lithography for SAG**. XR1451-02 was spin coated at 3000 rpm resulted in a 30 nm thick film. Writing the protection mask, where PhC holes and tapers were located, was done with 4000 $\mu C/cm^2$, while alignment marks were drawn with 7000 $\mu C/cm^2$ to be able to put the PhC pattern in the desired place. The resist was developed 90 s in 1:2 AZ400K:H_2O (see section 3.1.3).
3. **Selective area epitaxial growth**. During this stage a single InGaAs/InP QW was grown preceeded by in-situ etching (see section 3.4 and 3.3.1).
4. **Alignment marks etching**. Since the contrast in SEM was achieved by a height difference, alignment crosses were etched down into the semiconductor using RIE. This step also included photolithography with the use of AZ5206E resist to protect the active material from dry etching and, eventually, HSQ removing in HF. (see section 4.2)
5. **Overgrowth**. Anterior to the overgrowth, a 70 nm thick selective silica mask was added to cover the alignment crosses from the deposition. Then, the top part of the InP membrane was grown. Posterior to this silica was etched 5 minutes in HF.
6. **PhC mask**. The next phase in the fabrication process was to make the photonic crystal air-suspended slab. First, 200 nm of silicon nitride (Si_3N_4) was deposited in the PECVD reactor. On the top of this layer, ZEP520A e-beam resist was spun on to arrive at 500 nm thickness. The selective removing of the resist and the hard mask on the alignment marks was done before e-beam exposure (see section 4.4.1).
7. **Electron beam lithography for PhC**. The electron dose and the current were 280 $\mu C/cm^2$ and 200 pA, respectively. After writing, the structures were developed 2 minutes in ZED N50 accomplished by manually stirring.

8. **Pattern transfer**. To transfer the pattern from ZEP520A to the silicon nitride mask, the etching in the RIE reactor was realized. Afterward the resist was stirred 2 hours in heated Microposit 1165 Remover with a low level of ultrasound followed by cleaning (see section 4.4.2).
9. **Semiconductor etching**. The etching of InP was done by RIE. Between cycles the oxygen cleaning was provided. After etching, the hard mask was removed in 40 % hydrofluoric acid for 5 minutes.
10. **Membranization**. In the end, the membrane was released in the mixture of 1 H_2SO_4: 8 H_2O_2: 80 H_2O for 5 minutes. To ensure complete removing of the sacrificial layer, the sample was stirred manually during etching process (see section 4.4.3).

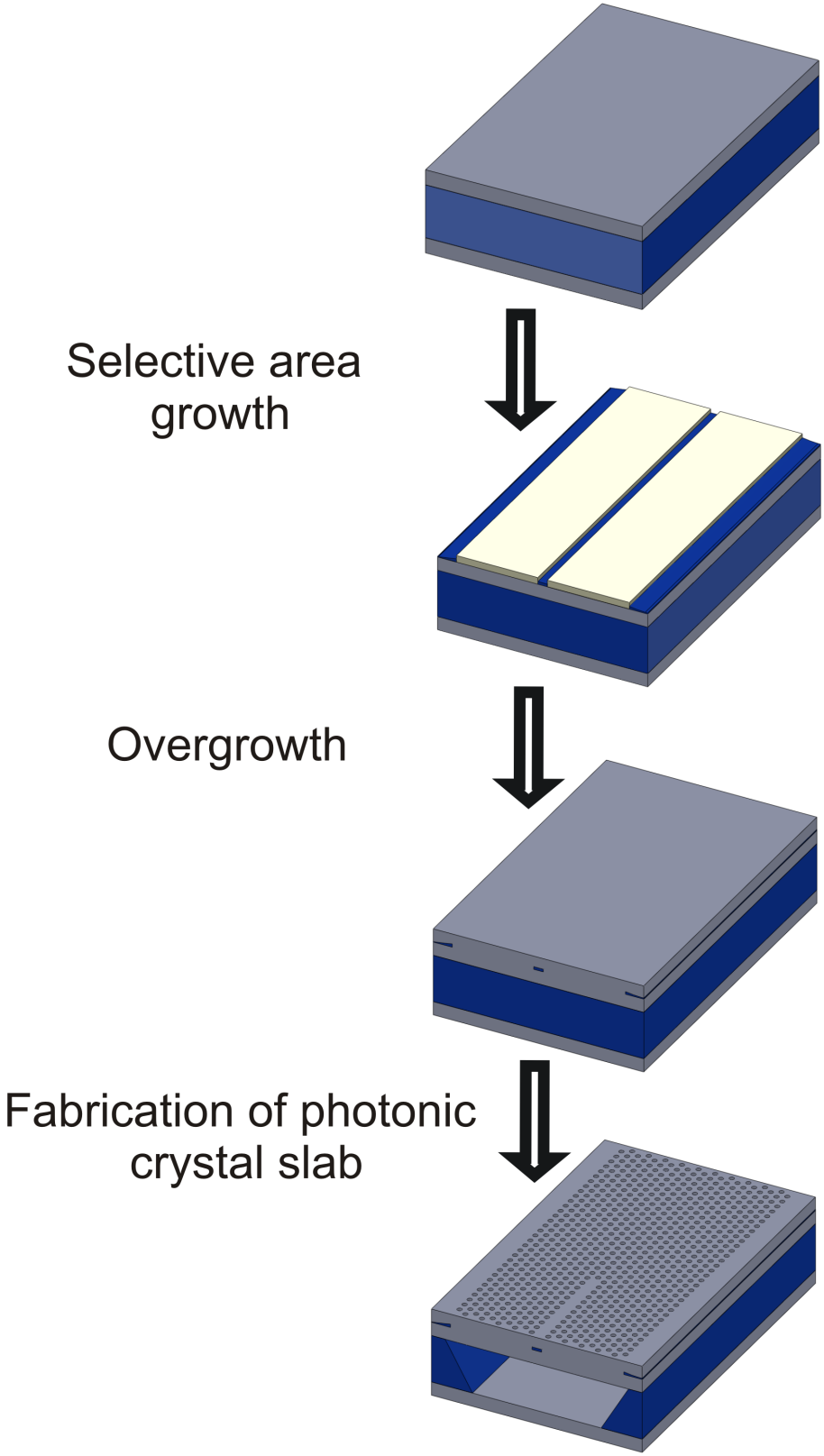

Figure 4.10: Schematic overview of the fabrication process of PhC with SAG material

Let us now consider the fabrication process in more details. In previous works on photonic crystals [87], [132], the slab had the thickness of 340 nm, which was used in this work as well. The slab was grown in two steps (#1 and #5 in the description). After growth of the bottom part, the pattern for the active material together with alignment marks was fabricated. The selectively grown structures need to be placed with accuracy of about 100 nm or less, which is to be compared to the waveguide width of 400 nm.

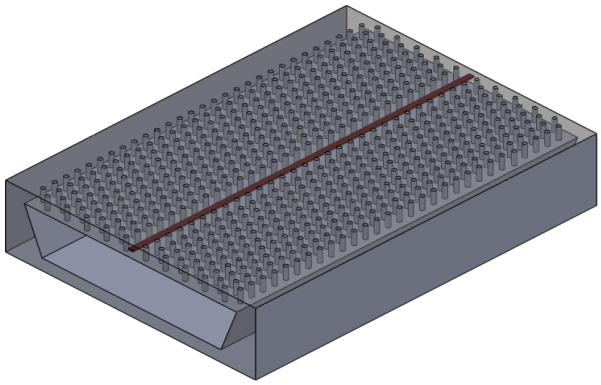

Figure 4.11: Drawing of a PhC with selectively grown active material

An unfortunate complication is that the epitaxial deposition of the top InP part of the membrane modifies the alignment marks increasing the misalignment value. To protect them, 70 nm of silica layer was deposited before epitaxy. To enhance adhesion of the AZ5206E resist to SiO_2, bis(trimethylsilyl)amine (HMDS) was applied for 15 minutes and the wafer was left in the air atmosphere for 5 minutes. Then, silica was selectively etched 1 minute in hydrofluoric acid using an AZ5206E protection mask to open the rest of the InP surface (see section 4.2). After all epitaxial growths, the patterned wafer is ready for the fabrication of photonic crystals.

4.4.1 Photonic crystals patterning

Photonic crystal pattern was produced in a positive tone electron beam resist called ZEP 520A. Silicon nitride (Si_3N_4) hard mask with a thickness of 200 nm was deposited by PECVD before the resist because ZEP deforms during III-V RIE. To minimize the charging effect during SEM alignment, the silicon nitride mask was etched from the alignment crosses in HF for 4 minutes. As stated above (see section 4.2), a selective protection mask was AZ5206E resist made by photolithography. Then the ZEP resist was spun on at 2600 rpm resulted in a 500 nm film, pre-baked for 5 minutes at 165 °C temperature. Again to improve in the contrast, the resist was manually removed from the alignment marks using anisol (methoxybenzene). Next, the pattern was exposed with a dose of 280 $\mu C/cm^2$ and a current of 200 pA.

The e-beam lithography writer has a 1000 μm by 1000 μm writing field with a stitching field accuracy of approximately 30 nm. The structures, i.e. waveguides, need to be designed no longer than 1000 μm and written in one field. Furthermore, the proximity effect must be taken into

account when PhC patterns are being prepared. The proximity effect leads to widening of the holes size because the neighboring areas of the exposed structures receive additional electron dose. The consequences of these changes on the PhC dispersion is discussed in section 5.4. Finally, the samples were developed 2 minutes in ZED N50 accompanied by manual stirring and cleaned 1 minute in IPA. Not only development affects the sizes of the holes, but also etching of both a hard mask and the semiconductor that is illustrated in the section below.

4.4.2 Reactive ion etching of PhC

After e-beam patterning, the mask was transferred to the silicon nitride layer. To obtain vertical sidewalls, highly isotropic etching is essential. It was done by RIE using freon/oxygen (CHF_3/O_2) chemistry with the following parameters: CHF_3/O_2 flows of 15/1 sccm, pressure of 10 mTorr, RF power of 13 W. The etch rate was found to be 17 nm/min and etching time was 18 minutes. Thus, samples were always over etched to obtain straight sidewalls. After hard mask etching, the ZEP resist was stripped 2 hours in 1165 remover, which was heated up to 70 °C, and a low power of ultrasonic agitation. The cleaning procedure afterwards was 5 minutes in acetone, 1 minute in IPA, and descumed in the oxygen plasma asher.

After stripping of the resist, the holes profile was tapered from a top to a bottom part. To reduce this, the etching time was increased to obtain the straighter sidewalls. Increasing etch time from 18 minutes to 19 minutes broadens holes size of around 15-25% depending on the original size. When small features are etched, it requires a thinner mask because not all radicals are directed vertically towards the surface. So a shadowing effect occurs, named a lag effect, slowing down the etch rate.

Table 4.2 Hole size changes during the fabrication process

Cavity length, μm	Design diameters, nm	Fabricated holes diameter, nm		
		After development	After resist stripping	After membranization
5	120	160	192	148
	130	164	207	156
	140	176	224	184
10	120	156	192	152
	130	164	207	160
	140	176	223	184

After that, the pattern was transferred further to InP using CH_4/H_2 chemistry (see chapter 4.2). During III-V dry etching, a choice of carrier underneath of a sample and its size can change the etch rate. The samples, therefore, were always cleaved to have the same size and placed on a ¼ of 2-inch InP wafer. Working with a 340 nm thick membrane, the etching time in CH_4/H_2 atmosphere was 45 minutes. Surface roughness, uniformity of holes and their straight sidewalls play an important role because all imperfections increase losses. To improve verticality of sidewalls, samples may require deeper etching than necessary to penetrate the membrane, but

drawback here is the broadening of the diameter of the holes. The evolution of the parameters during processing is presented in the table 4.2.

4.4.3 Membranization

In order to achieve an air-suspended membrane, an InGaAs sacrificial layer was removed in a 1 H_2SO_4: 8 H_2O_2: 80 H_2O solution for 5 minutes. Prior the Si_3N_4 layer is removed by 5 minutes in 40% HF. To guarantee the complete removal of the material, etching was accomplished with manual stirring of samples. The slab is robust after etching, thereby can be dried by nitrogen blowing. Figure 4.12 shows the released slab and the inset presents the top view of the holes having a slightly square shape. One possible explanation for this is anisotropic etching of InP during the long membrane etching.

A severe drawback of this fabrication process is that the misalignment can be checked only when the membrane is released. If the InGaAs QW touches the holes due to misalignment, it is etched away. The smallest obtained misalignment value was 65 nm (see figure 4.12 (b)). The measurements along with theory and design of the fabricated photonic crystals waveguides will be carried out in the section 5.4.

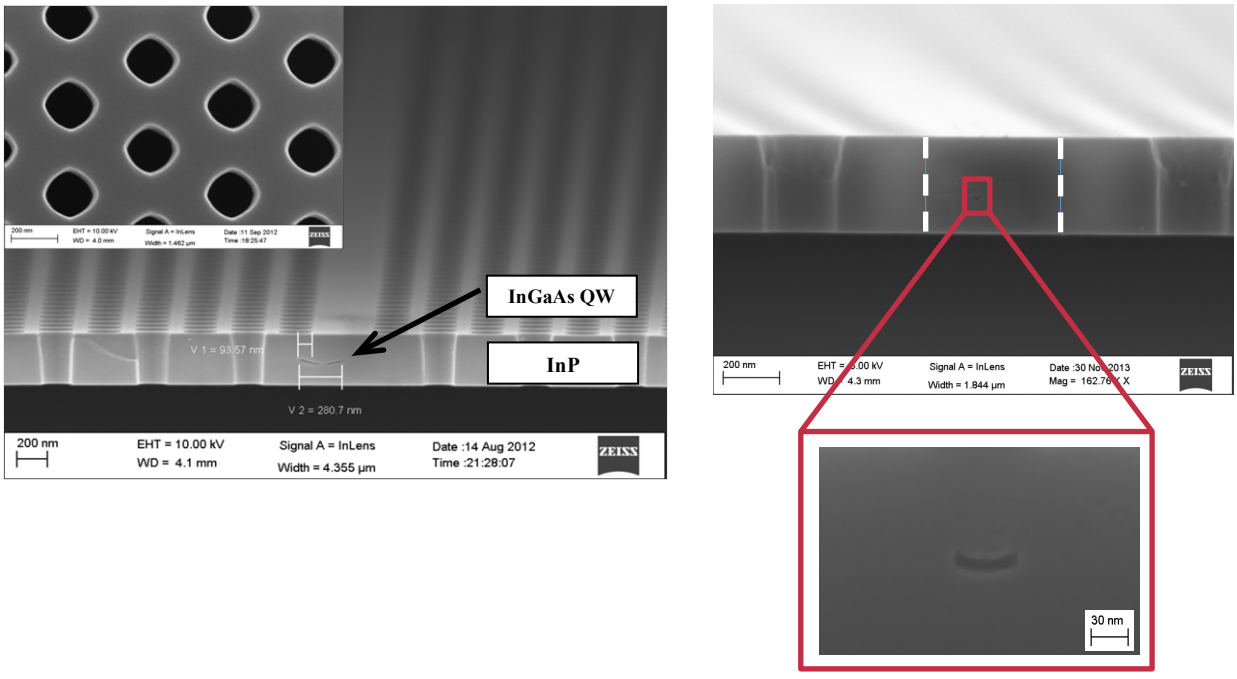

(a) (b)

Figure 4.12: SEM image of photonic crystal waveguide with selective area material (a) and stained-etched SAG QW in the PhC waveguide region (b)

4.5 Summary

The fabrication error for manual alignment of two patterns was minimized via the improvement of the alignment marks quality. In additional, the fabrication process was modified to obtained/keep the marks of satisfactory quality.

The best misalignment value was of 30 nm in one direction and 40 nm in another one for needle-shaped specimens. However, the protection of sidewalls by silicon dioxide falls off during the last step of wet etching possibly due to the poor quality of the glass layer, thus the adhesion can be improved via improving the glass quality.

During fabrication of photonic crystals, the misalignment value was slightly worse i.e. 65 nm. This is related to the additional overgrowth of InP that demands on the extra manipulations with the protection layers and can decrease the marks quality.

Chapter 5. Characterization of SAG structures and photonic crystals

When developing new methods for epitaxial material deposition, the examination of their optical properties is essential along with imaging them at high resolution. Therefore, this chapter is devoted to investigation of selectively grown structures by different techniques. The first section contains visualization of the selected samples at atomic resolution by scanning transmission electron microscopy. Cathodoluminescence measurements are demonstrated in the second section. The third section contains photoluminescence spectra of a single InGaAs/InP QW with an InP buffer layer underneath and the fourth one - the PL study of directly grown InGaAs/InP in in-situ etched trenches. Amplified spontaneous emission measurements of fabricated photonic crystals are presented in the last section.

5.1 Scanning transmission electron microscopy

Scanning transmission electron microscopy allows imaging nanostructures at atomic resolution along with determination of their chemical composition. In a STEM a focused electron beam scans over the sample in a raster while the desired signal is collected to construct an image [133]. An advantage of STEM over TEM is the ability to operate simultaneously in different imaging modes including achievement of high sensitivity in Z-contrast. A range of different detectors provides collection not only of direct beams, but also scattered ones. Especially high-angle scattered electrons gathered by an annular dark-field detector allow improving the signal collection efficiency and giving less uncertainty about the size and shape of an investigating object. The contrast in each point of the images is dependent on the average atomic number along the electron beam path inside the sample. Defects of crystal lattice, such as extended dislocations, domains of the different crystal orientation can be directly seen in the image as irregularities of the lattice pattern. Although the defects of small size (atom vacancies and interstitials) usually cannot be observed because too weak perturbation produced by the electron beam. A drawback of TEM techniques is related to sample preparation, which is time-consuming and locally destroys samples when they are being thinned down to achieve electron transparency. As discussed in chapter 4, thin lamellas in plan-view geometry can be prepared by FIB milling, which introduces considerable damage into III-V semiconductors. An alternative option for specimen preparation could be the use of electron beam lithography followed by wet etching to produce needle-shaped specimens. The attempts to fabricate these samples have so far been unsuccessful. The goal of the further described measurements is the investigation of selectively grown material developed in this thesis.

The chosen sample consisted of lattice-matched InP/InGaAs/InP layers selectively grown on an InP:S wafer. Prior to deposition, the substrate with the HSQ mask was etched in-situ by CBr_4 inside the MOVPE reactor (see section 3.3). The specimens were prepared by FIB milling, then lifted out followed by a gentle Ar milling in the Fischione 1040 Nanomill. STEM analysis was performed on a less than 100 nm thin lamella in the direction perpendicular to the mask [0-11]. In addition, EDS analysis was conducted.

Figure 5.1 illustrates HAADF STEM pictures of epitaxially grown InP/InGaAs/InP, whereas InGaAs layer appears brighter than the InP matrix. Both high-resolution and low-resolution images revealed the non-uniform thickness of InGaAs over the layer becoming wider towards edges. Specifically, the middle part of the structure consists of ~16 ML while on sides its ~21 ML[7]. This non-uniformity is assumed to come from the fact that various incorporation rates are observed on the different crystallographic planes developed after in-situ etching (see section 3.3.1). Moreover, the profile possesses a symmetrical shape around the central vertical line that is another evidence of involvement of various crystallographic planes. Due to complicated shape of the structure, it is challenging to resolve specific planes involved in growth. However, the angle measurements using a graphic software could define {100} and {311}B planes. Additionally, the border between the InP:S wafer and the epitaxially grown InP layer is clearly seen that allows to observe the trench shape after etching.

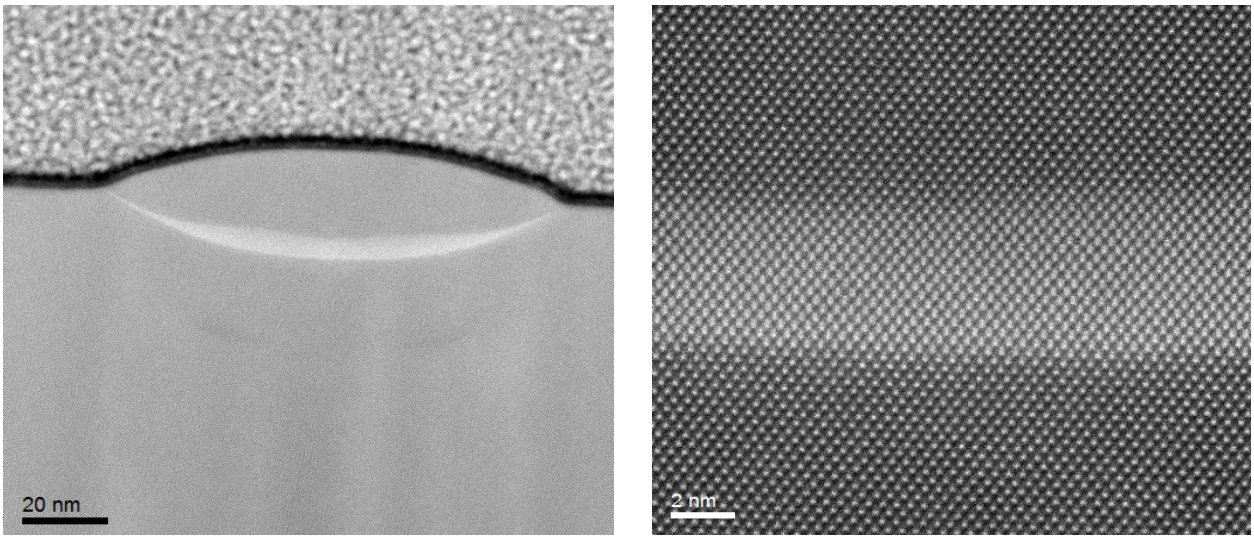

(a) (b)

Figure 5.1: STEM low magnification (a) and high magnification (b) images of an InGaAs/InP QW. The vertical white lines in the left figure are the curtaining effect from FIB and nanomill preparation.

EDS analysis revealed InAsP thin layer of around 3-4 nm underneath of the QW as discussed by other authors [134]–[136]. Along the InGaAs layer the composition is changed from

[7] Here sides refers to the thick middle part of the InGaAs layer as the right part in figure 5.1 (b), not the thin layer on sidewalls

$In_{0.65}Ga_{0.35}As_{0.87}P_{0.13}$ in the central part to $In_{0.75}Ga_{0.25}As_{0.77}P_{0.23}$ on the sides. Gallium, therefore, incorporates better on the {100} plane than on {311}B plane.

Another investigation was performed on the InGaAs directly grown after in-situ etching. An interesting aspect was to check the absence of dislocations, since the In content of InGaAs can increase significantly and lead to dislocation formation [31]. This experiment was conducted on the 250 nm wide opening oriented along the [0-1-1] direction which has two regions of InGaAs separated by InP (see section 3.4). The InGaAs is mostly grown on {311}B spreading partially on {111}B and {100} planes (figure 5.2 (a)). Indium content is smaller on {311}B planes increasing toward {111}B and {001} surfaces (see figure 5.2 (b)), and no dislocations are observed on the interface.

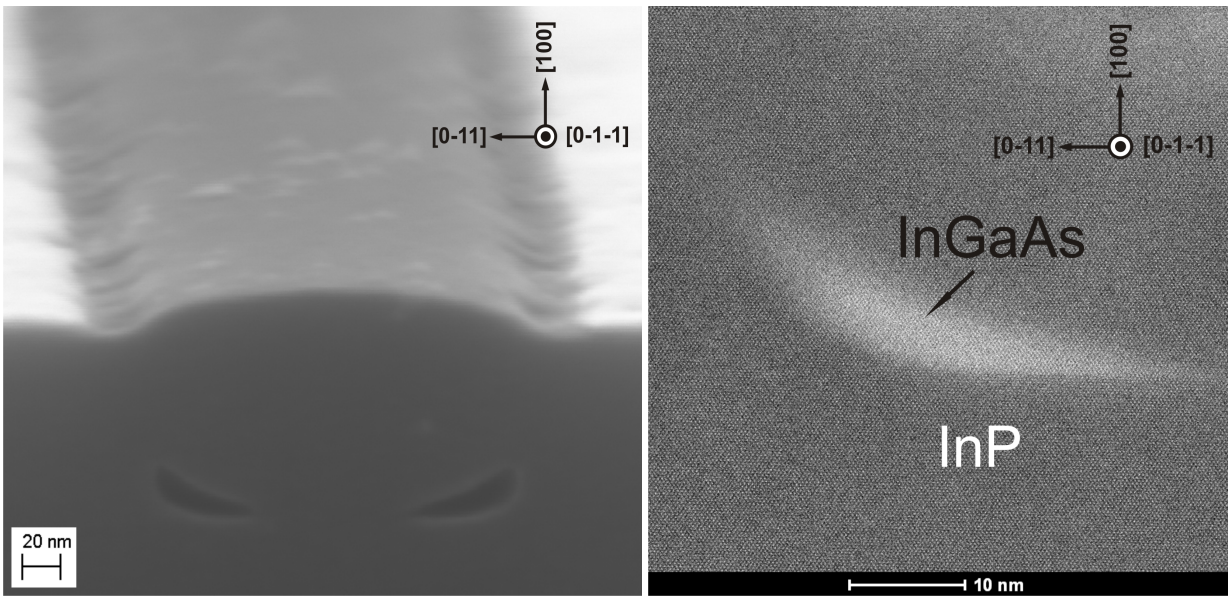

(a) (b)

Figure 5.2: STEM (a) and SEM (b) images of the 250 nm opening

Despite the possibility to investigate compositional structures and image on the atomic level, STEM analysis requires destructive and time-consuming sample preparation. Therefore, alternative approaches may be applied to investigate selectively grown structures, such as photoluminescence or cathodoluminescence, hence the latter is presented in the next section.

5.2 Cathodoluminescence

Cathodoluminescence (CL) method allows careful analysis of heterointerfaces in quantum well structures with atomic-scale fluctuations [137]. Under electron bombardment samples can exhibit cathodoluminescence that reveals properties of semiconductors, such as a band structure, defect states and quantum states of confined structures. However, the spatial limitation of this technique is due to migration of the injected charges, which need to be considered in data analysis.

CL measurements were carried out at the Technical University of Berlin (Germany), in the group headed by Prof. Dr. Stephan Reitzenstein. The used setup is based on a modified commercial scanning electron microscope Jeol JSM840 [138]. Presence of a cryostat with a He continuous flow makes possible to measure samples in a temperature range of 5-300 K. The depth of information, where signal comes from (or electron penetration), and lateral resolution are adjusted via variation of an acceleration voltage in an available range of 0.5-40 kV. The experiment was conducted under 1 nA current and 7 kV voltage, which corresponds to the penetration depth for electrons ~1 μm. The emission was collected using a cryogenically cooled InGaAs linear array. Integration time, the slit width and grating of the spectrometer were 5 s, 200 μm and 150 respectively. The pattern widths were 1 μm and 4 μm and the opening sizes were varied in a range of 100-500 nm in 100 nm increments. The SAG InP/InGaAs/InP layers, whose the fabrication process is described in section 3.4, were investigated.

As a reference, the spectrum of an unperturbated SQW was taken at He and room temperatures. The wavelength peaks was centered around 1465 nm and consists of four peaks. Multi-peaks can originate from not optimal growth conditions leading either to formation of InAsP layer (see appendix B) or non-uniform thickness of the QW. The difference in peak intensities of spectra taken at He and room temperatures was small (475 and 610 a.u. respectively). This slight difference takes place due to either lack of carries, which come from the matrix, or because not all carries recombine.

To investigate the selectively grown structures, first the openings with 1 μm protection lines were measured. The spectra of 500 nm and 400 nm openings along the [0-1-1] direction possess four peaks (at 1374 nm, 1454 nm, 1496 nm, and 1520 nm) (figure 5.3 (a)), which can be associated with different thicknesses of QW along the vertical interface. Thereby, in figure 5.3 (b) a scanning electron microscopy (SEM) image of the cross-sectional geometry demonstrates a variation of the thickness of the selectively grown InGaAs layer. It is difficult to observe the expected bandgap shift with temperature decrease. The red-shift of the bandgap perhaps is compensated by thermal occupation of higher energy states for higher sample temperature. Alternatively, the signal intensity at room temperature is extremely low and the wavelength peak is close to the InGaAs cut-off; thereby the wavelength peak could be located at the longer wavelength. Importantly, the QW grown in the 200 nm opening represents an array of small hills with altering wavelength in the range of 68 nm. The hills are believed to appear due to not optimized exposure conditions leading to left partial residual layer.

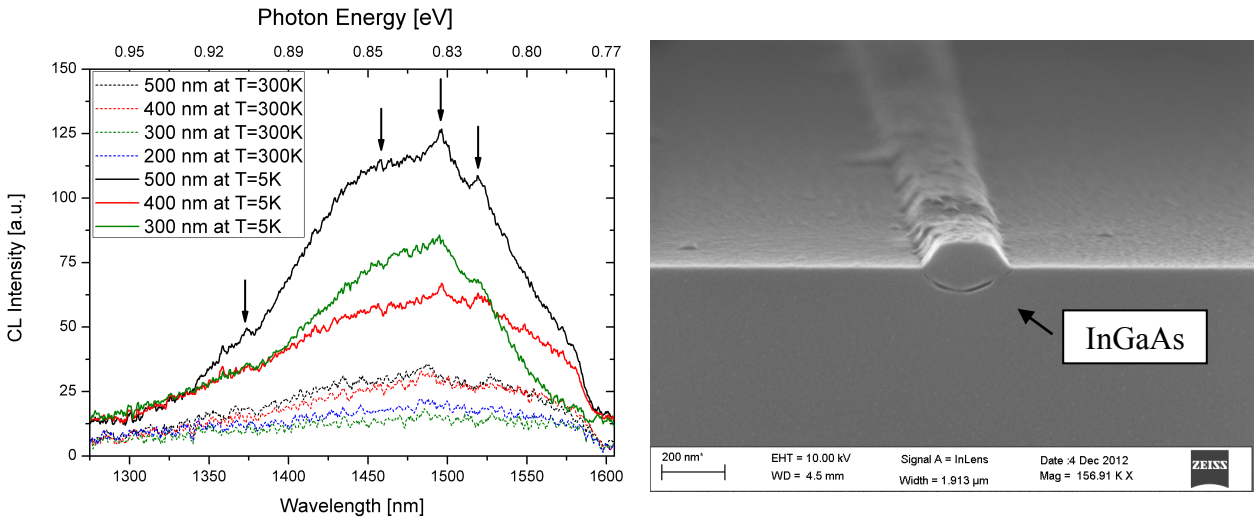

(a) (b)

Figure 5.3: SEM image of cross-section geometry and CL spectra of different width of selective area grown material with 1 µm protection line along [0-1-1] taken at 5 K (b)

For another crystallographic direction and wider protection lines no clear dependences has been identified. The difference in the intensity of the signal was observed to be small for low energies at He and room temperatures. For 500 nm and 400 nm widths for 4 µm mask width, the triplets were observed and the extracted peaks are 1449 nm, 1486 nm and 1530 nm. Due to the low signal intensity, the spatial mapping of the luminescence properties has not been done.

5.3 Photoluminescence

Photoluminescence spectroscopy is a powerful technique for study the quality of the semiconductor structures along with understanding of recombination mechanisms occurring in them [139]. PL is applied for quantifying the efficiency of optical emission and alloy composition. Two effects can be considered to have influence on the emission of a single SAG QW compared to unperturbated one far away from the mask. As already mentioned in section 2.3, surface kinetic limitation on the masked regions leads to lateral diffusion of the precursors to the uncovered semiconductor areas. Therefore, the growth enhancement in the open regions manifests itself in a red shift of the emission wavelength. In addition, the growth rate of group-III elements is different around the mask, as a result, the alloy composition perturbates. In the case of InGaAs, the effective diffusion length of TMIn precursors and desorption coefficient are smaller in comparison to TMGa. Thus, the In concentration is higher in the selectively grown heterostructure, which causes an additional red-shift of the wavelength. Furthermore, the sticking coefficients of Ga and In atoms are different on different crystallographic planes, so in-plane composition modulation occurs as well. A confocal micro-photoluminescence (µPL) setup, which is described in the following section, was used to evaluate the optical quality of the SAG material.

5.3.1 Experimental setup

The confocal micro-PL setup employed in this work was built at DTU Fotonik by Martin Schubert [132]. It permits measurements on an area of just a few µm as well as the possibility to resolve weak signals that are essential when working with nano-area selective material.
A schematic illustration of the setup is presented in figure 5.4. To pump the samples, the light source chosen was a laser diode emitting at 980 nm under continuous wave (CW) mode with a maximum output power of 300 mW. Varying the driver current can alter the output power of the laser diode. The pump source is coupled by a fiber into the setup. The light coupled out of the fiber is collected by an objective (Olympus) with a low numerical aperture. The beam is then expanded using two positive lenses, which play a role of a Keplerian beam expander. This is done to guarantee that the beam fills out the input aperture of the objective (FWHM=5 mm). Following the purple lines further, a combination of two half-wave plates (HWP) and a polarizing beam splitter allows to precisely adjust the pump power. Another way to tune the power is by using a rotating wheel with six filters.

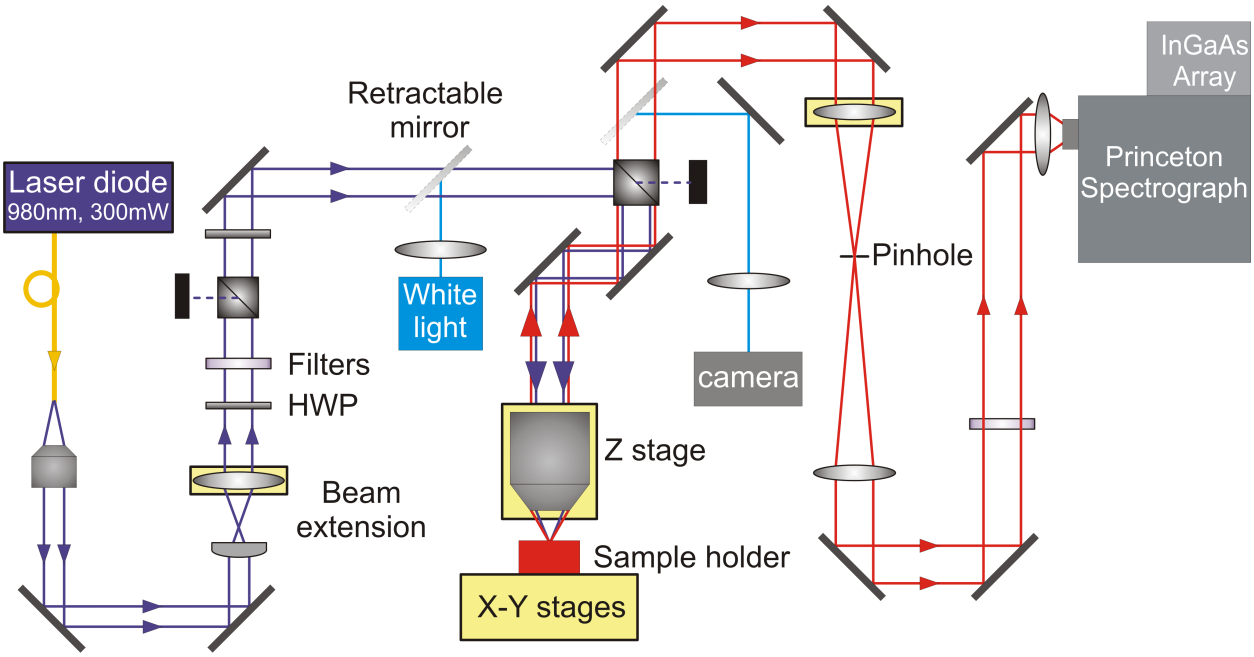

Figure 5.4: A schematic of the micro-Pl setup. The color scheme is the following: purple lines indicate the excitation beam rays, red lines are emitted light, and the blue ones are the white light to visualize the samples, additionally, the orange line shows the fiber and yellow boxes depict the adjustable mounts.

A mirror on a flip mount is used to switch between the excitation and visualization of the samples. The pellicle beam splitter is placed onwards to allocate in the same path the pumping and collecting beams. The beam splitter is put at 45 degrees angle to the incident beam. It transmits 92% of the incoming light and reflects 8% of it. Such configuration allows to collect a large fraction of the investigated emission.

The light is focused on the sample surface using a 50X Mitutoyo Plan Apo NIR HR Infinity-Corrected objective with a NA=0.65, a focal distance of 4 mm, and a working distance of 10 mm. To focus the beam, the objective is moved in the orthogonal direction to the sample surface by a z translation stage with a stepper motor. Although this objective is color corrected, the focus needs to be adjusted for the white light and the pumping spot separately. A sample is mounted on a piezo stage attached to a linear stage. The linear stage performs movements in a long range of 50 mm with an accuracy of less than 100 nm. It is mainly used for rough alignment. For precise positioning, the piezo stages with a movement range of 20 µm and an accuracy of 20 nm are employed. To find a position on the sample, a CCD camera is used together with a retractable mirror while the samples illuminated with a white light sources.

Light is spatially filtered by a combination of two achromatic lenses and a pinhole. Even though the resolution using the spatial selection with the pinhole is worse than the lateral resolution governed by the numerical aperture of the objective and the wavelength of the light, the selection help resolving weak signals by removing PL picked up outside the desired area. A rule of thumb here is that the spatial resolution equals the size of the pinhole divided by the objective magnification.

A long pass filter filters out the reflected light of the pump source. The light is then collected into a 500 mm Czerny-Turner spectrograph with a low-resolution grating of 300 lines per mm and blazed at 1000 nm. The spectrum is detected by using a cryogenically cooled InGaAs linear array. This type of detector covers the wavelength range from 0.8 µm to 1.7 µm; however, it is noisier for dark counts compared to Si detectors in the wavelength region where the sensitivity of both detectors overlaps.

5.3.2 Measurements of SAG InP/InGaAs/InP

To evaluate the influence of the growth mask parameters, the mask widths chosen were 1 µm and 4 µm with opening sizes varied in a series of steps (100, 125, 150, 200, 300, 400, 500 nm). The distance between two neighboring structures was 20 µm. The layer structure is InP/InGaAs/InP, whose fabrication process including shape profiles can be found in section 3.4. All surrounding material was etched away to prevent any additional signal to the optical spectra from the planar area. The measurements were done only at room temperature due to unavailable cryostat equipment at that time. The excitation photon energy is large than the InP bandgap, thereby the luminescence is observed only from the low band gap InGaAs QW. The excitation intensity was 31.2 kW/cm^2.

Prior to the investigation of the SAG structures, the PL spectrum of an unpatterned area (1 mm away from the selective structures) was measured having the peak wavelength located at 1401 nm, which corresponds to 4.1 nm of $In_{0.53}Ga_{0.47}As$ QW, and the line width FWHM=81.8 nm (51 meV). Figure 5.5 (a) shows the relationship between the wavelength and opening sizes along two crystallographic directions. Along the [0-1-1] direction, the bandgap decreases when the openings become smaller than 300 nm. Referring to the inset, the peak wavelength is located at the water absorption region, which prevents the exact determination of

the wavelengths of some structures. The thickness enhancement is more pronounced along the [0-1-1] direction, as evaluated by SEM measurement, resulted in the bigger wavelength shift for this direction s. When the mask is oriented along [0-11], the wavelength starts shifting at the smaller opening size of 300 nm. For the wider protection mask, the dependence has the same trend but the wavelength shifts to the longer region, which is associated with the increased growth enhancement proportional to the mask area.

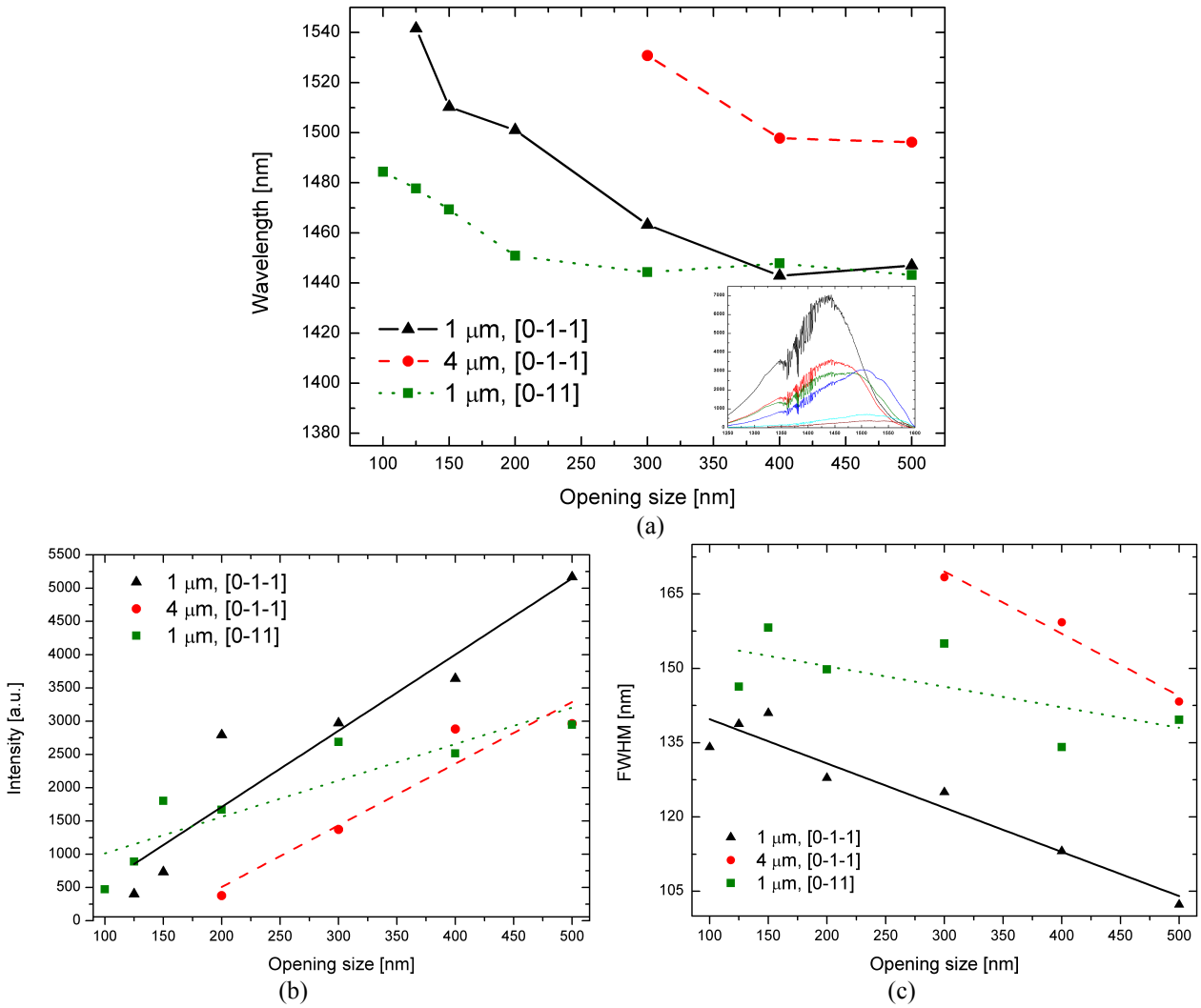

Figure 5.5: Wavelength (a), intensity (b) and FWHM (c) vs the opening sizes along the [0-1-1] and [0-11] crystallographic directions. The inset in the left figure shows PL spectra taken along the [0-1-1] direction.

Analyzing PL spectra one can, in principle, determine the composition of the epitaxial layer, however, the thickness of the layer needs to be known in advance. Since the effective thickness due to the growth enhancement is increased when the opening sizes are scaled down, it is difficult to make qualitative estimation of the wavelength shift. Moreover, an unpredictable intermixing of the elements on the lower heterointerface makes the estimation even more complicated [140]. However, considering the 125 nm opening investigated by STEM

(section 5.1), the calculated wavelength is 1512 nm (5 nm of $In_{0.65}Ga_{0.35}As_{0.87}P_{0.13}$ with barriers of $In_{0.75}Ga_{0.25}As_{0.77}P_{0.23}$). The difference in 29 nm can be seen when one compares the measured value of 1541 nm to the calculated one of 1518 nm.

Additionally the wavelength of the big openings (400 nm-500 nm) is not equal to the wavelength of the planar area. Therefore, the influence of the distance between neighboring structures [141] was investigated. The expansion in the separation distance results in a lower growth enhancement, due to the amount of material per unit area of the open surface. For example, an increase in a separation distance from 20 μm to 100 μm shifts the PL peak of big openings by 25 nm to a shorter wavelength under the same given conditions. Thus, the distance between selective features must be kept more than 100 μm to prevent the influence of the neighboring structures.

Even though the wavelength for the large openings does not vary much, the intensity changes linearly with a decrease of the opening sizes (figure 5.5 (b)). Along [0-1-1], the curve slop is similar for 1 μm and 4 μm wider protection lines, but the intensity of stripes with 1 μm lines is 1.75 times stronger than ones with 4 μm lines. For another direction, the curve slope is different in a way that the intensity is weaker for bigger than 300 nm openings and then becomes stronger. The emission line width (figure 5.5 (c)) is broader along the [0-11] direction, thus presumably the intermixing increases and the non-uniformity along the stripes leading to broader emission. The broadening is even bigger for wide protection lines, which believed due to rougher edges of the mask, which affects the width variation along the stripes.

Intuitively the openings on the submicron scale should not affect the optical properties in a significant way because some authors reported [35], [128] the diffusion length of TMIn and TMGa to be a few micrometers that leads to composition change. However, our experiments have showed that the intermixing and the large growth enhancement have a strong effect on the optical properties of an SAG InGaAs/InP QW even with few hundreds of nanometers in width.

5.3.3 Measurements of directly grown InGaAs/InP QW

Quantum structures grown in in-situ prepared V-shaped trenches potentially reduce the demands on precise control of the nanostructures due to their self-limited nature and on buffer layer growth [72]. By constructing the lateral potential of a QW to the size of 10 nm or even less, quantum confinement of carriers can be achieved in two dimensions.

5.3.4 Experimental setup

These μPL measurements were done at St. Petersburg Academic University in the group headed by Prof. A. Zhukov. The experimental setup is schematically illustrated in figure 5.6. The excitation source was a doubled Nd:YAG laser emiting at 532 nm working in CW mode. The excitation power was varied by the use of neutral density filters. Employing a pellicle beam splitter with a ratio of 8/92 (transmission/ reflection), the excitation and collection is established along the same path. By an Olympus LMPlan IR 100 NA=0.8 objective, the beam spot was

focused onto samples. The focused beam is scanned across the sample by the use of three piezo-stages with a movement accuracy of 20 nm. The signal was collected by a cryogenically cooled InGaAs detector (Horiba Symphony). Visualization of the structures was provided using a white light source and a CCD camera.

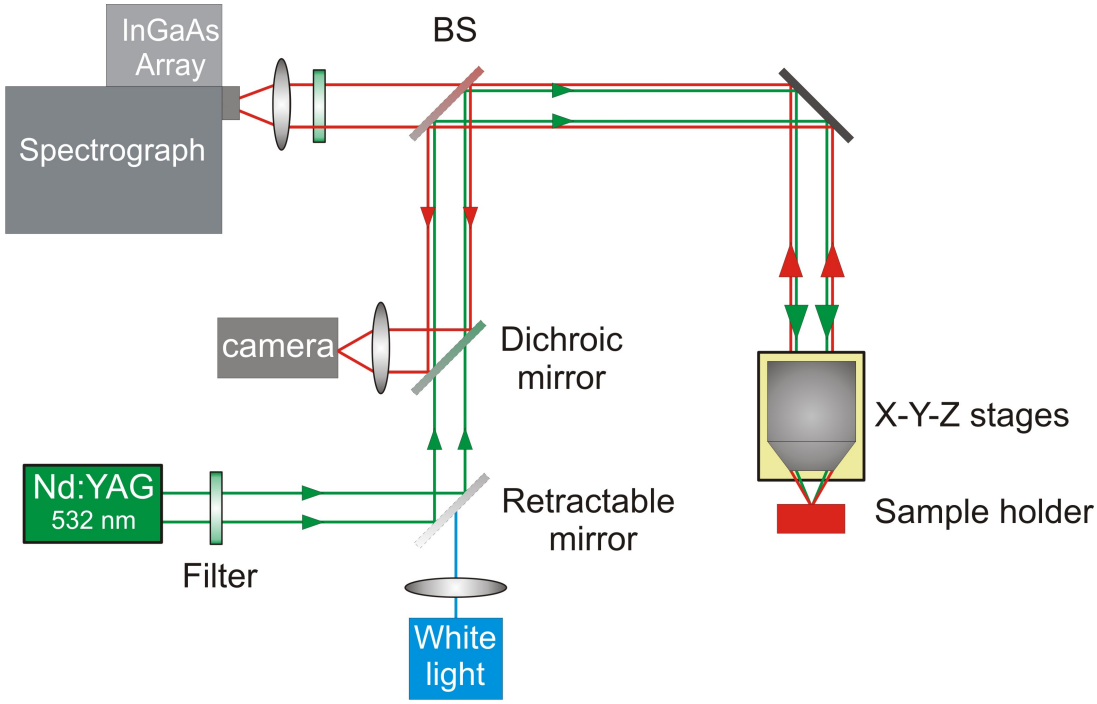

Figure 5.6: A schematic of the experimental setup.

In the current study, the optical properties of structures described in section 3.4.2 were investigated. As a reference the peak wavelength of the PL spectra take at room temperature from an unpatterned area were measured to be 1250 nm (FWHM=63 meV), which corresponds to 3.1 nm of $In_{0.53}Ga_{0.47}As/InP$ QW.

In the beginning, the selective area material was scanned across the mask to evaluate the wavelength and intensity changes. The strong signal with a wavelength of 1450 nm is located in a narrow range (figure 5.7). The intensity drops when the pumping position moves away from the central point, which proves the selectivity of the grown material. The extra stripes on the colormap are related to the water absorption lines.

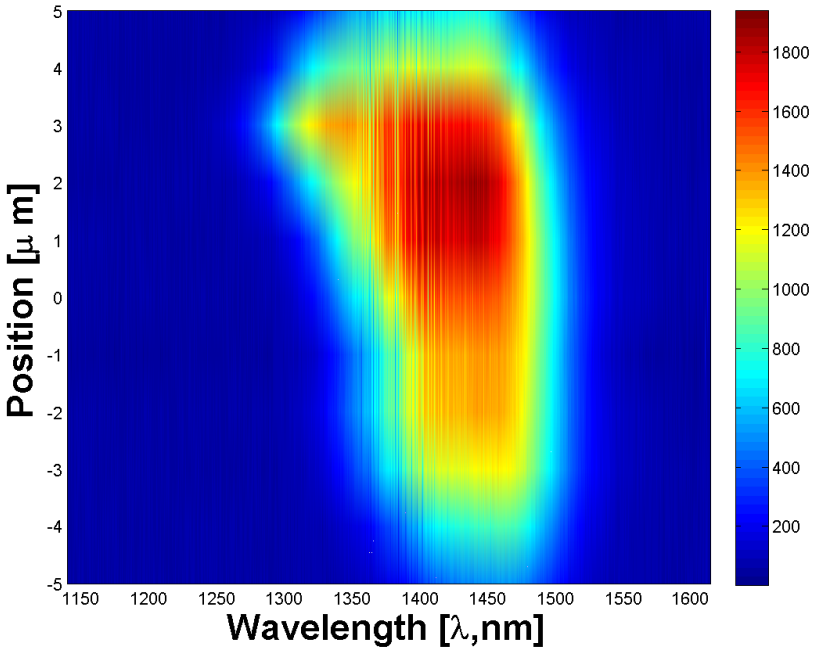

Figure 5.7: Colormap of selectively grown QW with the mask width of 4 μm and an opening size of 125 nm along [0-1-1] direction taken at 77 K and excitation power of 5.3 kW/cm^2

Along the [0-1-1] direction, PL spectra, which are displayed in figure 5.8 (a), show weaker emission intensity in comparison to the nanostructures in the perpendicular direction. Spectral broadening is approximately 175 nm (98 meV) and 120 nm (83 meV) along [0-1-1] and [0-11] directions, respectively. The 250 nm opening contains a doublet (see figure 5.2), which could be associated with the non-uniform thickness and the intermixing in the regions. The full spectrum is not observed due to the InGaAs detector cut-off. Spectra from the stripes along [0-1-1] revealed a red shift in over 125 nm contrasting with the stripes oriented in another way, as depicted in figure 5.8 (b)[8].

[8] Due to the lowest available grating of only 600 lines per mm the spectrum was assembled from multiple sub-spectra which affected the uniformity of the Gaussian lines.

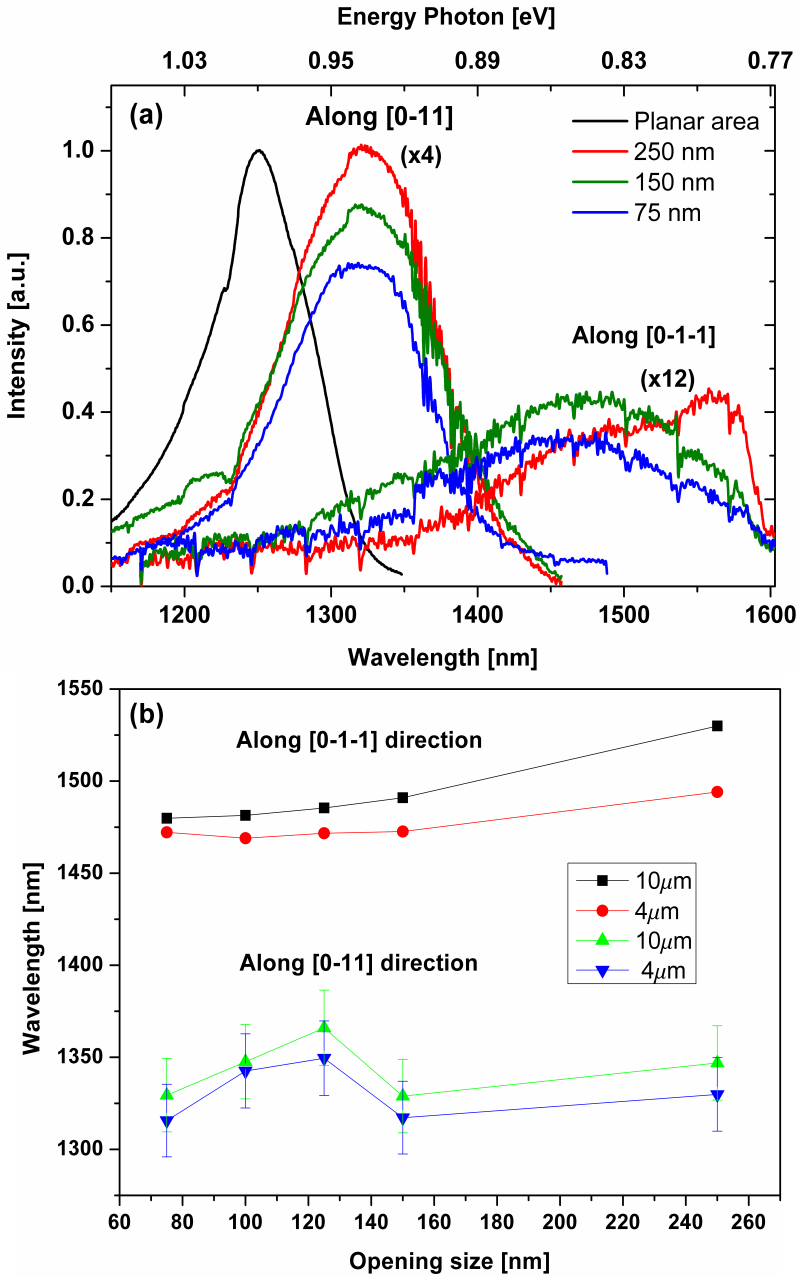

Figure 5.8: Room temperature PL spectra of the planar area and three selected openings (a), wavelength vs opening sizes of the selectively grown InGaAs/InP QW (b)

One challenge in the SEM observation is in precise measurements of thicknesses smaller than 10 nm, therefore, it was difficult to directly compare the growth enhancement for the two examined structures; however, qualitative estimation from the PL showed a higher growth enhancement along the [0-1-1] direction. As investigated in the work [30], different species exhibit distinct incorporation rate on different planes. A possible explanation for the InGaAs growth morphology is that the incorporation rate of Ga is higher on {311}A planes compared to combination of the {100} and {311}B planes. A not constant wavelength and intensity along the

ridges were observed for the [0-11] direction and is believed related to the non-uniform etched profile and mask collapse due to the large undercut (see section 3.4.2).

The experiments conducted with varying excitation power density did not reveal the saturation of the PL intensity due to the nonradiative recombination centers [142] even at the lowest used laser intensity of 4 kW/cm^2. Along [0-11], however, there was the saturation of the intensity when the excitation power was lower than 13 kW/cm^2. With an increase of the excitation power, the wavelength changes as expected due to the band filling effect.

5.4 Amplified spontaneous emission of PhC

Studying the Amplified Spontaneous Emission (ASE) of active PhC amplifiers can say a lot about physical aspects occurring in them. In brief, slow light enhancement can be identified from ASE spectra. Before discussing the measurements, the description of the experimental setup is presented in the next section.

5.4.1 Experimental setup

A schematic illustration of the setup for emission characterization of the fabricated devices is shown in figure 5.9. To pump the samples, a laser diode emitting at 980 nm was employed. This laser can be driven either in continuous mode with a maximum output power of 300 mW, or in pulsed mode. The chosen wavelength ensures efficient absorption of the pump wavelength by the active material. The pump power is either controlled using an attenuator or simply by changing driven current. The pumping light is collimated inside an Olympus microscope by employing a commercial collimation package (Thorlabs, F810FC-780). The sample is placed on a piezo-stage allowing precise alignment of the pumping beam to the desired region. The pumping beam is focused on the samples by an objective. In addition, by using a combination of two convex (f = 30 mm) lenses (not illustrated in the figure), the pump beam size can be changed to either a small spot or a wider area. Hence, the smallest pump spot achieved is ~ 2 μm diameter with a circular shape. The microscope contains a dichroic mirror and a beam splitter, which allow pumping the sample, collecting the light, and to visualizing the samples at the same time. In order to align and focus the pump beam onto a waveguide region or a laser cavity, the imaging is essential and is performed using an IR camera. The emission from the samples is collected through the same objective and detected by a cryogenically cooled InGaAs linear array. Alternatively, for the in-plane detection, a tapered fiber can be employed through a piezo-controlled positioner to collect light from the sample's facet.

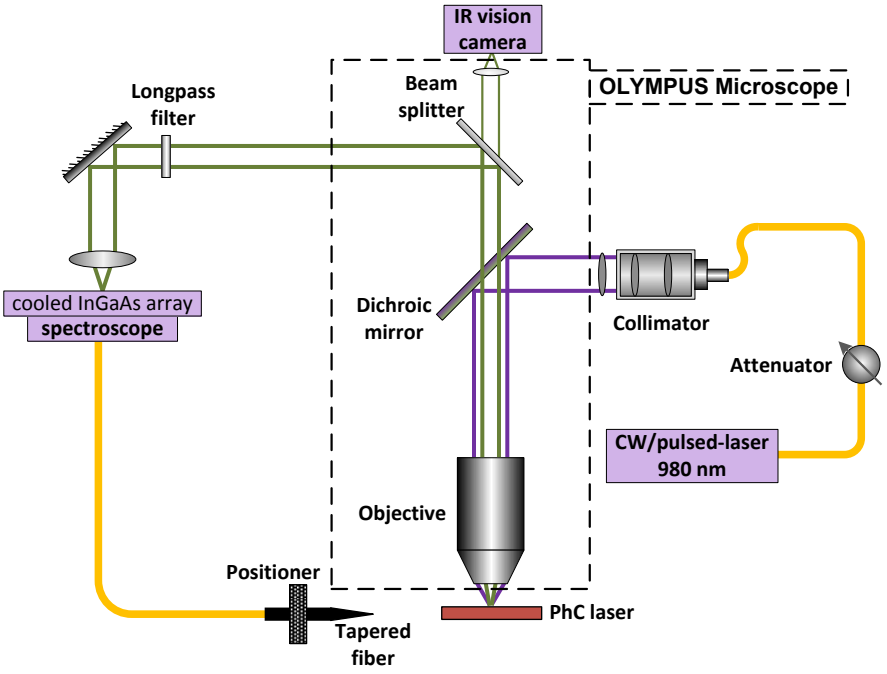

Figure 5.9: An illustration of the experimental setup. The yellow solid lines represent single mode fibers. The purple lines indicate the pumping beam rays and the green lines, the emission from the investigated samples. *Figure by courtesy of Weiqi Xue*

5.4.2 PhC waveguides

PhC waveguides with a missing row of holes (W1 type) were formed in an InP air-suspended membrane with a triangular lattice of air holes. A selectively grown InGaAs/InP quantum well was incorporated in the middle of the membrane. The material was grown in U-shaped trenches with a mask oriented along [0-1-1] direction (section 3.4). As discussed in section 4.4, integration of SAG into PhC membrane requires precise alignment of e-beam patterns. Take, for example, the active material of 200 nm in width and estimating the waveguide width of 400 nm, and then the affordable error should be less than 100 nm.

Photonic crystals have a pronounced effect on the spontaneous emission of quantum wells. The fabricated samples contain a variation in the lattice constants and holes radii to check the fabrication tolerances and the tunability of the waveguides. Generally speaking, controlling the lattice constant is more robust approach comparing to holes radii variation. Figure 5.10 illustrates three different waveguides with varying photonic crystals lattices. The presented spectra were pumped with the power of 12 mW under CW mode and the in-plane emission was collected from the out-coupling taper. In agreement with theoretical prediction, the wavelength of the fundamental mode moves in the expected way when the PhC parameters are altered, thereby the wavelength is blue shifted with the reduction of the lattice constant.

The waveguide in figure 5.10 denoted by a black line showed the strongest interaction between the photonic crystal and the active material while the other two waveguides have weaker enhancement (a red and blue line). The enhancement for the WG working at 1540 nm

had fourfold increase in gain compared with the one at 1490 nm. Note that the total intensity depends on the actual SAG gain, which is modulated by the waveguide group index, so the SAG intrinsic gain varies with the wavelength. Additionally, the out-coupling and the quality with regards to the position of the SAG can differ among waveguides.

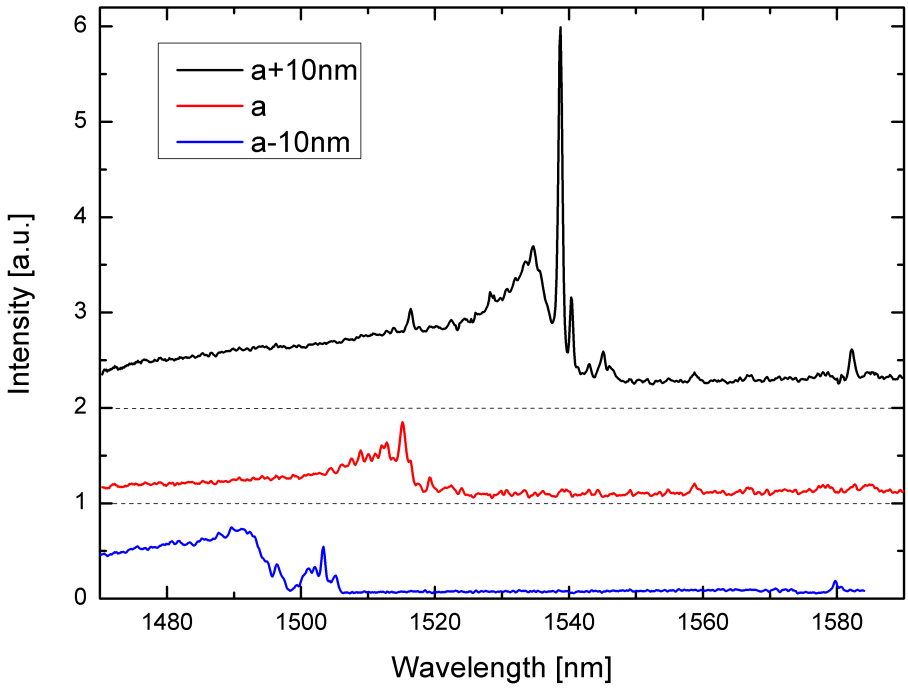

Figure 5.10: Spontaneous emission collected from the facet of three waveguides with various holes radii and lattice constants, where a=425 nm. Pump alignment and pump intensity are comparable for the given samples. An offset applies to the Y axis for clarity

A variation of the pumping power in a range of 1-12 mW revealed only a linear increase in the peaks intensity. In conclusion there were no lasing effect interfering with the measurements. If a laser forms, the relationship between the pump power and laser output is nonlinear. The waveguide working at 1540 nm was chosen for further investigation because, in the used setup, transmission measurements can be conducted only in a spectral range of 1530-1570 nm, which is a full usable wavelength range of the pump laser.

Moreover, the spectral shapes of the signals change as the smaller lattice constant the fewer peaks are accounting for the departing from the band edge. This was further investigated by checking the polarization as the emission from the PhC waveguides is polarization dependent. In graph presented above, the collected light contained both TE- and TM-modes. To distinguish between them, a polarizer is placed in front of the free-space coupled spectrometer. The peaks around 1540-1545 nm are TM-polarized modes (figure 5.11), not a part of the TE-fundamental mode. The band diagram indeed contains few TM modes closed to the fundamental mode. These modes are lossy and delocalized over the PhC, but can exhibit very large density of states due to their proximity to the TM band edge.

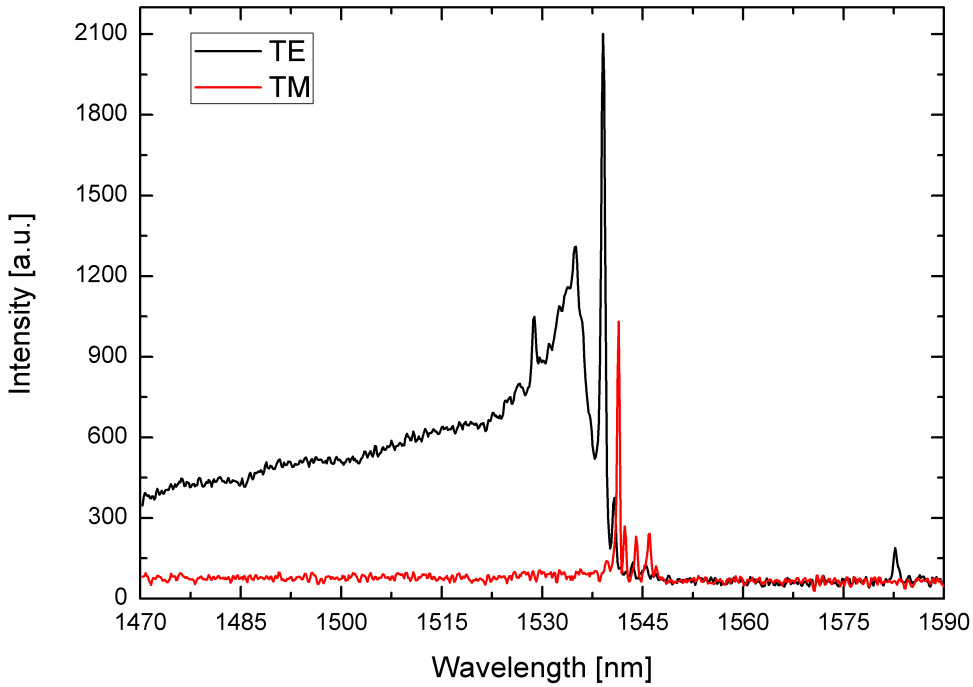

Figure 5.11: TE and TM emission of the PhC waveguide

In order to confirm the origin of the selectively grown active material, the collecting fiber was swiped across the edge of the photonic crystal waveguide. This technique is analogue to an unidimensional scanning near-field optical microscopy (SNOM) experiment with a coarse resolution of about 0.5µm. The different collected spectra are plotted in figure 5.12 as a colormap, hence showing the spectrum depending on the position on the PhC facet. The PhC waveguide extends in the y direction between -5µm to +5µm. When the fiber is outside of the PhC, a low intensity spectrum is seen corresponding to the wafer emission, with peak intensity around 1600 nm. When the fiber is moved across the PhC, a few discrete modes are seen. These modes are not strictly localized inside the waveguide and expand over the whole PhC structure: the mode at 1580 nm is a mode from the dielectric band, as confirmed by ab-initio computation of the PhC band diagram; the discrete modes around 1540 nm are associated to TM polarized modes. Finally, a strong photoluminescence signal ranging from below 1500 nm up to 1540 nm is only seen when the fiber is set precisely in front of the waveguide. The position and the wavelength range proved the emission from the SAG QW.

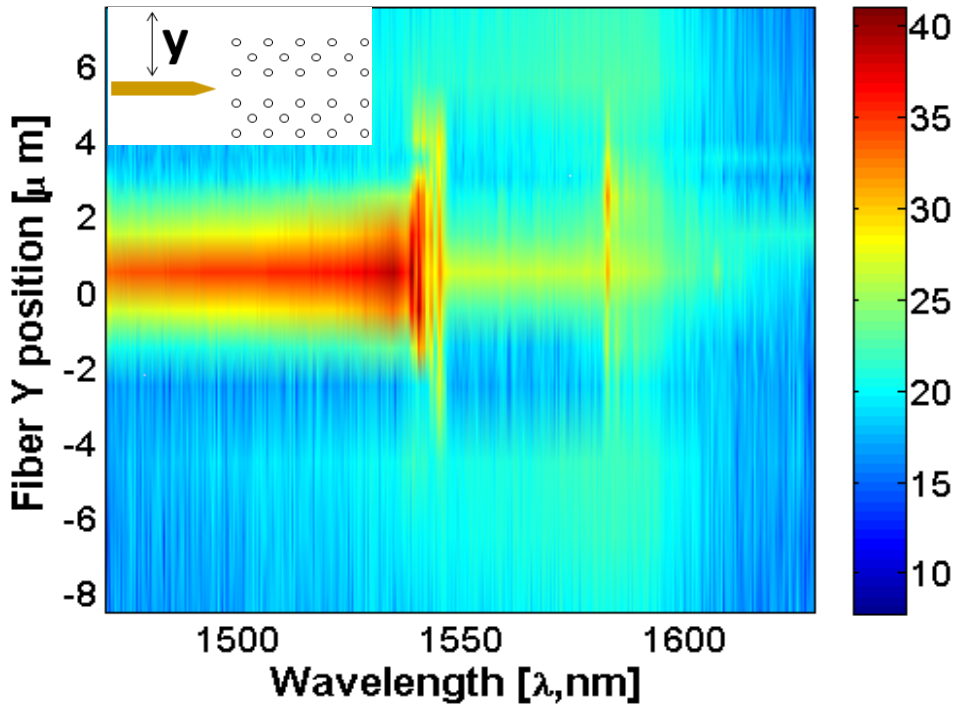

Figure 5.12: Colormap corresponding to the spectra recorded as the collecting fiber is swept across the photonic crystal edge (see inset). Both TE and TM polarization are collected. Colorscale: intensity in count/s, logarithmic scale.

The theoretical dispersion curve superimposed on the emission spectrum has been computed using the MPB [85] software with a resolution of N=30pts/a and the following parameters: a=415 nm, r/a=0.316, and h=340 nm (see figure 5.13). The intensity increases with the wavelength, as expected by theory. The slow light provides an enhancement of the photoluminescence proportional to the group index [143]. The computed group index is seen to match relatively well the emission spectrum up to group indices of 18, which is a reasonable value for a 900 μm long waveguide. Closer to the band edge, where the group index increases further, multiple scattering [144] and weak localization due to disorder disturb the ideal behavior. Owing to an imperfection blocking the light transmission at the output facet, it was unfortunately not possible to investigate the amplification capability of the waveguide and estimate the gain precisely.

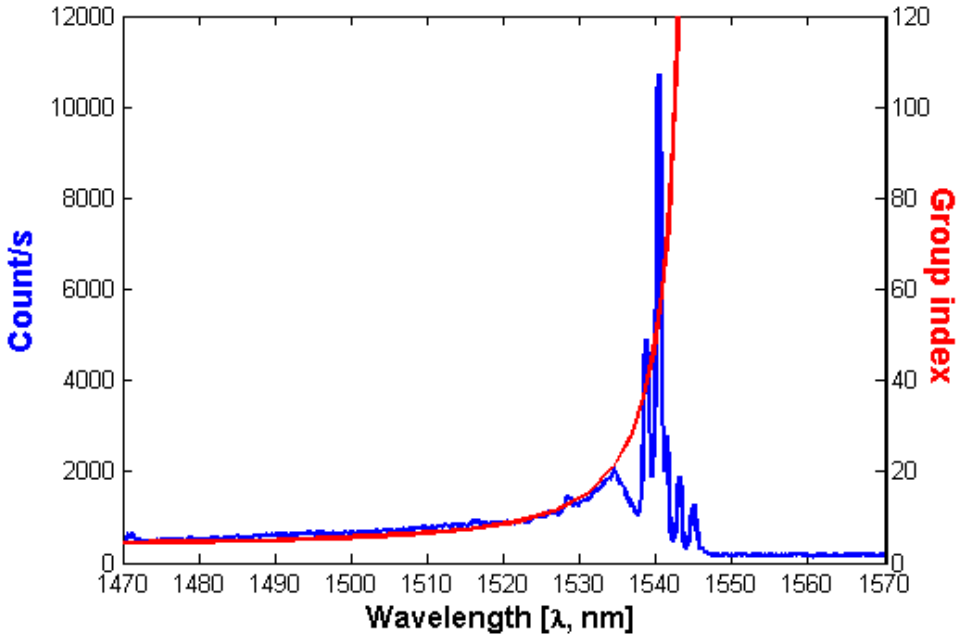

Figure 5.13: The theoretical waveguide's dispersion is shown, scaled by a factor 100, no offsets are applied.

For comparison figure 5.14 shows the measured spectra for other waveguides where the SAG material appears to be misaligned. The different polarizations are discriminated by a polarizer. The black curve is likely to be a TM-polarized mode. The red curve reminds the tale of the bulk InGaAs sacrificial layer emission. In addition, the samples did not exhibit the general variation of wavelength with PhC parameter changes. This indicates that the emission, therefore the active material, is not coupled to the PhC.

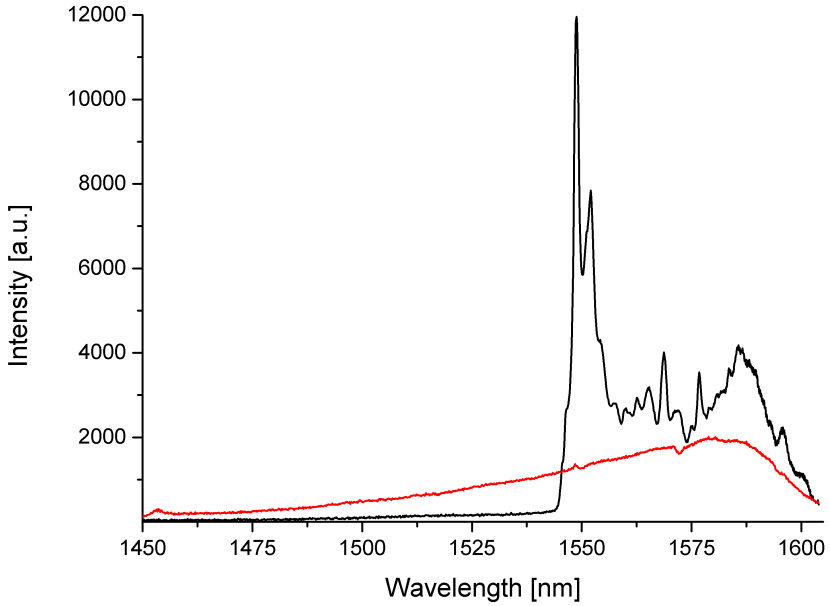

Figure 5.14: PL of photonic crystal waveguides with a single QW, where the material is misaligned within the PhC waveguide.

5.4.3 PhC lasers

The demonstration of compact lasers fulfilling the requirements of noise, speed and energy consumption for integrated photonic circuits in communications is of great interest. PhC slab lasers, therefore, are explored theoretically and experimentally by various groups around the world [145]–[148].

The SAG material was now incorporated in a long PhC cavity made by closing a PhC waveguide at each side by a supplementary reflecting mirror. The photonic crystal lasers were designed in eight different cavity lengths in a range of 5-40 μm in 5 μm increments. The cavity was formed by adding holes to both sides of the W1 type waveguide, 20 holes served as a completely reflective mirror and a single hole is used as an out-coupling mirror. The cavity is 5 μm away from the out-coupling taper (see figure 5.15).

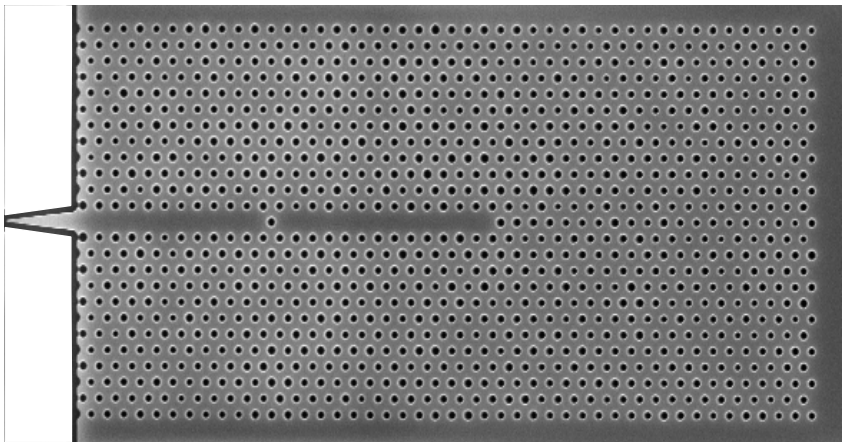

Figure 5.15: SEM image of the photonic crystal laser with one hole as an out-coupling mirror

The measurements were conducted by collecting the signal from the output facet terminated by inverted tapers and from the top plane. Neither type of measurements has revealed any lasing. The emission remains the spectrum depicted in figure 5.14 and is not believed to be associated with selective area QW into PhC lasers. In fact, sweeping the collecting fiber across the PhC facet, like done previously for the PhC amplifiers did not indicate any reasonable changes in the spectral or spatial positions of the emission. Moreover, when the PhC parameters were varied among the samples, the expected spectral shifts were not observed.

PhC lasers did not work in the expected way. So far, the reason for this has not been clearly understood. Prior to integration into the PhC platform, the wavelength of the SAG single QW was calibrated and the growth process went without errors. Moreover, relatively broad emission peak (FWHM > 100 nm) ensures overlap with photonic crystal band edge. The SAG QW test structures placed on the wafer were checked using SEM imaging and revealed the presence of the active material inside the waveguide area in both directions. Besides, the presence of working PhC waveguide amplifiers on the same wafer, as presented previously, indicates that both PhC design and SAG QW material are match in term of position and working wavelength. One hypothesis is the presence of a residual misalignment, especially along the waveguide direction.

This would not affect the PhC waveguide amplifier strongly owing to its long length, but could have a detrimental effect on the much shorter cavity.

Further investigations are necessary to fully understand the reason for the emission absence. For the further work, a selective material without photonic crystals and photonic crystal without an active material as reference structures need to be included into fabrication design.

5.5 Summary

Concluding this section, STEM analysis revealed an intermixing of the group V elements, especially, the composition of the intermixed InGaAsP is distinctive for different planes, on which growth is initiated. Non-uniformity in thickness was measured along the investigated structure being 5 ML. CL spectra contained multi-peaks, which are believed due to non-uniform thickness across the QW layer and InAsP formation on the lower heterointerface.

Photoluminecence measurements showed that the distance between neighboring structures smaller than hundreds of micrometers affects the wavelength of the SAG InGaAs/InP QW. When InP is deposited before the QW, the emission wavelength is dependent on the opening sizes. This dependence is distinctive along different crystallographic directions: the wavelength red-shift is stronger for the structures oriented along [0-1-1] direction and start been seen for the openings as big as 300 nm. This effect is explained by the intermixing of the components and the increased growth enhancement. In the case of a directly grown QW, room temperature micro-photoluminescence measurements indicated a wavelength red-shift in over 125 nm along [0-1-1] comparing to [0-11], which is related to both growth enhancement and composition variation of the grown material.

The successful integration of SAG QW into a photonic crystal structure has been reported. This demonstration involves (i) the control of the emission wavelength of the SAG QW, which matches the PhC operating wavelength; (ii) the precise alignment of the PhC waveguide with the active SAG QW. The ASE originates, indeed, from the PhC waveguide that was proved by a coarse SNOM experiment. The PhC waveguide showed a multiple-scattering free ASE spectra up to n_g=18. This performance could still be improved considering that the waveguide tested was a simple W1 waveguide, not dispersion-engineered.

PhC lasers made by the incorporation of SAG QW into a long PhC cavity were also studied without any lasing observed. The absence of a clear TE polarized ASE and the fact that the residual ASE is not confined inside the PhC cavity may indicate a problem related to the SAG QW. The principal hypothesis would be the presence of a residual misalignment between the active material and the PhC. That could have a minor effect on the PhC waveguide due to its long length but would be detrimental to the PhC cavity; further investigations are required.

Chapter 6. Conclusion and outlook

6.1 Conclusion

This work has developed active photonic crystals with selective area grown active medium. The ASE of such structures was measured indeed from the PhC waveguide as demonstrated by a coarse SNOM experiment. The expected trend of the dispersion with PhC parameter alteration was obtained with the strongest enhancement at 1540 nm. The PhC waveguide showed a multiple-scattering free ASE spectra up to n_g=18. Closer to the band edge, the ideal behavior was disturbed due multiple scattering and weak localization.

The fabrication process for SAG material involved the development of a scum free HSQ mask with openings of several tens/hundreds nm. The optimum parameters of the HSQ mask were XR1451-02 spun on 30 nm thickness, pre-baking 2 minutes at a temperature of 120 °C and 2 minutes at 220 °C, the electron dose of 4000 μC/cm^2 and the development condition is 90 s in 1 AZ400K: 2 H_2O at room temperature. The presence of the residual layer in the opening areas leads to a detrimental decrease in the PL signal. Thus, the mask quality plays an important role in the further epitaxial process.

Before performing MOVPE growth, etching of the native InP oxide in concentrated sulfuric acid, as a surface preparation step, revealed crystallographic dependent behavior. Sulfuric acid etches InP with etch rate of around 7 nm/min. Another observation was that the minimum time for native oxide etching followed by regrowth of an InGaAs/InP QW and identified by photoluminescence measurements was 2 minutes without a detrimentally decrease of the optical signal.

During in-situ CBr_4 etching, U-shaped grooves were formed along the [0-1-1] direction, terminated by {111}B planes with an ~15 nm {100} plateau and transitional{311}B planes, developed in a self-limiting manner. When the etch time is not enough to reach this profile, the trench possessed a trapezoidal shape with a combination of {100} and {311}B planes at the bottom. In the perpendicular direction [0-11], etching with a dominant lateral component driven by fast etched {111}A and {311}A side planes was observed. Undercutting was observed for both directions being larger for the mask oriented along [0-11]. Moreover, the etching enhancement was more pronounced for a wider mask.

In light of these results, the shape of a selectively grown InGaAs layer is dependent on crystallographic orientation of the mask as well as on the opening sizes. When an InP buffer layer is deposited the shape of InGaAs spreads differently across various opening widths: for 250 nm openings it reproduces the groove configuration, but for 100 nm openings the material is mostly located in the InP matrix. STEM analysis revealed an intermixing of the group V elements resulted in formation of $In_{(1-x)}Ga_xAs_{(1-x)}P_y$ with different compositions. A non-uniform

profile along the SAG structures was seen wherein the QW becomes thicker toward sidewalls. Photoluminecence measurements of SAG QWs with prior deposited InP showed wavelength dependence on the opening sizes and the width of protection lines. This dependence is distinctive along different crystallographic directions: the wavelength red-shift is stronger for the structures oriented along [0-1-1] direction and seen for openings as big as 300 nm. The current effect is explained by the intermixing of the components and the growth enhancement. In addition, the influence of the neighboring structures on the growth enhancement was detected, thus to the distance between structures has to be greater than 100 μm in order to not interfere with each other.

A directly grown single InGaAs QW in the etched grooves demonstrated different QW profiles: a crescent-shaped on {311}B and {100} planes (along the [0-1-1] direction) and two separated quarter-circle curvatures grown preferably on {311}A along [0-11]. Room temperature micro-photoluminescence measurements indicated a wavelength red-shift in over 125 nm along [0-1-1] comparing to [0-11], which is related to both growth enhancement and composition variation of the grown material.

With regards to incorporation of SAG material into InP slabs, the material was placed inside pillar-shaped specimens for imaging at high resolution. The fabrication error for alignment of two patterns was obtained 30 nm for needle-shaped specimens; however, for structures required additional overgrowth of InP, such as PhC devices, the misalignment value was 65 nm.

6.2 Outlook

The mask optimization has been done for the QW pattern while the mask for the QDs was left beyond of this study. A more advanced writing procedure is required to achieve an appropriate pattern, as discussed in the section 3.1.3.

The unfortunate drawback is that etching along different directions revealed distinctive trench' profiles. In addition, mask undercutting and the obtained shapes prevent further development of the present technology to grow multiple quantum wells. Therefore, the effect of etching temperature variation can be assessed [125] that could lead to various profiles. Another concept is to try different wafer orientation, such as InP(111)B wafers [149]. For further laser application, it is interesting to investigate SAG of other materials, such as InGaAsP and InGaAlAs.

For the needle-shaped specimens for TEM investigation, optimization of the glass layer to obtain its better quality is believed can improve the adhesion and protect the specimens during final wet-etched release of the sacrificial layer.

For the future experiments with photonic crystal lasers, the sacrificial layer can be changed to InAlAs, which has the wavelength of 0.86 μm. First, as shown by NTT, an InAlAs sacrificial layer decreases the leakage current through substrate [82]. Secondly, the PL signal can be measured directly after selective area growth to give the possibility to tailor PhC dispersion for better matching of working wavelength of PhC and SAG material.

Appendix A

Spin coating of HSQ

Ultrathin HSQ layers are interesting material for nanofabrication. By varying the diluting ratio of HSQ with a 4/methylpentan-2-one (MIBK) solution [110], the thickness of a spin-coated film can be altered, in particular decreased even to 13 nm. Therefore, various dilution rates of HSQ and spinning settings were tested. The results are presented in the table A.1.

Table A.1 Thickness of HSQ using different dilutions and spinning conditions

Type of resist	Prespeed	Preacceleration	Speed	Acceleration	Thickness [nm]
XR1451-06	500	100	1000	1000	253
XR1451-06	0	0	4000	4000	94
1:2 XR1451-06:MIBK	0	0	4000	4000	40
1:4 XR1451-06:MIBK	500	100	4000	4000	127
1:4 XR1451-06:MIBK	0	0	4000	4000	30
1:9 XR1451-06:MIBK	500	100	4000	4000	78
1:9 XR1451-06:MIBK	0	0	4000	4000	25
1:10 XR1451-06:MIBK	0	0	1000	1000	25
1:10 XR1451-06:MIBK	0	0	4000	4000	13

The spin coating was done with a closed lid. The thickness was measured by ellipsometer (WVASE). The curves were fitted using Cauchy model. As seen, the prespin raises the thickness almost in three times. When the prespin does not apply, the obtained thicknesses follows the spin curve obtained from Dow Corning for XR1451 resist [150].

Appendix B

Optimization of InP/InGaAs/InP interface

The quality of the InGaAs/InP interfaces strongly depends on the gas switching sequence during MOVPE growth. Deposition of InGaAs on InP and vice versa requires exchange of two elements, thus to obtain abrupt interfaces growth interruption need to be included in the growth procedure. An intermixing of elements at the upper and lower heterojunction can occur, especially after growth of InGaAs layer, As atoms can incorporate into InP and form InAsP interlayer. Obtained in this way graded interface InGaAs-InAsP-InP increases the effective thickness of the quantum well and manifests in the red-shift of the wavelength. Furthermore, at the lower interface P can incorporate into InGaAs to form InGaAsP, which lowers the emission energy. As reported [134]–[136], the optimal parameters are individual for each growth reactor and can vary significantly.
The experiment was conducted on a (001) InP:Fe wafer with a 500 nm epitaxially grown buffer layer without any selective mask. Three samples were grown with various growth procedures. For the sample A, the layer stack including the sequence of gas exchange is shown in table B.1. A single quantum well InGaAs/InP lattice matched to InP had a nominal thickness of 6.5 nm. In the case of sample B, the AsH_3 phase after InGaAs layer (step #7 in the table B.1) was removed. Sample C was grown without CBr_4 etching (step #2 was removed) to test the influence of this step on the optical properties.

Table B.1 Gas switching sequence

	Material	Start	Start	Thickness	Time	Flow	Comments
No		**(x)**	**(y)**	**(nm)**	**sec**	**sccm**	
9	InP			13	40.01	350/200	
8	PH_3				1	200	
7	AsH_3				1	175	
6	InGaAs			6.5	4.6	350/14.72/200	
5	AsH_3				1	175	
4	InP			5	9.09	350/200	
3	PH_3				1	200	
2	CB_4 etching			40	183.4	115.71	with 200 sccm PH_3
1	InP buffer			500			
Sub	**InP:Fe**			$350*10^3$			

Before the measurements at low temperature, mapping of the entire wafer at RT and with 980 nm excitation wavelength showed non-uniformity in the intensity and FWHM distribution of 50% and 10%, respectively. Photoluminescence spectra taken at 77K are presented in figure B.1 and the values are extracted in the table B.2. The calculated wavelength of the QW with the abrupt interfaces was 1399 nm, thereby the grown alloy composition was In-rich. Another explanation is non-uniform growth rates at the beginning of the deposition. When the AsH_3 phase is removed from the growth procedure, the optical properties are deteriorated (sample B). Only a small red-shift of 2 nm is observed, but intensity dropped and the line width increased. A non-abrupt InGaAs quantum well can be described by adding 1 ML of $In_{0.53}Ga_{0.47}AsP$ to the lower interface and 1 ML of InAsP to the upper interface [136].
During CBr_4 etching carbon can be embedded in a sufficient amount into layers and such strong doping can broad luminescence features. Comparing the samples A and C allows speculate that CBr_4 improves the etched surface quality as a rough interface deteriorates the optical signal. Even the Sample A has a broader peak but it can be related to FWHM gradient on the wafer.

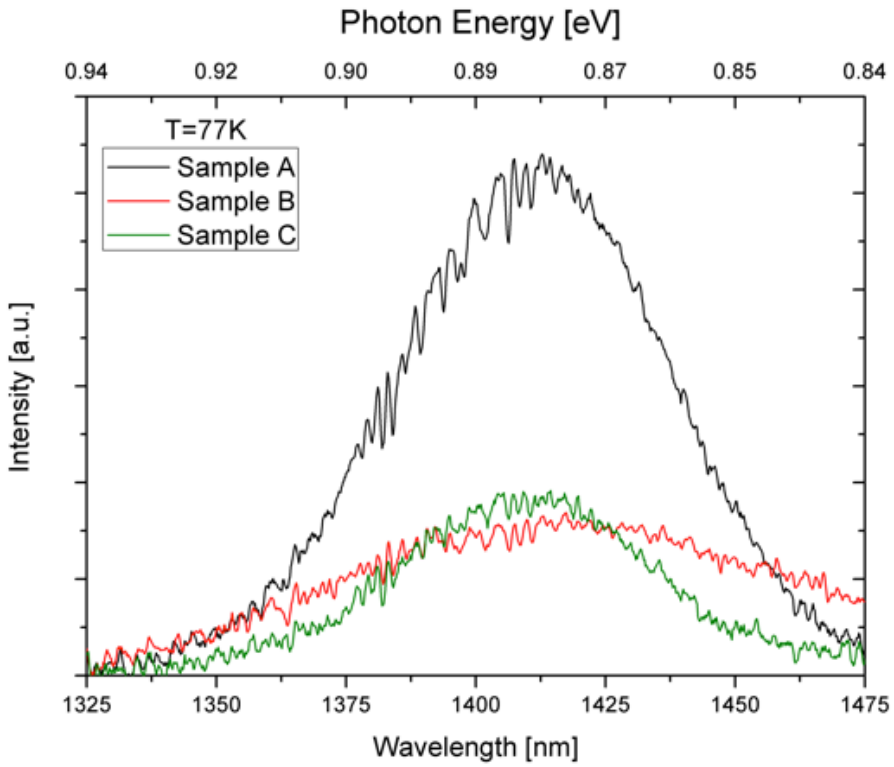

Figure B.1: PL spectra taken at 77K with excitation power of 1 mW

Table B.2 Comparison of PL spectra of the investigated wafers

Sample	Wavelength, nm	FWHM, nm	Intensity, a.u.
Sample A	1414.3	58.7	553
Sample B	1416.9	87.3	175.5
Sample C	1409.3	51.7	205

List of Abbreviations

ASE	Amplified spontaneous emission
CL	Cathodoluminescence
ClVPE	Chloride vapor phase epitaxy
CW	Continuous Wave
DFB	Distributed Feedback
DI water	Deionized water
DOS	Density of state
EDS	Energy dispersive X-ray spectroscopy
FDTD	Finite-Difference Time-Domain
FWHM	Full width at half maximum
HVPE	Hydride vapor phase epitaxy
HSQ	Hydrogen silsesquioxane
ICP	Inductive coupled plasma
LEAP	Lambda-scale embedded active region photonic crystal
LED	Light emitting diode
LPE	Liquid phase epitaxy
MBE	Molecular beam epitaxy
MIBK	4/methylpentan-2-one
MOVPE	Metal-organic vapor phase epitaxy
MPB	Massachusetts Institute of Technology bandgap package
NOC	Network-on-chip
NTT	Nippon Telegraph and Telephone Corporation
PBG	Photonic band gap
PECVD	Plasma enhanced chemical vapor deposition
PhC	Photonic crystal
PL	Photoluminescence
QD	Quantum dot
QW	Quantum well
QWire	Quantum wire
RDR	Rotating disk reactor
RF	Radio frequency
RIE	Reactive ion ething
RHEED	Reflection of high-energy electron diffraction
SAG	Selective area growth
SEM	Scanning electron microscopy

STEM	Scanning transmission electron microscopy
TEM	Transmission electron microscopy
TE	Transverse electric
TIR	Total internal reflection
TM	Transverse magnetic
VCSEL	Vertical cavity surface-emitting lasers

Materials

GaAs	Gallium Arsenide
InP	Indium Phosphide
InGaAsP	Indium Gallium Arsenide Phosphide
InGaAlAs	Indium Gallium Aluminium Arsenide

Reagents

CH_4	Methane
CHF_3	Fluoroform
CF_4	Carbon tetrafluoride
HCl	Hydrochloric acid
IPA	Isopropyl alcohol
HF	Hydrofluoric acid
H_3PO_4	Phosphoric acid
H_2SO_4	Sulphuric acid
N_2O	Nitrous oxide
SiH_4	Silan
Si_3N_4	Silicon nitride

Bibliography

[1] E. B. Desurvire, “Capacity Demand and Technology Challenges for Lightwave Systems in the Next Two Decades,” *J. Light. Technol.*, vol. 24, no. 12, pp. 4697–4710, Dec. 2006.

[2] D. A. B. Miller, “Rationale and challenges for optical interconnects to electronic chips,” *Proc. IEEE*, vol. 88, no. 25, pp. 728–749, Sep. 2000.

[3] D. A. B. Miller, “Physical reasons for optical interconnection,” *Int. J. Optoelectron.*, vol. 168, 1997.

[4] D. A. B. Miller, “Device requirements for optical interconnects to silicon chips,” *Proc. IEEE*, vol. 97, pp. 1166–1185, Jul. 2009.

[5] M. Smit, J. van der Tol, and M. Hill, “Moore’s law in photonics,” *Laser Photon. Rev.*, vol. 6, no. 1, pp. 1–13, Jan. 2012.

[6] T. Baba, “Remember the light,” *Nature*, vol. 1, 2007.

[7] Lord Rayleigh, “On the Maintenance of Vibrations by Forces of Double Frequency, and on the Propagation of Waves Through a Medium Endowed with a Periodic Structure,” *Philosopical Mag. J. Sci.*, vol. 24, no. 147, pp. 145–159, 1887.

[8] E. Yablonovitch, “Inhibited spontaneous emission in solid-state physics and electronics,” *Phys. Rev. Lett.*, vol. 58, no. 20, pp. 2059–2062, 1987.

[9] S. John, “Electromagnetic absorption in a disordered medium near a photon mobility edge,” *Phys. Rev. Lett.*, vol. 53, no. 22, pp. 2169–2172, 1984.

[10] E. Yablonovitch, “Photonic crystals: semiconductors of light,” *Sci. Am.*, vol. December 2, pp. 47–55, 2001.

[11] J. Sanders, “Microstructure and crystallinity of gem opals,” *Am. Mineral.*, vol. 60, pp. 749–757, 1975.

[12] J. Zi, X. Yu, Y. Li, X. Hu, C. Xu, X. Wang, X. Liu, and R. Fu, “Coloration strategies in peacock feathers.,” *Proc. Natl. Acad. Sci. U. S. A.*, vol. 100, no. 22, pp. 12576–8, Oct. 2003.

[13] L. Biró, Z. Bálint, K. Kertész, Z. Vértesy, G. Márk, Z. Horváth, J. Balázs, D. Méhn, I. Kiricsi, V. Lousse, and J.-P. Vigneron, “Role of photonic-crystal-type structures in the

thermal regulation of a Lycaenid butterfly sister species pair," *Phys. Rev. E*, vol. 67, no. 2, p. 021907, Feb. 2003.

[14] K. Ishizaki, M. Koumura, K. Suzuki, K. Gondaira, and S. Noda, "Realization of three-dimensional guiding of photons in photonic crystals," *Nat. Photonics*, vol. 7, pp. 133–137, 2013.

[15] S. a. Rinne, F. García-Santamaría, and P. V. Braun, "Embedded cavities and waveguides in three-dimensional silicon photonic crystals," *Nat. Photonics*, vol. 2, no. January, pp. 52–56, 2008.

[16] K. Suzuki, K. Kitano, K. Ishizaki, and S. Noda, "Three-dimensional photonic crystals created by single-step multi-directional plasma etching," *Opt. Express*, vol. 22, no. 14, pp. 17099–117106, 2014.

[17] H. M. Yates, M. E. Pemble, H. Míguez, a. Blanco, C. López, F. Meseguer, and L. Vázquez, "Atmospheric pressure MOCVD growth of crystalline InP in opals," *J. Cryst. Growth*, vol. 193, pp. 9–15, 1998.

[18] S. Noda, "Full Three-Dimensional Photonic Bandgap Crystals at Near-Infrared Wavelengths," *Science (80-.).*, vol. 289, pp. 604–606, 2000.

[19] M. Notomi, "Manipulating light with strongly modulated photonic crystals," *Reports Prog. Phys.*, vol. 73, no. 9, p. 096501, Sep. 2010.

[20] S. Noda, A. Chutinan, and M. Imada, "Trapping and emission of photons by a single defect in a photonic bandgap structure," *Nature*, vol. 407, no. 6804, Oct. 2000.

[21] Z. Zhang and M. Qiu, "Small-volume waveguide-section high Q microcavities in 2D photonic crystal slabs.," *Opt. Express*, vol. 12, no. 17, Aug. 2004.

[22] Z. Alferov, "The double heterostructure: concept and its application in physics, electronics and technology," 2000.

[23] U. W. Pohl, *Epitaxy of semiconductors*. Springer, 2013, p. 326.

[24] A. Y. Cho, "Film Deposition by Molecular-Beam Techniques," *J. Vac. Sci. Technol.*, vol. 8, no. 5, pp. S31–S38, Sep. 1971.

[25] H. M. Manasevit and W. I. Simpson, "The Use of Metal-Organics in the Preparation of Semiconductor Materials: I. Epitaxial gallium-V compounds," vol. 116, no. 12, pp. 1725–1732, 1969.

[26] K. Takeda, T. Sato, A. Shinya, K. Nozaki, W. Kobayashi, H. Taniyama, M. Notomi, K. Hasebe, T. Kakitsuka, and S. Matsuo, "Few-fJ/bit data transmissions using directly

modulated lambda-scale embedded active region photonic-crystal lasers," *Nat. Photonics*, vol. 7, no. 7, pp. 569–575, May 2013.

[27] A. Lupi, I.-S. Chung, and K. Yvind, "Electrical Injection Schemes for Nanolasers," *IEEE Photonics Technol. Lett.*, vol. 26, no. 4, pp. 330–333, Feb. 2014.

[28] A. Strittmatter, A. Holzbecher, A. Schliwa, J.-H. Schulze, D. Quandt, T. D. Germann, A. Dreismann, O. Hitzemann, E. Stock, I. A. Ostapenko, S. Rodt, W. Unrau, U. W. Pohl, A. Hoffmann, D. Bimberg, and V. Haisler, "Site-controlled quantum dot growth on buried oxide stressor layers," *Phys. Status Solidi Appl. Mater. Sci.*, vol. 209, no. 12, pp. 2411–2420, Dec. 2012.

[29] S. Matsuo, A. Shinya, T. Kakitsuka, K. Nozaki, T. Segawa, T. Sato, Y. Kawaguchi, and M. Notomi, "High-speed ultracompact buried heterostructure photonic-crystal laser with 13 fJ of energy consumed per bit transmitted," *Nat. Photonics*, vol. 4, pp. 648–654, 2010.

[30] E. Kapon, "Chapter 4 Lateral Patterning of Quantum Well Heterostructures by Growth on Nonplanar Substrates," *Semicond. Semimetals*, vol. 40, pp. 259–336, 1994.

[31] R. Bhat, E. Kapon, J. Werner, D. M. Hwang, N. G. Stoffel, and M. a. Koza, "Organometallic chemical vapor deposition of InP/InGaAsP on nonplanar InP substrates: Application to multiple quantum well lasers," *Appl. Phys. Lett.*, vol. 56, no. 9, p. 863, 1990.

[32] M. D. Scott, J. R. Riffat, I. Griffith, J. I. Davies, and A. C. Marshall, "Code: A novel MOVPE technique for the single stage growth of buried ridge double heterostructure lasers and waveguides," *J. of Cryst. Growth*, vol. 93. pp. 820–824, 1988.

[33] P. J. Poole, G. C. Aers, a. Kam, D. Dalacu, S. Studenikin, and R. L. Williams, "Selective growth of InP/InGaAs ‹010› ridges: Physical and optical characterization," *J. Cryst. Growth*, vol. 310, no. 6, pp. 1069–1074, Mar. 2008.

[34] C. Amano, A. Rudra, P. Grunberg, J. F. Carlin, and M. Ilegems, "Growth temperature dependence of the interfacet migration in chemical beam epitaxy of InP on non-planar substrates," *J. Cryst. Growth*, vol. 164, pp. 321–326, Jul. 1996.

[35] J. Décobert, N. Dupuis, P. Y. Lagrée, N. Lagay, a. Ramdane, a. Ougazzaden, F. Poingt, C. Cuisin, and C. Kazmierski, "Modeling and characterization of AlGaInAs and related materials using selective area growth by metal-organic vapor-phase epitaxy," *J. Cryst. Growth*, vol. 298, pp. 28–31, Jan. 2007.

[36] M. Gibbon, J. P. Stagg, C. G. Cureton, E. J. Thrush, C. J. Jones, R. E. Mellard, R. E. Pritchard, N. Collis, and A. Chew, "Selective-area low-pressure MOCVD of GaInAsP and related materials on planar InP substrates," *Semicond. Sci. Technol.*, vol. 8, pp. 998–1010, 1993.

[37] D. W. Shaw, "Selective Epitaxial Deposition of Gallium Arsenide in Holes," *J. Electrochem. Soc.*, vol. 113, no. 9, pp. 904–908, 1966.

[38] G. B. Stringfellow, *Organometallic Vapor-Phase Epitaxy, Second Edition: Theory and Practice*. 1999, p. 572.

[39] S. Noda, M. Fujita, and T. Asano, "Spontaneous-emission control by photonic crystals and nanocavities," *Nat. Photonics*, vol. 1, pp. 449–458, 2007.

[40] E. M. Purcell, "Spontaneous emission probabilities at radio frequencies," *Phys. Rev.*, vol. 69, pp. 681–681, 1946.

[41] S. Matsuo, T. Sato, K. Takeda, A. Shinya, K. Nozaki, H. Taniyama, M. Notomi, S. Member, K. Hasebe, and T. Kakitsuka, "Ultra-low Operating Energy Electrically Driven Photonic Crystal Lasers," *IEEE J. Selcted Top. Quantum Electron.*, vol. 19, no. 4, 2013.

[42] M. Matsuda, T. Simoyama, A. Uetake, S. Okumura, M. Ekawa, and T. Yamamoto, "Uncooled, low-driving-current 25.8 Gbit/s direct modulation using 1.3 μm AlGaInAs MQW distributed-reflector lasers," *Electron. Lett.*, vol. 48, no. 8, 2012.

[43] P. Moser, W. Hofmann, P. Wolf, J. a. Lott, G. Larisch, A. Payusov, N. N. Ledentsov, and D. Bimberg, "81 fJ/bit energy-to-data ratio of 850 nm vertical-cavity surface-emitting lasers for optical interconnects," *Appl. Phys. Lett.*, vol. 98, no. 23, 2011.

[44] O. Painter, R. K. Lee, A. Scheree, A. Yariv, J. D. O'Brien, P. D. Dapkus, and I. Kim, "Two-Dimensional Photonic Band-Gap Defect Mode Laser," *Science (80-.).*, vol. 284, no. 5421, pp. 1819–1821, Jun. 1999.

[45] S. Matsuo, A. Shinya, T. Kakitsuka, K. Nozaki, T. Segawa, T. Sato, Y. Kawaguchi, and M. Notomi, "Ultra-small InGaAsP/InP buried heterostructure photonic crystal laser," *2009 IEEE LEOS Annu. Meet. Conf. Proc.*, pp. 453–454, Oct. 2009.

[46] D. D. Nolte, "Surface recombination, free-carrier saturation, and dandling bonds in InP and Gas," *Solid. State. Electron.*, vol. 33, no. 2, pp. 295–298, 1990.

[47] A. G. Thompson, R. A. Stall, P. Zawadzki, and G. H. Evans, "The Scaling of CVD Rotating Disk Reactors to Large Sizes and Comparison With Theory," *J. Elecronic Mater.*, vol. 25, no. 9, pp. 1487–1494, 1996.

[48] E. M. Sparrow and J. L. Gregg, "Mass Transfer , Flow , and Heat Transfer About a Rotating Disk," *J. Heat Transfer*, pp. 294–302, 1960.

[49] R. Pollard and J. Newman, "Silicon Deposition on a Rotating Disk," *J. Electrochem. Soc. Solid-state Sci. Technol.*, vol. 127, no. 3, pp. 744–752, 1980.

[50] G. Evans and R. Greif, "Effects of Boundary Conditions on the Flow and Heat Transfer in a Rotating Disk Chemical Vapor Deposition Reactor," *Numer. Heat Transf.*, vol. 12, no. 2, pp. 243–252, Feb. 1987.

[51] W. G. Breiland and G. H. Evans, "Design and Verification of Nearly Ideal Flow and Heat Transfer in a Rotating Disk Chemical Vapor Deposition Reactor," *J. Electrochem. Soc.*, vol. 138, no. 6, pp. 1806–1816, 1991.

[52] W. G. Breiland, M. E. Coltrin, J. R. Creighton, H. Q. Hou, H. K. Moffat, and J. Y. Tsao, "Organometallic vapor phase epitaxy (OMVPE)," *Mater. Sci. Eng. R Reports*, vol. 24, no. 6, pp. 241–274, Feb. 1999.

[53] J. J. Coleman, "Metalorganic chemical vapor deposition for optoelectronic devices," *Proc. IEEE*, vol. 85, no. 11, pp. 1715–1729, 1997.

[54] B. Mitrovic, A. Gurary, and L. Kadinski, "Reactor Design Optimization Based on 3D CFD Modeling of Nitrides Deposition in MOCVD Vertical Rotating Disc Reactors," 2005, no. June.

[55] G. . Stringfellow, "Fundamental aspects of organometallic vapor phase epitaxy," *Mater. Sci. Eng. B*, vol. 87, no. 2, pp. 97–116, Nov. 2001.

[56] N. Dupuis, J. Décobert, P.-Y. Lagrée, N. Lagay, D. Carpentier, and F. Alexandre, "Demonstration of planar thick InP layers by selective MOVPE," *J. Cryst. Growth*, vol. 310, no. 23, pp. 4795–4798, Nov. 2008.

[57] I. Vurgaftman, J. R. Meyer, and L. R. Ram-Mohan, "Band parameters for III–V compound semiconductors and their alloys," *J. Appl. Phys.*, vol. 89, no. 11, pp. 5815–5875, 2001.

[58] N. Gogneau, L. Le Gratiet, E. Cambril, G. Beaudoin, G. Patriarche, a. Beveratos, R. Hostein, I. Robert-Philip, J. Y. Marzin, and I. Sagnes, "One-step nano-selective area growth (nano-SAG) of localized InAs/InP quantum dots: First step towards single-photon source applications," *J. Cryst. Growth*, vol. 310, no. 15, pp. 3413–3415, Jul. 2008.

[59] J. Décobert, N. Dupuis, P. Y. Lagrée, N. Lagay, a. Ramdane, a. Ougazzaden, F. Poingt, C. Cuisin, and C. Kazmierski, "Modeling and characterization of AlGaInAs and related materials using selective area growth by metal-organic vapor-phase epitaxy," *J. Cryst. Growth*, vol. 298, pp. 28–31, Jan. 2007.

[60] J. E. Greenspan, "Alloy composition dependence in selective area epitaxy on InP substrates," *J. Cryst. Growth*, vol. 236, no. 1–3, pp. 273–280, Mar. 2002.

[61] Y. Wang, H. Song, M. Sugiyama, Y. Nakano, and Y. Shimogaki, "Surface reaction kinetics of InP and InAs metalorganic vapor phase epitaxy analyzed by selective area growth technique," *Jpn. J. Appl. Phys.*, vol. 47, no. 10, pp. 7788–7792, 2008.

[62] A. Al Amin, T. Doi, K. Sakurai, Z. Z. Z. Zhang, X. S. X. Song, M. Sugiyama, and Y. Nakano, "Simulation of bandgap in MOVPE selective area growth of InGaAsP-based photonic integrated circuits," in *Proceedings of the 4th International Conference on Numerical Simulation of Optoelectronic Devices, 2004. NUSOD '04.*, 2004.

[63] T. Fujii and M. Ekawa, "Origin of compositional modulation of InGaAs in selective area metalorganic vapor phase epitaxy," *J. Appl. Phys.*, vol. 78, no. 9, p. 5373, 1995.

[64] T. Sasaki, M. Yamaguchi, and M. Kitamura, "Monolithically integrated multi-wavelength MQW-DBR laser diodes fabricated by selective metalorganic vapor phase epitaxy," *J. Cryst. Growth*, vol. 145, no. 1–4, pp. 846–851, Dec. 1994.

[65] R. Bhat, "Current status of selective area epitaxy by OMCVD," *J. Cryst. Growth*, vol. 120, pp. 362–368, May 1992.

[66] O. Kayser, B. Opitz, R. Westphalen, U. Niggebrügge, K. Schneider, and P. Balk, "Selective embedded growth of GaInAs by low pressure MOVPE," *J. Cryst. Growth*, vol. 107, no. 1–4, pp. 141–146, Jan. 1991.

[67] Y. Shimogaki, M. Sugiyama, and Y. Nakano, "Selective area MOVPE of InGaAsP and InGaN systems as process analytical and design tools for OEICs," in *2013 International Conference on Indium Phosphide and Related Materials (IPRM)*, 2013, vol. 1, pp. 1–2.

[68] Y. T. Sun, E. Rodríguez Messmer, S. Lourdudoss, J. Ahopelto, S. Rennon, J. P. Reithmaier, and a. Forchel, "Selective growth of InP on focused-ion-beam-modified GaAs surface by hydride vapor phase epitaxy," *Appl. Phys. Lett.*, vol. 79, no. 12, p. 1885, 2001.

[69] M. Kappet and D. Bimberg, "Wet Chemical Etching of High Quality V-Grooves with {111}A Sidewalls on (001) lnP," *J. Electrochem. Soc.*, vol. 143, no. 10, pp. 3271–3273, 1996.

[70] A. Stano, "Chemical Etching Characteristics of InGaAs / InP and InAlAs/InP Heterostructures," *J. Electrochem. Soc. Solid-state Sci. Technol.*, vol. 134, no. 2, pp. 448–452, 1987.

[71] M. Kappelt, M. Grundmann, A. Krost, V. Turck, and D. Bimberg, "InGaAs quantum wires grown by low pressure metalorganic chemical vapor deposition on InP V-grooves," *Appl. Phys. Lett.*, vol. 68, no. 25, p. 3596, 1996.

[72] T. Schrimpf, P. Bonsch, D. Wullner, H.-H. Wehmann, A. Schlachetzki, F. Bertram, T. Riemann, and J. Christen, "InGaAs quantum wires and wells on V-grooved InP substrates," *J. Appl. Phys.*, vol. 86, no. 9, p. 5207, 1999.

[73] Y. D. Galeuchet, P. Roentgen, and V. Graf, "Buried GaInAs/InP layers grown on nonplanar substrates by one-step low-pressure metalorganic vapor phase epitaxy," *Appl. Phys. Lett.*, vol. 53, no. 1988, pp. 2638–2640, 1988.

[74] Y. D. Galeuchet and P. Roentgen, "Selective area MOVPE of GaInAs/InP heterostructures on masked and nonplanar (100) and {111} substrates," *J. Cryst. Growth*, vol. 107, pp. 147–150, 1991.

[75] S.-H. Lim, S. Song, G.-D. Lee, E. Yoon, and J.-H. Lee, "Facet evolution in selective epitaxial growth of Si by cold-wall ultrahigh vacuum chemical vapor deposition," *J. Vac. Sci. Technol. B Microelectron. Nanom. Struct.*, vol. 22, no. 2, p. 682, 2004.

[76] C. Caneau, R. Bhat, M. R. Frei, S. a. Schwarz, W. a. Bonner, and M. a. Koza, "Selective OMVPE of GaInAs and InP using a polycrystalline InP mask," *J. Cryst. Growth*, vol. 114, no. 3, pp. 481–485, Nov. 1991.

[77] B. Garrett and E. J. Thrush, "Temporally resolved growth habit studies of InP/(InGa)As heterostucturegrown by MOCVD on contoured InP substrates," *J. Cryst. Growth*, vol. 97, pp. 273–284, 1989.

[78] P. Yeht, A. Yariv, and E. Marom, "Theory of Bragg fiber *," vol. 68, no. 9, pp. 1196–1201, 1978.

[79] E. Kuramochi, M. Notomi, S. Mitsugi, A. Shinya, T. Tanabe, and T. Watanabe, "Ultrahigh-Q photonic crystal nanocavities realized by the local width modulation of a line defect," *Appl. Phys. Lett.*, vol. 88, no. 4, p. 041112, 2006.

[80] E. Kuramochi, H. Taniyama, T. Tanabe, A. Shinya, and M. Notomi, "Ultrahigh-Q two-dimensional photonic crystal slab nanocavities in very thin barriers," *Appl. Phys. Lett.*, vol. 93, no. 11, p. 111112, 2008.

[81] Y. Tanaka, T. Asano, and S. Noda, "Design of Photonic Crystal Nanocavity With -Factor of," vol. 26, no. 11, pp. 1532–1539, 2008.

[82] S. Matsuo, T. Sato, K. Takeda, A. Shinya, K. Nozaki, E. Kuramochi, H. Taniyama, M. Notomi, T. Fujii, K. Hasebe, and T. Kakitsuka, "Photonic crystal lasers using wavelength-scale embedded active region," *J. Phys. D. Appl. Phys.*, vol. 47, pp. 1–18, 2014.

[83] J. D. Joannopoulos, S. G. Johnson, J. N. Winn, and R. D. Meade, *Photonic Crystals: Molding the Flow of Light*. Princeton University Press; 2nd edition, 2008, p. 304.

[84] T. Allen, *Computational Electrodynamics The Finite-Difference Time-Domain Method*. Artech House, Boston-London, 2nd edition, 2000, p. 599.

[85] S. Johnson and J. Joannopoulos, "Block-iterative frequency-domain methods for Maxwell's equations in a planewave basis," *Opt. Express*, vol. 8, no. 3, p. 173, Jan. 2001.

[86] K. Srinivasan and O. Painter, "Momentum space design of high-Q photonic crystal optical cavities," *Opt. Express*, vol. 10, no. 15, p. 670, Jul. 2002.

[87] S. Ek, "Active Photonic Crystal Waveguides," Technical University of Denmark, 2012.

[88] S. Substrate, T. Baba, A. Motegi, T. Iwai, N. Fukaya, and Y. Watanabe, "Light Propagation Characteristics of Straight Single-Line-Defect Waveguides in Photonic Crystal Slabs Fabricated Into a," vol. 38, no. 2, pp. 743–752, 2002.

[89] S. Johnson, P. Villeneuve, S. Fan, and J. Joannopoulos, "Linear waveguides in photonic-crystal slabs," *Phys. Rev. B*, vol. 62, no. 12, pp. 8212–8222, Sep. 2000.

[90] T. Baba, N. Fukaya, and J. Yonekura, "Observation of light propagation in photonic crystal optical waveguides with bends," *Electron. Lett.*, vol. 35, no. 8, p. 654, 1999.

[91] M. Notomi, A. Shinya, K. Yamada, J. Takahashi, C. Takahashi, and I. Yokohama, "Singlemode transmission within photonic bandgap of width-varied single-line-defect photonic crystal waveguides on SOI substrates," *Electron. Lett.*, vol. 37, no. 5, pp. 293–295, 2001.

[92] A. Chutinan and S. Noda, "Waveguides and waveguide bends in two-dimensional photonic crystal slabs," *Phys. Rev. B*, vol. 62, no. 7, pp. 4488–4492, Aug. 2000.

[93] X. Letartre, C. Seassal, C. Grillet, P. Rojo-Romeo, P. Viktorovitch, M. Le Vassor d'Yerville, D. Cassagne, and C. Jouanin, "Group velocity and propagation losses measurement in a single-line photonic-crystal waveguide on InP membranes," *Appl. Phys. Lett.*, vol. 79, no. 15, p. 2312, 2001.

[94] T. Baba and D. Mori, "Slow light engineering in photonic crystals," *J. Phys. D. Appl. Phys.*, vol. 40, no. 9, pp. 2659–2665, May 2007.

[95] C. López, "Anderson localization of light: A little disorder is just right," *Nature Physics*, vol. 4. pp. 755–756, 2008.

[96] O. Painter and K. Srinivasan, "Localized defect states in two-dimensional photonic crystal slab waveguides: A simple model based upon symmetry analysis," *Physical Review B*, vol. 68, no. 3. p. 035110, Jul-2003.

[97] M. Patterson, S. Hughes, S. Combrié, N.-V.-Q. Tran, a. De Rossi, R. Gabet, and Y. Jaouën, "Disorder-Induced Coherent Scattering in Slow-Light Photonic Crystal Waveguides," *Phys. Rev. Lett.*, vol. 102, no. 25, p. 253903, Jun. 2009.

[98] J. Liu, P. D. Garcia, S. Ek, N. Gregersen, T. Suhr, M. Schubert, J. Mørk, S. Stobbe, and P. Lodahl, "Random nanolasing in the Anderson localized regime.," *Nat. Nanotechnol.*, vol. 9, no. 4, pp. 285–9, Apr. 2014.

[99] S. Ek, P. Lunnemann, Y. Chen, E. Semenova, K. Yvind, and J. Mork, "Slow-light-enhanced gain in active photonic crystal waveguides.," *Nat. Commun.*, vol. 5, p. 5039, Jan. 2014.

[100] J. P. Dowling, M. Scalora, M. J. Bloemer, and C. M. Bowden, "The photonic band edge laser : A new ap roach to gain enhancement," vol. 75, no. November 1993, pp. 4–7, 1994.

[101] T. F. Krauss, "Slow light in photonic crystal waveguides," *J. Phys. D. Appl. Phys.*, vol. 40, no. 9, pp. 2666–2670, May 2007.

[102] J. Grgić, J. R. Ott, F. Wang, O. Sigmund, A.-P. Jauho, J. Mørk, and N. A. Mortensen, "Fundamental Limitations to Gain Enhancement in Periodic Media and Waveguides," *Phys. Rev. Lett.*, vol. 108, no. 18, p. 183903, May 2012.

[103] U. P. Dharanipathy, M. Minkov, M. Tonin, V. Savona, and R. Houdré, "Evolutionarily optimized ultrahigh-Q photonic crystal nanocavity," in *Optics Info Base*, 2013, p. 17.

[104] P. Lalanne, C. Sauvan, and J. P. Hugonin, "Photon confinement in photonic crystal nanocavities," *Laser Photonics Rev.*, vol. 2, no. 6, pp. 514–526, Dec. 2008.

[105] M. Heuck, S. Blaaberg, and J. Mørk, "Short Pulse Generation in a Passively Mode-Locked Photonic Crystal Semiconductor Laser," *Integr. Photonics Res. Silicon Nanophotonics Photonics Switch.*, p. ITuA2, 2010.

[106] Y. Chen and J. Mørk, "Distributed Feedback Effects in Active Semiconductor Photonic Crystal Waveguides," in *Advanced Photonics Congress*, 2012, pp. 2–4.

[107] Q. V. Tran, S. Combrié, P. Colman, and A. De Rossi, "Photonic crystal membrane waveguides with low insertion losses," *Appl. Phys. Lett.*, vol. 95, no. 6, p. 061105, 2009.

[108] L. Dong-Jin, L. Seung-Gol, L. El-Hang, and O. Beom-Hoan, "Effective Restoration of Junction Coupling by Position Tuning of Inlet Holes in Photonic Crystal Waveguides," *J. Korean Phys. Soc.*, vol. 58, no. 6, pp. 1587–1590, Jun. 2011.

[109] H. Namatsu, "Three-dimensional siloxane resist for the formation of nanopatterns with minimum linewidth fluctuations," *J. Vac. Sci. Technol. B Microelectron. Nanom. Struct.*, vol. 16, no. 1, p. 69, Jan. 1998.

[110] A. E. Grigorescu and C. W. Hagen, "Resists for sub-20-nm electron beam lithography with a focus on HSQ: state of the art.," *Nanotechnology*, vol. 20, no. 29, p. 292001, Jul. 2009.

[111] D. L. Olynick, J. A. Liddle, A. V. Tivanski, M. K. Gilles, T. Tyliszczak, F. Salmassi, K. Liang, and S. R. Leone, "Scanning x-ray microscopy investigations into the electron-beam exposure mechanism of hydrogen silsesquioxane resists," *J. Vac. Sci. Technol. B Microelectron. Nanom. Struct.*, vol. 24, no. 6, pp. 3048–3054, 2006.

[112] Datasheet, "Dow Corning ® XR-1541 E-Beam."

[113] N. Clark, A. Vanderslice, R. Grove, and R. R. Krchnavek, "Time-dependent exposure dose of hydrogen silsesquioxane when used as a negative electron-beam resist," *J. Vac. Sci. Technol. B Microelectron. Nanom. Struct.*, vol. 24, no. 6, pp. 3073–3076, 2006.

[114] S. Adachi, *Physical properties of III-V semiconductor compounds*. New York: Waley, 1992.

[115] A. E. Grigorescu, M. C. van der Krogt, C. W. Hagen, and P. Kruit, "10nm lines and spaces written in HSQ, using electron beam lithography," *Microelectron. Eng.*, vol. 84, pp. 822–824, May 2007.

[116] Y. M. Georgiev, W. Henschel, A. Fuchs, and H. Kurz, "Surface roughness of hydrogen silsesquioxane as a negative tone electron beam resist," *Vacuum*, vol. 77, no. 2, pp. 117–123, Jan. 2005.

[117] D. Lauvernier, S. Garidel, C. Legrand, and J.-P. Vilcot, "Realization of sub-micron patterns on GaAs using a HSQ etching mask," *Microelectron. Eng.*, vol. 77, no. 3–4, pp. 210–216, Apr. 2005.

[118] F. C. M. J. M. van Delft, "Delay-time and aging effects on contrast and sensitivity of hydrogen silsesquioxane," *J. Vac. Sci. Technol. B Microelectron. Nanom. Struct.*, vol. 20, no. 6, pp. 2932–2936, 2002.

[119] Y. Sun, Z. Liu, F. Machuca, P. Pianetta, and W. E. Spicer, "Optimized cleaning method for producing device quality InP(100) surfaces," *J. Appl. Phys.*, vol. 97, no. 12, pp. 124902–1 – 124902–7, 2005.

[120] C. Ebert, J. Levkoff, J. Roberts, J. Seiler, C. Wanamaker, and T. Pinnington, "Selective area etching of InP with CBr4 in MOVPE," *J. Cryst. Growth*, vol. 298, pp. 94–97, Jan. 2007.

[121] J. Tommila, a. Tukiainen, J. Viheriälä, a. Schramm, T. Hakkarainen, a. Aho, P. Stenberg, M. Dumitrescu, and M. Guina, "Nanoimprint lithography patterned GaAs templates for site-controlled InAs quantum dots," *J. Cryst. Growth*, vol. 323, no. 1, pp. 183–186, May 2011.

[122] Y. Huang, T. Kim, T. Garrod, L. J. Mawst, S. Xiong, P. F. Nealey, K. Schulte, and T. F. Kuech, "Nanofabrication of quantum dots on InP by in-situ etching and selective growth," in *Science and Innovations (CLEO Technical Digest)*, 2012.

[123] S. Arakawa, M. Itoh, and A. Kasukawa, "In-Situ Etching of Semiconductor with CBr4 in Metalorganic Chemical Vapor Deposition (MOCVD) Reactor," *Jpn. J. Appl. Phys.*, vol. 41, no. Part 1, No. 2B, pp. 1076–1079, Feb. 2002.

[124] K. Tateno, Y. Kohama, and C. Amano, "Carbon doping and etching effects of CBr4 during metalorganic chemical vapor deposition of GaAs and AlAs," *J. Cryst. Growth*, vol. 172, pp. 5–12, Feb. 1997.

[125] B. Henle, R. Rudeloff, H. Bolay, and F. Scholz, "In situ selective-area etching and MOVPE regrowth of GaInAs-InP on InP substrates," *Semicond. Sci. Technol.*, vol. 8, pp. 994–997, 1993.

[126] S. Adachi and H. Kawaguchi, "Chemical Etching Characteristics of (001) InP," *J. Electrochem. Soc.*, vol. 128, no. 6, pp. 1342–1349, 1981.

[127] Y. Sakata, Y. Inomoto, and K. Komatsu, "Surface migration effect and lateral vapor-phase diffusion effect for InGaAsP/InP narrow-stripe selective metal-organic vapor-phase epitaxy," *J. Cryst. Growth*, vol. 208, pp. 130–136, 2000.

[128] M. Sugiyama, "Selective area growth of III-V semiconductors: From fundamental aspects to device structures," in *2010 22nd International Conference on Indium Phosphide and Related Materials (IPRM)*, 2010, pp. 1–6.

[129] P. H. L. Notten, "The Etching of InP in HCI Solutions: A Chemical Mechanism," *J. Electrochem. Soc.*, vol. 131, no. 11, pp. 2641–2644, 1983.

[130] P. Eliás, I. Kostic, J. Soltýs, and S. Hasenöhrl, "Wet-etch bulk micromachining of (100) InP substrates," *J. Micromechanics Microengineering*, vol. 14, no. 8, pp. 1205–1214, Aug. 2004.

[131] T. R. Hayes, D. M. A., T. P. M., D. W. C., and H. L. A., "Reactive ion etching of InP using CH4/H2 mixtures: Mechanisms of etching and anisotropy," *J. Vac. Sci. Technol. B Microelectron. Nanom. Struct.*, vol. 7, no. 5, pp. 1130–1140, Sep. 1989.

[132] M. Schubert, "Coupled Photonic Crystal Cavity Array Laser," Technical University of Denmark, 2010.

[133] M. Varela, A. R. Lupini, K. van Benthem, A. Y. Borisevich, M. F. Chisholm, N. Shibata, E. Abe, and S. J. Pennycook, "Materials Characterization in the Aberration-Corrected Scanning Transmission Electron Microscope," *Annu. Rev. Mater. Res.*, vol. 35, no. 1, pp. 539–569, Aug. 2005.

[134] J. Hergeth, D. Grützmacher, F. Reinhardt, and P. Balk, "Effect of growth parameters on the interfacial structure of GaInAs/InP quantum wells," *J. Cryst. Growth*, vol. 107, no. 1–4, pp. 537–542, Jan. 1991.

[135] H. Kamei and H. Hayashi, "OMVPE growth of GaInAs/InP and GaInAs/GaInAsP quantum wells," *J. Cryst. Growth*, vol. 107, pp. 567–572, 1991.

[136] K. Streubel, V. Haarle, F. Scholz, M. Bode, and M. Grundmann, "Interfacial properties of very thin GaInAs/InP quantum well structures grown by metalorganic vapor phase epitaxy," *J. Appl. Phys.*, vol. 71, no. 7, pp. 3300–3306, 1992.

[137] D. Bimberg, J. Christen, T. Fukunaga, H. Nakashima, D. E. Mars, and J. N. Miller, "Cathodoluminescence atomic scale images of monolayer islands at GaAs / GaAIAs interfaces," *J. Vac. Sci. Technol. B*, vol. 5, pp. 1191–1197, 1987.

[138] J. Christen, M. Grundmann, and D. Bimberg, "Scanning cathodoluminescence microscopy: A unique approach to atomic-scale characterization of heterointerfaces and imaging of semiconductor inhomogeneities," *J. Vac. Sci. Technol. B Microelectron. Nanom. Struct.*, vol. 9, no. 4, pp. 2358–2368, Jul. 1991.

[139] G. D. Gilliland, "Photoluminescence spectroscopy of crystalline semiconductors," *Materials Science and Engineering: R: Reports*, vol. 18. pp. 99–399, 1997.

[140] I. V. Kulkova, S. Kadkhodazadeh, N. Kuznetsova, A. Huck, E. S. Semenova, and K. Yvind, "High-quality MOVPE butt-joint integration of InP/AlGaInAs/InGaAsP-based all-active optical components," *J. Cryst. Growth*, vol. 402, pp. 243–248, Sep. 2014.

[141] H. Debrégeas, J. Decobert, N. Lagay, R. Guillamet, D. Carrara, O. Patard, C. Kazmierski, and R. Brenot, "Selective-area-growth technology for flexible active building blocks," in *Advanced Photonics Congress*, 2012, pp. 4–6.

[142] H. Temkin, G. J. Dolan, M. B. Panish, and S. N. G. Chu, "Low temperature photoluminescence from InGaAs/lnP quantum wires and boxes," *Appl. Phys. Lett.*, vol. 50, no. 413, pp. 413–415, 1987.

[143] M. Patterson, S. Hughes, D. Dalacu, and R. Williams, "Broadband Purcell factor enhancements in photonic-crystal ridge waveguides," *Phys. Rev. B*, vol. 80, no. 12, p. 125307, Sep. 2009.

[144] S. Hughes, L. Ramunno, J. Young, and J. Sipe, "Extrinsic Optical Scattering Loss in Photonic Crystal Waveguides: Role of Fabrication Disorder and Photon Group Velocity," *Phys. Rev. Lett.*, vol. 94, no. 3, p. 033903, Jan. 2005.

[145] E. K. Lau, A. Lakhani, R. S. Tucker, and M. C. Wu, "Enhanced modulation bandwidth of nanocavity light emitting devices," *Opt. Express*, vol. 17, no. 10, p. 7790, Apr. 2009.

[146] N. Gregersen, T. Suhr, M. Lorke, and J. Mørk, "Quantum-dot nano-cavity lasers with Purcell-enhanced stimulated emission," *Appl. Phys. Lett.*, vol. 100, no. 13, p. 131107, 2012.

[147] H. Altug, D. Englund, and J. Vučković, "Ultrafast photonic crystal nanocavity laser," *Nat. Phys.*, vol. 2, no. 7, pp. 484–488, Jul. 2006.

[148] K. Kiyota, T. Kise, N. Yokouchi, T. Ide, and T. Baba, "Various low group velocity effects in photonic crystal line defect waveguides and their demonstration by laser oscillation," *Appl. Phys. Lett.*, vol. 88, no. 20, p. 201904, 2006.

[149] M. Akabori, J. Takeda, J. Motohisa, and T. Fukui, "InGaAs nano-pillar array formation on partially masked InP(111)B by selective area metal–organic vapour phase epitaxial growth for two-dimensional photonic crystal application," *Nanotechnology*, vol. 14, no. 10, pp. 1071–1074, Oct. 2003.

[150] "Dow Corning," "XR-1541 Spin Curve after HP." .